Deformation of geothermal reservoirs: A case study in the Hengill geothermal area using satellite geodesy

Daniel Juncu

Faculty of Earth Sciences
University of Iceland
2018

Deformation of geothermal reservoirs: A case study in the Hengill geothermal area using satellite geodesy

Daniel Juncu

Dissertation submitted in partial fulfillment of a
Philosophiae Doctor degree in Geophysics

Advisor
Dr. Thóra Árnadóttir

PhD Committee
Dr. Halldór Geirsson, University of Iceland
Dr. Andrew Hooper, University of Leeds, UK
Dr. Björn Lund, Uppsala University, Sweden

Opponents
Dr. Ólafur G. Flóvenz, ÍSOR — Iceland GeoSurvey
Dr. Sigurjón Jónsson, King Abdullah University of Science and Technology, Saudi Arabia

Faculty of Earth Sciences
School of Engineering and Natural Sciences
University of Iceland
Reykjavik, January 2018

Deformation of geothermal reservoirs:
A case study in the Hengill geothermal area using satellite geodesy
Deformation in the Hengill geothermal area
Dissertation submitted in partial fulfillment of a *Philosophiae Doctor* degree in Geophysics

Faculty of Earth Sciences
School of Engineering and Natural Sciences
University of Iceland
Sturlugata 7
101, Reykjavik
Iceland

Telephone: 525-4000

Bibliographic information:
Daniel Juncu, 2018, *Deformation of geothermal reservoirs:*
A case study in the Hengill geothermal area using satellite geodesy, PhD dissertation, Faculty of Earth Sciences, University of Iceland, 126 pp.

ISBN 978-9935-9306-8-2

Printing: Háskólaprent ehf.
Reykjavik, Iceland, January 2018

Abstract

Deformation of geothermal reservoirs is a growing topic in the field of crustal deformation research. The deformation behavior of a geothermal resource can give us insight about its sustainability and can help to increase our understanding of reservoir processes. The topic of this dissertation is crustal deformation in the Hengill area with focus on the deformation around the two geothermal fields of Hengill: Hellisheidi and Nesjavellir. We show that in a complex geological setting as we have in Hengill, we need good models of the regional deformation processes to be able to investigate the more localized deformation signals of geothermal reservoirs. The plate spreading constitutes a significant component to the horizontal displacement at Hengill which can be seen in GNSS data as well as InSAR data. Additionally, a wide scale deformation signal can be seen in Eastern Hengill. The first paper of this thesis describes these observations and their modeling. We find that local subsidence signals at Hellisheidi and Nesjavellir is consistent with the observed pressure decrease in the two geothermal fields. In the second paper in this thesis, we investigate an uplift signal that was observed at Húsmúli, one of the injection sites at the Hellisheidi field, during 2011–2012. The signal appeared at the same time as the injection and an increase in seismicity in September 2011. We interpret the deformation as being caused by an increase in pore pressure, which in turn led to an increase in seismicity. To better understand the deformation of geothermal reservoirs, we study the relationship between amount of extracted geothermal fluid and the magnitude of reservoir deformation as the third topic of the thesis. We show that the ratio of reservoir volume decrease due to deformation to mass of extracted fluid depends on a number of parameters, in particular the compressibility of rock and pore fluid. We use examples from three geothermal reservoirs to investigate how different values of this ratio can be explained by different combinations of material parameters. Possible ranges of parameter combinations are presented for each case, showing that our method can be used to constrain values of material properties based on geodetic observations of surface deformation.

Útdráttur

Mælingar og líkangerð á jarðskorpuhreyfingum á jarðhitasvæðum er vaxandi grein innan jarðeðlisfræði. Slíkar rannsóknir á hreyfingum á yfirborði jarðhitasvæða gefa m.a. upplýsingar um ástand jarðhitageyma (rúmmálsbreytingar og staðsetningu) á hverjum tíma. Niðurstöðurnar þarf að túlka í samræmi við aðrar jarðeðlisfræðilegar mælingar til að auka skilning á eðli svæðisins, t.d. við mat á vinnslugetu og hve lengi má nýta það. Í þessari ritgerð er fjallað um jarðskorpuhreyfingar og líkangerð á Hengilssvæðinu, sér í lagi á vinnslusvæðum fyrir virkjanirnar tvær: Hellisheiði og Nesjavelli. Til að skilja staðbundnar jarðskorpuhreyfingar á Hengilssvæðinu er nauðsynlegt að leiðrétta fyrir öðrum þáttum, m.a. hreyfingum vegna landreks. Landrekið veldur aðallega láréttum færslum og sést vel í landmælingum með gervitunglum – GNSS og radarbylgjuvíxlmyndum (InSAR). Auk þess mælist sig á stóru svæði í austurhluta Hengilssvæðisins. Fyrsti kafli ritgerðarinnar lýsir þessum mælingum og líkangerð. Helsta niðurstaða líkangerðarinnar er að staðbundið sig við Hellisheiði og Nesjavelli sé í samræmi við mælingar á þrýstingslækkun í jarðhitageymunum. Í öðrum kafla ritgerðarinnar er greint frá landrisi sem við mælum við Húsmúla á tímabilinu 2011-2012. Landrisið hófst á sama tíma og niðurdæling á jarðhitavökva og aukinnar smáskjálftavirkni varð vart í september 2011. Líkangerð á landmælingunum bendir til að jarðskorpuhreyfingarnar (landris og þensla) og jarðskjálftavirknina megi skýra með auknum poruþrýsingi í berginu þar sem jarðhitavökvanum er dælt niður. Þriðji kafli ritgerðarinnar kannar tengsl jarðskorpuhreyfinga við magn jarðhitavökva sem dælt er upp úr jarðhitasvæðum. Við sýnum að hlutfall rúmmálsminnkunar í jarðhitageyminum og massa jarðhitavökva sem dælt er upp, er aðallega háð samþjöppun bergs og vökva. Við bárum þetta hlutfall saman á þremur háhitasvæðum, þar sem munurinn er allt að tífaldur, til að kanna möguleg gildi á efniseiginleikum bergs og jarðhitavökva. Niðurstöðurnar benda til að nota megi aðferðina, sem leidd er út í kafla 3, til að setja skorður á efniseiginleika jarðhitasvæða út frá mælingum á jarðskorpuhreyfingum.

Table of Contents

List of Figures

List of Tables

List of Original Papers

I: Juncu, D., Árnadóttir, T., Hooper, A., and Gunnarsson, G. (2017). Anthropogenic and natural ground deformation in the Hengill geothermal area, Iceland. *Journal of Geophysical Research: Solid Earth*, 122(1):692–709.

II: Juncu, D., Árnadóttir, T., Geirsson, H., Guðmundsson, G. B., Lund, B., Gunnarsson, G., Hooper, A., Hreinsdóttir, S. and Michalczewska, K. Injection-induced surface deformation and seismicity at the Hellisheidi geothermal field, Iceland. Submitted to *Journal of Volcanology and Geothermal Research*.

III: Juncu, D., Árnadóttir, T., Geirsson, H., and Gunnarsson, G. The effect of fluid compressibility and elastic rock properties on deformation of geothermal reservoirs. Submitted to *Geophysical Journal International*.

Acknowledgments

First and foremost, I would like to thank my PhD advisor Thóra Árnadóttir from whom I learned so much during the last years. With her patience and guidance she always lead me in the right direction. I am also very grateful for all the advice I received from my great co-advisors, Halldór Geirsson, Andy Hooper and Björn Lund. The help from my advisory team is what made this thesis possible. I would like to extend my gratitude to everyone in the Crustal Deformation group at the University of Iceland, who not only always offered help and advice when needed but are also a truly pleasant group of people to share a workplace with. And not to forget, many thanks to all the people with whom I had the pleasure to do field work with during my PhD. Additional thanks to Reykjavik Energy, ÍSOR and the Icelandic Meteorological Office for generously sharing their data which greatly helped this study. This work was supported in part by grants from the Iceland Research Fund and the University of Iceland Research Fund.

I want to thank my family and my friends, back home and elsewhere in the world, for not forgetting about me during all this time and even making a trip or another to visit me in the cold north. It was always very much appreciated! And last but not least, I am very grateful for all the friends I have made in Iceland during the last years. Thank you all, for all the good times, the beers, the skiing, the movies and of course the serious physical exercise with DRC. All of this is what made me really enjoy the last four years.

1 Introduction

1.1 Crustal deformation in Iceland

Iceland, with all its volcanic and tectonic activity, presents itself like a natural laboratory for earth scientists. Being a surface section of the Mid-Atlantic ridge it features volcanic eruptions, plate spreading, earthquakes and steaming geothermal areas. The combination makes for a highly dynamic environment causing the Earth's crust to deform in complex patterns. The most prominent of the active deformation processes in Iceland is the spreading between the North American and Eurasian tectonic plates. Decades before the theory of plate tectonics became scientific consensus, researchers already attributed extensional features of Iceland's geology to large scale tectonic processes (see e.g. Nielsen, 1930). For a long time, however, it was difficult to quantify and validate this hypothesis, basically for two reasons: the magnitude of deformation was either too small to be measured or its scale was too large to be captured using the available techniques. With the rise of millimeter-precision geodetic techniques, the first problem was solved and it became possible to detect small magnitude deformation processes. Gaining momentum in the 1960s, distance and tilt measurements were performed to measure local surface displacements in and across rift zones as well as around volcanoes, using geodimeters, tilt-meters and optical leveling (Tryggvason, 1968; Decker et al., 1971; Tryggvason, 1994). Starting in the 1980s, satellite-borne geodesy drastically increased the spatial scales on which observations could be made. The global positioning system (GPS), first used to study deformation in Iceland in 1986 (Foulger et al., 1987), was applied to detect surface motion in a countrywide network, measured in 1993 and 2004, revealing the spreading across the plate boundary (Árnadóttir et al., 2009). Interferometric satellite-borne synthetic aperture radar (InSAR) added the possibility of spatially dense measurements of surface motion over scales of tens of kilometers. Vadon and Sigmundsson (1997) applied it in Iceland for the first time, showing how it can be used on a regional scale to highlight plate spreading and geothermal reservoir deformation.

Over the years an extensive range of deformation processes have been observed in Iceland using GPS and InSAR, with the purpose of research or monitoring of natural hazards. These processes include deformation of magma chambers (e.g. Sigmundsson et al., 1992; Geirsson et al., 2012), propagation of dykes (Sigmundsson et al., 2015), deformation during (e.g. Pedersen et al., 2001; Árnadóttir et al., 2001) and following (e.g. Jónsson et al., 2003; Árnadóttir et al., 2005) earthquakes, deformation following rifting episodes (e.g. Foulger et al., 1992; Sigmundsson et al., 1997), glacial isostatic adjustment (e.g. Árnadóttir et al., 2009; Auriac et al., 2013), seasonal surface load variations (Grapenthin et al., 2006; Drouin et al., 2016) and geothermal energy production (e.g.

Vadon and Sigmundsson, 1997).

In this study we focus on surface deformation in the Hengill area in south-west Iceland (Figure 1.1). We investigate the complex deformation field generated by overlapping signals from plate spreading, geothermal reservoir- and volcanic deformation in Paper I. In Paper II, we investigate how injection in the Hellisheidi geothermal field can cause surface uplift and how injection and uplift relate to the local increase in seismicity. For Paper III we take a more general look at how the amount (i.e. volume or mass) of fluid extraction from a geothermal reservoir relates to the deformation and compare the behavior of the Hellisheidi reservoir to geothermal fields in- and outside of Iceland.

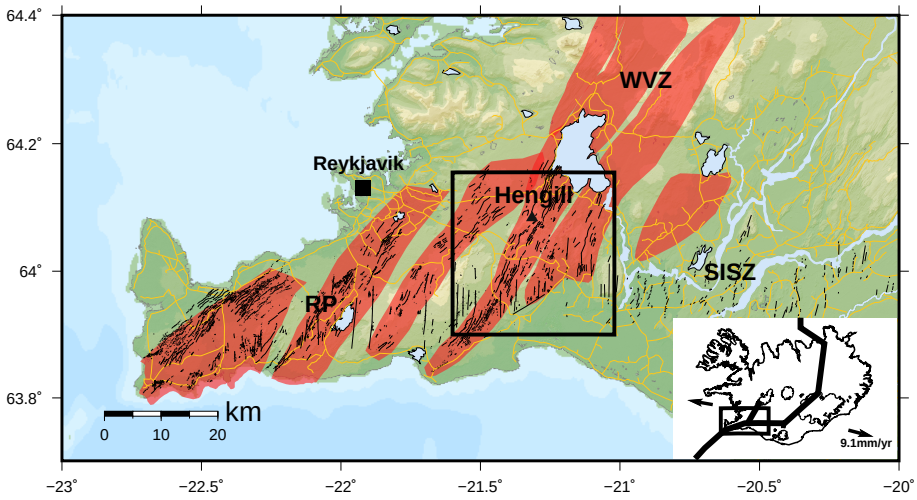

Figure 1.1: Southwest Iceland and the study area at Hengill. Red areas show fissure swarms (Hjartardóttir et al., 2016). Surface faults are shown as black lines and are taken from Clifton et al. (2002) and Einarsson (2008). The small map of Iceland in the bottom right shows the location of plate boundaries taken from Árnadóttir et al. (2009) and plate velocities calculated using the MORVEL model (DeMets et al., 2010).

1.2 The Hengill area

The Hengill mountain range, around 20 km east of Reykjavik, is a particular interesting area for studying deformation processes. It marks a triple junction of the plate boundaries between the North American plate, the Eurasian plate and the Hreppar microplate. The arms of the plate boundaries that meet here are the Reykjanes Peninsula (RP) in the south-west, the South Iceland Seismic Zone (SISZ) in the east and the Western Volcanic Zone (WVZ) in the north (Figure 1.1). Being located on a divergent plate boundary Hengill has a history of volcanism, usually attributed to three different volcanic centers: the long inactive Grensdalur system (Foulger, 1988), the Hengill system and the Hrómundartindur system. The Hengill and Hrómundartindur systems are part of two separate, parallel fissure swarms (depicted as orange areas in Figure

1.2; see Hjartardóttir et al., 2016; Steigerwald, 2017). The most recent eruptions are attributed to the Hengill system, with the last eruption occurring around 2000 years ago (Sæmundsson, 1967). The volcanic eruptions produced interbedded hyaloclastite and basaltic lava formations which are highly fractured (Sæmundsson, 1967; Franzson et al., 2010). SW-NE striking fissure swarms and normal faults characterize the Hengill range, but faults and fractures of various orientations can be found including N-S striking right-lateral strike-slip faults (e.g. Clifton et al., 2002).

The N-S orientation of strike-slip fault is widely observed in the region, e.g. on the Reykjanes peninsula (Clifton et al., 2003) and in the SISZ. In the SISZ, N-S oriented strike-slip earthquakes are common with major events occurring in sequences with average recurrence intervals of 80 to 100 years (Einarsson, 1991). The most recent sequence started in 2000 with two earthquakes of moment magnitudes 6.4–6.5 (e.g. Árnadóttir et al., 2001; Pedersen et al., 2003) and continued with two M_W 6 events close to the Ölfus river (Hreinsdóttir et al., 2009), directly south-east of Hengill (Figure 1.2). During an episode of seismic unrest and surface uplift between 1994–1998, two earthquakes of $M_L \geq 5.0$ occurred on right-lateral N-S trending faults. The epicenters of both earthquakes are located close to the boundary between the Hengill and Hrómundartindur fissure swarms (Clifton et al., 2002, locations in Figure 1.2). Episodes of induced seismicity in the Húsmúli area at the Hellisheidi power plant occur on N-S striking strike-slip faults, as well (see Paper II).

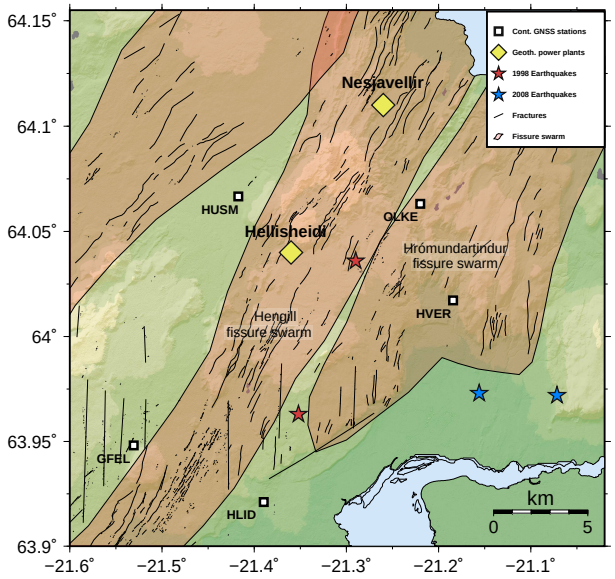

Figure 1.2: The study area at Hengill, with locations of continuous GNSS stations (as of 2015), the two geothermal power plants, the 1998 and 2008 earthquakes, surface faults and fissure swarms. Faults are shown as black lines and are taken from Clifton et al. (2002) and Einarsson (2008). Orange areas are fissure swarms (Hjartardóttir et al., 2016).

On the top of creating a complex geological structure, Hengill's volcanic activity provides the energy for Iceland's most productive geothermal power sources. Today,

there are two geothermal power plants operational in Hengill (see Figure 1.2): Nesjavellir, located on the northern end of the Hengill range is operational since 1990, produces circa 120 MW electrical power. Hellisheidi, on the southern end, has been operational since 2006, with a production capacity of 300 MW for electricity. Hellisheidi is the largest geothermal power station in Iceland and received special attention in 2011 after an intense increase in seismicity with the commencing of re-injection of geothermal waste-water at the northwestern edge of the geothermal field, at the Húsmúli injection site (Paper II).

1.3 Deformation in geothermal areas

Like other types of subsurface fluid reservoirs (groundwater, oil, gas), geothermal reservoirs can exhibit considerable amounts of deformation when fluids are removed or injected. The volume change of the reservoir fluid can either change pore/fracture pressure or the production/injection of fluid can cause a temperature change in the reservoir, both of which may result in deformation of the reservoir.

The first well known example (and probably until today the most substantial case) occurred at the Wairakei field in New Zealand, where the first borehole was drilled in 1950. Subsidence was observed for the first time in 1956 by re-leveling the 1950 benchmark levels, measuring a maximum subsidence of around 8 cm (Hatton, 1970). The complete power plant was commissioned in 1958 and by 2007 the maximum subsidence had reached 15 m, with observed subsidence rates being as high as $50\,\mathrm{cm\,yr^{-1}}$ (Allis et al., 2009). Other cases have been reported from various geothermal areas around the world, e.g.: Cerro Prieto, Mexico (Carnec and Fabriol, 1999; Glowacka et al., 1999), the Geysers, USA (Lofgren, 1978; Mossop and Segall, 1997), Larderello, Italy (Dini and Rossi, 1990) and Bulalo, Philippines (Nordquist et al., 2004).

The five largest geothermal power plants in Iceland are Hellisheidi, Nesjavellir, Reykjanes, Svartsengi and Krafla. All of the geothermal fields that these plants exploit show observable surface deformation on the order of a few millimeters to a few centimeters per year. For Reykjanes, Svartsengi and Krafla these rates have been reported by e.g. Keiding et al. (2010), Vadon and Sigmundsson (1997), Sturkell et al. (2008) and Drouin et al. (2017). Deformation rates for Hellisheidi and Nesjavellir are presented in Papers I and II of this dissertation.

The most common occurrence of observed deformation around geothermal fields is ground subsidence due to fluid extraction (see examples above). Cases of ground uplift caused by fluid injection (which is common practice to maintain pressure in geothermal systems), however, have been observed as well. Heimlich et al. (2015), for example, report surface uplift (in line of sight of the satellite, see Section 2.2) of 4 cm within 8 months between 2013 and 2014 at the geothermal power plant of Landau, Germany. In an experimental setting, Vasco et al. (2002a) used tilt measurements of injection related deformation to determine reservoir flow characteristics at the Hijori test site in Japan.

In this dissertation we study deformation around the geothermal fields in the Hengill area, Hellisheidi and Nesjavellir, in detail. GNSS data from a dense campaign network, combined with data from continuous stations as well as InSAR data help us to quantify

surface displacements with millimeter precision. We analyze the data in order to separate the signal from the geothermal fields from regional deformation, plate spreading and volcano related deformation. Using analytical models, we model the deformation related to both extraction (Paper I) and injection (Paper II) and compare the results to the amount of fluid that was extracted or injected. We investigate, with an idealized model, what controls the relation between magnitude of deformation and amount of extracted/injected fluid in order to learn more about material properties, both of the host rock and of the geothermal fluid (Paper III).

1.4 Induced seismicity due to fluid extraction and injection

Induced seismicity is frequently observed in the vicinity of hydrocarbon or geothermal fluid exploitation sites (see Ellsworth, 2013; Zang et al., 2014). Generally speaking, it can be caused by an increase in shear stress, a decrease in (compressive) normal stress or an increase in pore pressure (e.g. Simpson et al., 1988; McGarr et al., 2002). Stress changes can be caused by both production and injection of fluids while pore pressure can increase when fluids are injected into a reservoir.

Examples of increasing seismicity related to fluid extraction are numerous, in particular for cases of hydrocarbon production (see e.g. Yerkes and Castle, 1976; Segall, 1989). In cases of geothermal fluid production, Fialko and Simons (2000), as well as Keiding et al. (2010) discuss for the geothermal fields at Coso, USA and Reykjanes, Iceland how fluid pressure drawdown may have caused stress changes leading to an increase in seismicity. These cases exhibit an increase in seismic activity both in- and outside of the main production area.

Earthquakes induced by fluid injection have been observed at a number of injection sites. The earliest well-documented example of this is a chemical weapon manufacturing site in Colorado, USA, where chemical waste-fluids were injected into the ground (Healy et al., 1968). It has since been observed related to injection operations at oilfields (e.g. Raleigh et al., 1976; Ottemöller et al., 2005; Shirzaei et al., 2016) as well as at geothermal fields (see Evans et al., 2012, for an overview). At the Geysers, USA, Rutqvist and Oldenburg (2008) argue that local cooling around injection wells causes stress changes which in turn generate induced seismicity. At Soultz-sous-Forêts, France (Baisch et al., 2010), in Basel, Switzerland (Deichmann and Giardini, 2009), and at the KTB site in southern Germany (Zoback and Harjes, 1997), increased seismicity has been attributed to pore pressure increase.

The most well known case of induced seismicity in Iceland is related to the re-injection of waste-water at the Húsmúli injection site into the Hellisheidi geothermal field (e.g. Bessason et al., 2012). Seismicity was observed during drilling and testing of production and injection wells at Hellisheidi between 2002 and 2011 (Ágústsson et al., 2015). When full-scale injection started at Húsmúli in September 2011 a strong increase in seismic activity was observed, culminating in two magnitude 4 earthquakes on 15 October 2011, which were felt in neighbouring towns and in the capital area 20 km to the west. In Paper II we investigate the link between the increase in seismicity, fluid

injection and surface deformation.

2 Methods

2.1 GNSS

The Global Navigation Satellite System (GNSS) is a geodetic system that uses radio signals transmitted from satellites for positioning of a receiver device, providing positions in an absolute, 3-D reference frame. GNSS is the umbrella term for several systems, of which only the U.S. GPS and the Russian GLONASS systems are fully operational at the time of writing. A European (GALILEO) and a Chinese (BeiDou) system are currently under construction and are expected to become operational within the coming years. In this section we will provide a brief outline of the concepts of GNSS measurements. A much more detailed treatment can be found in the work of Misra and Enge (2006).

GNSS consists of a constellation of satellites orbiting the Earth at an altitude of approximately 20,000 km, and specifically designed receiver instruments are used to pick up these signals. The signal can be used to determine the distance, or range, between a receiver and a satellite, which is required to infer the receiver's position. There are two ways to determine the receiver-satellite range: *code phase* measurements and *carrier phase* measurements (Misra and Enge, 2006). Code phase measurements can be used to derive the apparent travel time between the receiver and the satellite, yielding the apparent range between receiver and satellite. Apparent, because satellite and receiver clocks are not synchronized, which means that the true travel time is not known. The difference between the time taken by satellite and receiver depends on the offsets of satellite clock and receiver clock to true time. While the offset, or bias in GNSS terminology, of the satellite clock can be mitigated (by using corrections from continuous reference stations tracking the same satellite), the receiver clock bias can neither be modeled nor be corrected for before positioning. Instead it becomes a fourth unknown in the equations that relate apparent range to the 3-D receiver coordinates. This means that, in order to determine the position of a receiver, at least four satellites need to be tracked at the same time. The position estimate, however, is affected by various error terms like atmospheric propagation delays, multipath arrivals, satellite clock bias and errors in orbital position. Partly, they can be minimized using appropriate models or specific measurement techniques (see Misra and Enge, 2006). An important tool to address these errors are continuously operated GNSS reference stations, which can be used to mitigate errors that are spatially and temporally correlated. For geodetic GNSS measurements in Iceland we are able to resort to a network of continuous GNSS stations both in Iceland and worldwide (Geirsson et al., 2006) .

The accuracy of pseudorange position estimates derived from code phase measurements, however, is on meter level making them unsuitable for geodetic applications.

Carrier phase measurements, on the other hand, can be measured with greater precision because of their shorter signal wavelengths and because of their greater immunity to receiver-related measurement errors, i.e. multipath and receiver noise (Misra and Enge, 2006).

Because of the various errors sources that have to accounted for to obtain millimeter-accuracy is the length in time for which a receiver is deployed at an observation point. An observation time of at least several hours, preferably several days, is required.

In this study we use two different modes of observation to obtain GNSS data: continuously operated GNSS stations, which have the highest accuracy but can only be employed in low numbers due to cost factors, and campaign stations, benchmarks that we observe once per year for at least 48 hours. The former have a high accuracy and full temporal coverage, the latter form a dense network (circa 2–3 stations per square kilometer in the Hengill area, see Paper I) adding good spatial resolution to the measurements. We analyze the data using the GAMIT/GLOBK software combination (Herring et al., 2015) to reduce errors and to obtain precise, absolute positions in the ITRF08 reference frame (Altamimi et al., 2012).

2.2 InSAR

Satellite mounted, synthetic aperture radar (SAR) is a technique to image the Earth's surface. Originally designed for mapping purposes, it was first used on the Seasat satellite, launched in 1978 (e.g. Stewart, 1988). With the launch of ERS-1 in 1991, the technology became easily accessible for the scientific community (see Massonnet et al., 1993).

SAR pulses have a wavelength spectrum between $\sim$3 cm (X-band) and $\sim$25 cm (L-band) and are capable of penetrating cloud cover and (to an extent) vegetation and do not require illumination by the sun unlike optical methods. The different wavelengths have a trade-off between less scatter (longer wavelengths) and better spatial resolution (shorter wavelengths). The satellite emits radar pulses (see Figure 2.1) that are reflected from the ground and part of the reflected signal returns to the satellite where it is recorded. Each SAR image acquired in this way contains amplitude and phase information from scatterers on the ground. If a satellite observes the same ground area at least twice from approximately the same point in orbit at different times, two images can be used to form an interferogram (interferometric SAR, or InSAR). To produce an interferogram, corresponding pixels in the two images are co-registered and the difference in phase is taken. If the scattering properties of a ground element do not vary significantly between acquisitions, the differencing removes the random contributions to the observed phase, leaving nonrandom residuals related to several effects: difference in viewing geometry (different positions in orbit) between acquisitions, different atmospheric conditions, topography and surface deformation that occurred between the two acquisitions. Since we are interested in surface deformation, the other effects need to be removed before we can obtain the desired information. In-depth explanation about InSAR and its application to crustal deformation can be found e.g. in Dzurisin (2007).

In cases where more than two acquisitions for a study area are obtained, we can

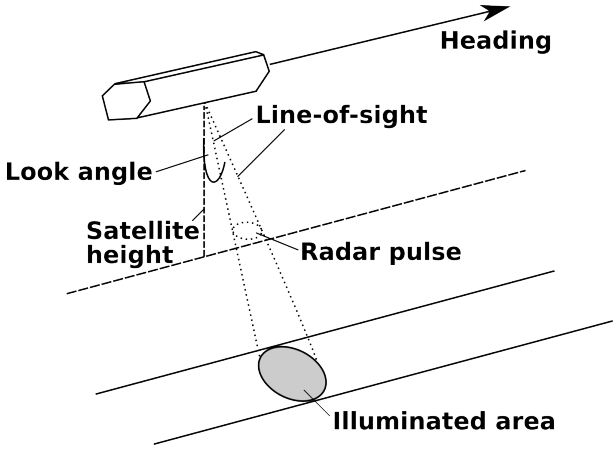

Figure 2.1: Schematic view of a satellite-mounted SAR setup.

apply a multitemporal approach, where multiple interferograms are processed together (Hooper, 2008). This way we are able to cover longer time spans and to reduce decorrelation between images. We use the small-baseline algorithm, implemented in the StaMPS software (Hooper et al., 2012), which identifies pixels that decorrelate little over short time intervals and tracks deformation using these pixels over the time interval of all acquisitions.

In this study we use data from the TerraSAR-X satellite (track 41, ascending in south-to-north orbit). The satellite operates on X-band frequency with a right-looking configuration. Satellite and orbit properties of TerraSAR-X track 41 are given in Table 2.1. InSAR only detects displacements of the ground in one direction, the line-of-sight (LOS) of the satellite. The LOS depends on the trajectory of the satellite and on its viewing angle when imaging the ground (see Table 2.1). For our dataset the average LOS unit vector of the imaged area is $[-0.50\ -0.12\ 0.86]$ (east, north, up). This means that the observations are mostly sensitive to vertical and E-W motion.

Table 2.1: Satellite and orbit configuration of TerraSAR-X track 41.

TerraSAR-X T41	**Configuration**
Mode	StripMap
Heading	346.5° (ascending)
Look direction	right
Look Angle	27.2°–29.5°
Altitude	515 km
Latitude	64.05°
Wavelength	31 mm (X-band)
Resolution	3 m
Covered area	50 km x 30 km

2.3 Deformation modelling

Deformation processes in the shallow crust are often assumed to exhibit an elastic Earth response (e.g. Turcotte and Schubert, 2002; Segall, 2010). In a geothermal reservoir, deformation can either be caused by a change in pore pressure (poroelastic deformation) or a change in temperature (thermoelastic deformation), both of which induce stress and strain in the rock matrix. A common objective in crustal deformation research is to determine properties of a source of deformation, which is an inverse problems (see Section 2.4). This can be done through elastic models that relate subsurface strain to surface displacements.

Most commonly, it is assumed that the deformation in the elastic material is linear and static. For this case, analytical solutions exist that can predict displacements due to strain in a finite source of simple geometry. Analytical solutions are often used in inverse problems because they simplify the problem of finding unique solutions. Using them, we can focus on a reduced number of model parameters and have the advantage of smaller computational demands. Various analytical solutions for different source geometries exist, all of which share the premise of an elastic half-space. To name the most common:

- Point source (Mogi, 1958)
- Rectangular dislocation (Okada, 1985)
- Spherical source (McTigue, 1987)
- Prolate spheroid (Yang et al., 1988)
- Horizonal circular crack (Fialko et al., 2001)

All of these models can be used to relate subsurface volume change, dislocations or pressure changes to surface displacements. Inversion studies of deformation data related to geothermal reservoirs commonly apply the models listed above. For example, point sources are used in the studies of Mossop and Segall (1997), Keiding et al. (2010) and Drouin et al. (2017), rectangular dislocations by Ali et al. (2016) and prolate spheroids by Fialko and Simons (2000) and Keiding et al. (2010), as well as by us in Paper I. The model choice can depend on shape of the deformation signal or on the reservoir geology, i.e. whether a certain model is deemed more appropriate than others (e.g. using rectangular dislocations for reservoir made up of fractured crystalline rock).

A different and more elaborate approach is to solve the elastostatic equations by integrating the point source solution over the modeling domain. This has been applied by e.g. Mossop and Segall (1999), Vasco et al. (2002b) and Masterlark and Lu (2004). This approach allows greater flexibility for the source geometry but requires smoothing of the solution in order to obtain plausible results

If the goal is to invert for more information than source volume change (e.g. change in pore pressure, fluid extraction/injection rates, reservoir compressibility), a poroelastic formulation can be used. This approach is most useful if additional parameter constraints are given, e.g. if reservoir pressure change is known, one can invert for reservoir compressibility and reservoir volume. The full set of poroelastic equations

was introduced by Biot (1941), an analytical solution for a simplified case (a flat reservoir) was given by Geertsma (1966, 1973). For example, this approach was used for modelling of deformation at the Salton Sea geothermal field by Barbour et al. (2016) and for deformation linked to oil production in the Yellow River Delta, China, by Liu et al. (2015).

2.4 Inverse method

In Sections 2.1 amd 2.2 we have described the geodetic data that we use in this study, and in Section 2.3 physical models that can be used to simulate that data. The problem that remains is to find the right parameters that need to be inserted in the model in order to reproduce the observed data. The problem of inferring model parameters through constraints from observed data is called the inverse problem. While the solution of linear inverse problems can be straightforward, non-linear problems, which are more common in Geophysics, are usually solved using stochastic methods, based on random sampling of the model parameter space.

For any given combination of values from the multi-dimensional parameter space we are interested in the likelihood of this parameter combination to explain the observed data. Bayesian inversion methods provide an approach to estimate this likelihood, which is also called the *posterior* probability density function (PDF), $p(\theta|\mathbf{D})$, of the model parameters. The Bayesian approach assumes that the posterior probability of the model parameters is a function of the likelihood function of the data $p(\mathbf{D}|\theta)$ and the prior probability of the model parameters $p(\theta)$, such that:

$$p(\theta|\mathbf{D}) \propto p(\mathbf{D}|\theta)p(\theta) \tag{1}$$

This relation can be interpreted as follows: say, we have a), a prior expectation for the values of model parameters (e.g. a physically appropriate range of values for elastic rock parameters) and b), a set of GNSS data, that we want to model with values from a). Combining only these two sets of information leads us to a new, improved expectation of the model parameter values, the posterior PDF. More detailed explanations on Bayesian methods can be found in Gelman et al. (2014).

The problem is that the posterior distribution can be very complex due to the large number of model parameters that we are dealing with. On top of that, the number of model parameters also creates a vast parameter space that needs to be explored. We need an intelligent approach to sample this parameter space so that we find the distribution that we are looking for without having to sample the infinite amount of possible parameter combinations. This can be achieved with Markov chain Monte Carlo methods (Gelman et al., 2014). Starting from random parameter combinations, the parameter space is sampled in little steps, in a process called a Markov chain. Steps are taken towards parameter combinations that improve the fit between data and model, leading to areas of better fit being sampled more frequently. For a large number of samples the frequency of sampled parameter values is used to determine the posterior probability distribution. A popular Markov chain method is the Metropolis algorithm (Metropolis et al., 1953), which adds a random component to the way steps are taken, this way allowing steps that worsen the fit to the data (though steps toward an improved

fit are still preferred). This brings the advantage that the algorithm is able to escape local peaks in the PDF.

In Papers I and II we use the CATMIP algorithm (Minson et al., 2013), a Metropolis-type algorithm in a Bayesian framework. It runs multiple Markov chains to explore a wider range of the parameter space. The algorithm uses an annealing procedure (similar to simulated annealing, see Kirkpatrick et al., 1983) which lets each Markov chain begin sampling a broader "hot" version of the PDF, which is useful to identify peaks of the posterior PDF, before moving towards the "cold" final PDF. The algorithm is designed to sample complex parameter spaces with multiple peaks without getting stuck in local peaks. The final PDF allows us to estimate arbitrary confidence intervals for each parameter.

3 Summaries of the three research papers

3.1 Paper I: Surface deformation in the Hengill area

We analyse GNSS and InSAR data during 2012–2015 for the Hengill area and find a complex signal, consisting of contributions from geothermal fluid extraction, plate spreading and volcanic deformation. We remove the the plate spreading signal using the model of Árnadóttir et al. (2009), derived from country wide plate motion 1993–2004, which reproduces plate motion in Hengill quite well. After correcting the data for the plate spreading signal, we perform an inversion and find that three sources of volume contraction explain the remaining signal (Figure 3.1). A deep source at ∼7 km depth in between the three volcanic centres in eastern Hengill explains large scale subsidence and far field horizontal GNSS velocities in Hengill. This source is approximately ∼3 km away from the inflating source found for the 1994–1998 uplift episode (Feigl et al., 2000), suggesting that the two signals may be related. Local signals around the Hellisheidi and Nesjavellir power plants can be linked to geothermal fluid extraction from shallow depth, most likely due to pressure decrease in the reservoir with only minor contribution from temperature decrease.

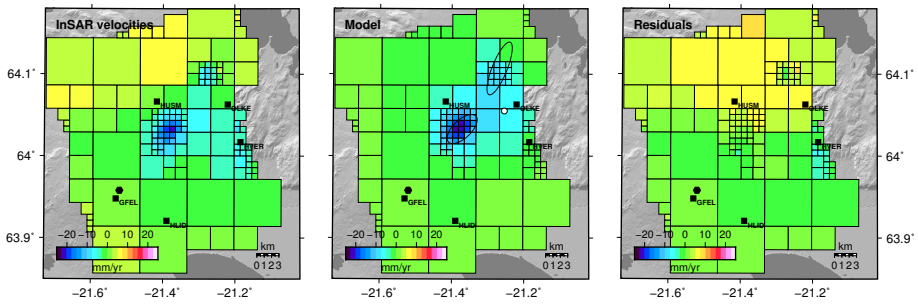

Figure 3.1: (left) Subsampled InSAR velocities 2012–2015 corrected for plate motion, (middle) estimated velocities, and (right) residuals. All in LOS of the satellite. The velocity reference point is denoted by a black hexagon. Black ellipses show surface projections of the spheroidal source locations, the white circle marks the point source.

3.2 Paper II: Injection related deformation and seismicity at Hellisheidi

Waste fluid is re-injected at the Hellisheidi field in order to mitigate pore pressure decrease in the reservoir as well as to dispose of excess fluid. When the injection commenced at Húsmúli in September 2011, an increase in seismicity around and just north of the injection boreholes was observed. The strongest events were two M4 earthquakes occurring on 15 October 2011. The injection is ongoing and periods of increased seismicity occur episodically.

We analyze InSAR data spanning May 2011 to June 2012, as well as horizontal GNSS data from October 2011 to June 2012 and find a signal of expansion, evident both in the InSAR and the GNSS data. We test various models using joint Bayesian optimization of both datasets to find the most likely cause of the deformation. Our modelling indicates that the deformation signal consists of contributions from a spherical source of pressure increase in the seismically active area (the center of which is located at about 0.5–1 km north of the injection site), and from a right-lateral N-S oriented strike-slip fault in the easternmost zone of induced seismicity (Figure 3.2). We interpret this as accumulation of injected water north of the injection site which causes an increase in pore pressure in this area. The increase in pore pressure brings faults in the region closer to failure and we consider it as being the main cause for the increase in seismicity.

The strike-slip source agrees in location, orientation and slip direction with the easternmost zone of seismicity. The depth of 0.7–1.1 km that we obtain for the source, however, is more shallow than the depths inferred for the seismicity which is around 1.5–4.5 km. The geodetic moment inferred from our slip model is also significantly higher than seismic moment released by the earthquakes in the same zone, although this strongly depends on the value of the shear modulus used. These differences, however, mean that we can not conclusively say whether the modelled fault slip is co-seismic or if it is aseismic slip occurring in addition to the earthquakes.

3.3 Paper III: Relationship between fluid extraction and reservoir deformation

Subsidence related to extraction of geothermal fluids is caused by contraction of the reservoir rock. The volume change of the rock due to contraction can be quantified from inversion of geodetic data using deformation models. The obtained reservoir volume change can be related to fluid volume or mass change. The relationship between the two volumes, however, is not simple and depends on the compressibilities of both pore fluid and rock formation, reservoir recharge, as well as various poroelastic material parameters and reservoir characteristics (see Equation 7 in Paper III). In geothermal reservoirs two-phase conditions can exist and it is very difficult to constrain the ratio between liquid and vapour phase. For this reason we propose to compare the reservoir volume change to fluid *mass change* rather than the fluid volume change. Using a stochastic approach, we find that the discrepancy can be explained by different reservoir

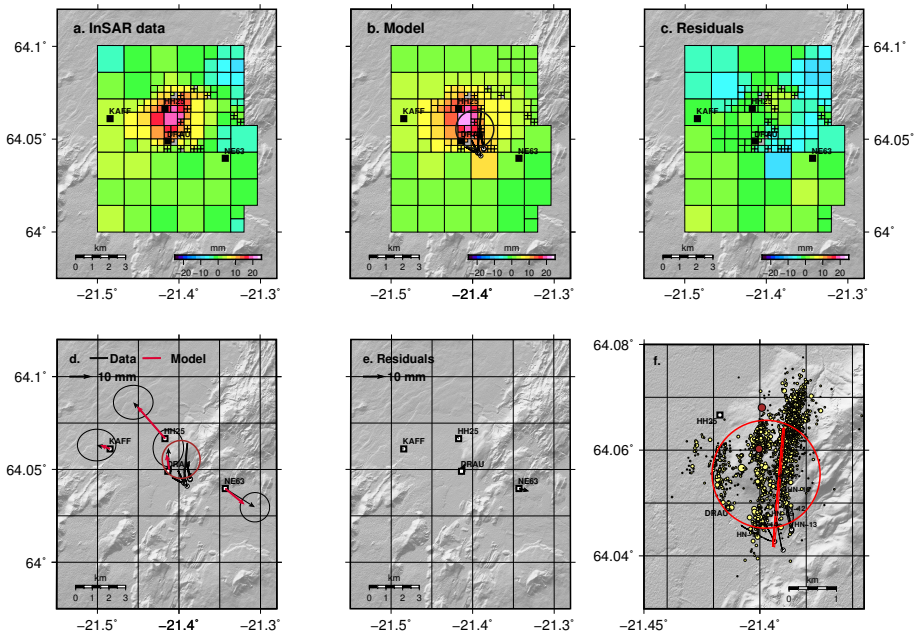

Figure 3.2: Spherical pressure source and rectangular dislocation. InSAR data (a), model (b) and residuals (c) in the top row. All in LOS of the satellite. GPS data, model (d) and residuals (e), as well as the location of the sources relative to the seismicity and the locations of the injection boreholes (f) in the bottom row. The rectangle marks the dislocation (bold line is the upper edge), the circle the spherical pressure source.

properties and that, in particular, the compressibilities of pore fluid and reservoir rock have a significant effect. For each case, a low reservoir bulk modulus ($K \lesssim 5\,\mathrm{GPa}$) combined with a low two-phase fluid bulk modulus offer a good explanation for the reported deformation.

4 Conclusions

We analysed geodetic data in the Hengill area during 2011–2012 (Paper II) and 2012–2015 (Paper I), and find that Hengill exhibits deformation caused by plate spreading, extraction and injection of geothermal fluids at two power plants, as well as deformation in eastern Hengill that is possibly related to the Hengill volcanic centre. While we can use existing models to reproduce the plate spreading signal quite well, the eastern Hengill deformation is not as easily explained. The point source that we find is at a similar depth as the source found for the 1994–1998 uplift episode, albeit with a horizontal distance of $\sim$3 km. The 1994–1998 episode was interpreted to be caused by an intrusion, the volume decrease due to contraction during 2012–2015, however, is too large to be caused by contraction of an intrusion of the given size. Both spatial and temporal variations might affect this signal and to fully understand the process the whole sequence of deformation should be analyzed. For the deformation data from 2011 to 2012 we find that the uplift signal close to Húsmúli injection site is likely caused by an increase in pore pressure induced by the nearby fluid injection. We suggest that the pore pressure increase is also the reason for the increase in seismicity that began when the re-injection of waste fluids at Húsmúli started.

The deformation around the geothermal power plants can be explained by observed pressure drawdown in the reservoirs. The inversion can yield good insight into the location and the extent of the deformation source. We can identify pressure drawdown as the main contribution to the deformation but we can not rule out that temperature decrease in the upper part of the reservoir plays a role as well.

The interplay between pressure change and temperature change, the uncertainty about fluid phase distribution the unknown structure, geometry, extent and level of heterogeneity all add up to making modeling of geothermal systems a complex problem. While we can gain valuable information about geothermal reservoirs using inverse methods with simple deformation models, a lot of the complexities remain unaddressed. In order to fully capture the intricacies of geothermal reservoir processes, numerical models are necessary. The advantage of large man-made operations like the exploitation of a geothermal resource, is that we have a large amount of additional information to constrain numerical models. In-situ borehole measurements of pressure and temperature change, tracer tests to study flow paths and surface deformation data can all complement each other. The inversion approach can be complemented with forward models of pressure- and temperature distribution within the reservoir, coupled with elastic deformation models. Using inversion results from geodetic observation to supplement existing reservoir models can add important constraints to fluid flow and fluid storage in the reservoir, and good knowledge about pressure and temperature distributions can in turn enhance deformation models.

References

Ágústsson, K., Kristjánsdóttir, S., Flóvenz, Ó. G., and Gudmundsson, O. (2015). Induced Seismic Activity during Drilling of Injection Wells at the Hellisheiði Power Plant, SW Iceland. In *Proceedings World Geothermal Congress 2015, Melbourne, Australia, 19–25 April 2015*.

Ali, S. T., Akerley, J., Baluyut, E. C., Cardiff, M., Davatzes, N. C., Feigl, K. L., Foxall, W., Fratta, D., Mellors, R. J., Spielman, P., Wang, H. F., and Zemach, E. (2016). Time-series analysis of surface deformation at Brady Hot Springs geothermal field (Nevada) using interferometric synthetic aperture radar. *Geothermics*, 61:114–120.

Allis, R., Bromley, C., and Currie, S. (2009). Update on subsidence at the Wairakei–Tauhara geothermal system, New Zealand. *Geothermics*, 38(1):169–180.

Altamimi, Z., Metivier, I., and Collileux, X. (2012). ITRF2008 plate motion model. *J. Geophys. Res.*, 117.

Árnadóttir, T., Hreinsdóttir, S., Gudmundsson, G., Einarsson, P., Heinert, M., and Völksen, C. (2001). Crustal deformation measured by GPS in the South Iceland Seismic Zone due to two large earthquakes in June 2000. *Geophys. Res. Lett*, 28(21):4031–4033.

Árnadóttir, T., Jónsson, S., Pollitz, F. F., Jiang, W., and Feigl, K. L. (2005). Postseismic deformation following the June 2000 earthquake sequence in the south Iceland seismic zone. *Journal of Geophysical Research: Solid Earth*, 110(B12).

Árnadóttir, T., Lund, B., Jiang, W., Geirsson, H., Björnsson, H., Einarsson, P., and Sigurdsson, T. (2009). Glacial rebound and plate spreading: results from the first countrywide GPS observations in Iceland. *Geophys. J. Int.*, 177:691–716.

Auriac, A., Spaans, K. H., Sigmundsson, F., Hooper, A., Schmidt, P., and Lund, B. (2013). Iceland rising: Solid earth response to ice retreat inferred from satellite radar interferometry and visocelastic modeling. *Journal of Geophysical Research: Solid Earth*, 118(4):1331–1344.

Baisch, S., Vörös, R., Rothert, E., Stang, H., Jung, R., and Schellschmidt, R. (2010). A numerical model for fluid injection induced seismicity at Soultz-sous-Forêts. *International Journal of Rock Mechanics and Mining Sciences*, 47(3):405–413.

Barbour, A. J., Evans, E. L., Hickman, S. H., and Eneva, M. (2016). Subsidence rates at the southern Salton Sea consistent with reservoir depletion. *Journal of Geophysical Research: Solid Earth*, 121(7):5308–5327.

Bessason, B., Ólafsson, E., Gunnarsson, G., Flovenz, O., Jakobsdóttir, S., Björnsson, S., and Árnadóttir, T. (2012). Verklag vegna örvaðrar skjálftavirkni í jarðhitakerfum. Technical report, Orkuveita Reykjavíkur, Reykjavik, Iceland. [In Icelandic].

Biot, M. A. (1941). General theory of three-dimensional consolidation. *Journal of Applied Physics*, 12(2):155–164.

Carnec, C. and Fabriol, H. (1999). Monitoring and modeling land subsidence at the Cerro Prieto geothermal field, Baja California, Mexico, using SAR interferometry. *Geophysical Research Letters*, 26(9):1211–1214.

Clifton, A. E., Pagli, C., Jónsdóttir, J. F., Eythorsdóttir, K., and Vogfjörð, K. (2003). Surface effects of triggered fault slip on Reykjanes Peninsula, SW Iceland. *Tectonophysics*, 369(3):145–154.

Clifton, A. E., Sigmundsson, F., Feigl, K. L., Guðmundsson, G., and Árnadóttir, T. (2002). Surface effects of faulting and deformation resulting from magma accumulation at the Hengill triple junction, SW Iceland, 1994–1998. *J. Volc. Geotherm. Res.*, 115:233–255.

Decker, R. W., Einarsson, P., and Mohr, P. A. (1971). Rifting in Iceland: New geodetic data. *Science*, 173(3996):530–533.

Deichmann, N. and Giardini, D. (2009). Earthquakes induced by the stimulation of an enhanced geothermal system below Basel (Switzerland). *Seismological Research Letters*, 80(5):784–798.

DeMets, C., Gordon, R. G., and Argus, D. F. (2010). Geologically current plate motions. *Geophysical Journal International*, 181(1):1–80.

Dini, I. and Rossi, A. (1990). Monitoring ground elevation changes in the Larderello geothermal region, Tuscan, Italy. In *Geothermal Resources Council TRANSACTIONS*, volume 14.

Drouin, V., Heki, K., Sigmundsson, F., Hreinsdóttir, S., and Ófeigsson, B. G. (2016). Constraints on seasonal load variations and regional rigidity from continuous GPS measurements in Iceland, 1997–2014. *Geophysical Journal International*, 205(3):1843–1858.

Drouin, V., Sigmundsson, F., Verhagen, S., Ófeigsson, B. G., Spaans, K., and Hreinsdóttir, S. (2017). Deformation at Krafla and Bjarnarflag geothermal areas, Northern Volcanic Zone of Iceland, 1993–2015. *Journal of Volcanology and Geothermal Research*, 344:92–105.

Dzurisin, D. (2007). *Volcano Deformation*. Springer.

Einarsson, P. (1991). Earthquakes and present-day tectonism in Iceland. *Tectonophysics*, 189(1):261–279.

Einarsson, P. (2008). Plate boundaries, rifts and transforms in Iceland. *Jökull*, 58(12):35–58.

Ellsworth, W. L. (2013). Injection-induced earthquakes. *Science*, 341(6142):1225942.

Evans, K. F., Zappone, A., Kraft, T., Deichmann, N., and Moia, F. (2012). A survey of the induced seismic responses to fluid injection in geothermal and CO_2 reservoirs in Europe. *Geothermics*, 41:30–54.

Feigl, K. L., Gasperi, J., Sigmundsson, F., and Rigo, A. (2000). Crustal deformation near Hengill volcano, Iceland 1993–1998: Coupling between magmatic activity and faulting inferred from elastic modeling of satellite radar interferograms. *J. Geophys. Res.*, 105(25):655–25.

Fialko, Y., Khazan, Y., and Simons, M. (2001). Deformation due to a pressurized horizontal circular crack in an elastic half-space, with applications to volcano geodesy. *Geophysical Journal International*, 146(1):181–190.

Fialko, Y. and Simons, M. (2000). Deformation and seismicity in the Coso geothermal area, Inyo County, California: Observations and modeling using satellite radar

interferometry. *J. Geophys. Res.*, 105:21,781–21,793.

Foulger, G., Bilham, R., Morgan, W. J., and Einarsson, P. (1987). The Iceland GPS geodetic field campain 1986. *Eos, Transactions American Geophysical Union*, 68(52):1809–1818.

Foulger, G. R. (1988). Hengill Triple Junction, SW Iceland 1. Tectonic Structure and the Spatial and Temporal Distribution of Local Earthquakes. *Journal of Geophysical Research: Solid Earth*, 93(B11):13493–13506.

Foulger, G. R., Jahn, C.-H., Seeber, G., Einarsson, P., Julian, B. R., and Heki, K. (1992). Post-rifting stress relaxation at the divergent plate boundary in Northeast Iceland. *Nature*, 358(6386):488–490.

Franzson, H., Gunnlaugsson, E., Árnason, K., Sæmundsson, K., Steingrímsson, B., and Harðarson, B. S. (2010). The Hengill geothermal system, conceptual model and thermal evolution. In *Proceedings World Geothermal Congress 2010*.

Geertsma, J. (1966). Problems of rock mechanics in petroleum production engineering. In *Proceedings of the 1st ISRM Congress*. International Society for Rock Mechanics.

Geertsma, J. (1973). Land subsidence above compacting oil and gas reservoirs. *Journal of Petroleum Technology*, 25(06):734–744.

Geirsson, H., Árnadóttir, T., Völksen, C., Jiang, W., Sturkell, E., Villemin, T., Einarsson, P., Sigmundsson, F., and Stefánsson, R. (2006). Current plate movements across the Mid-Atlantic Ridge determined from 5 years of continuous GPS measurements in Iceland. *Journal of Geophysical Research: Solid Earth*, 111(B9).

Geirsson, H., LaFemina, P., Arnadottir, T., Sturkell, E., Sigmundsson, F., Travis, M., Schmidt, P., Lund, B., Hreinsdottir, S., and Bennett, R. (2012). Volcano deformation at active plate boundaries: Deep magma accumulation at Hekla volcano and plate boundary deformation in south Iceland. *Journal of Geophysical Research: Solid Earth*, 117(B11).

Gelman, A., Carlin, J. B., Stern, H. S., Dunson, D. B., Vehtari, A., and Rubin, D. B. (2014). *Bayesian Data Analysis*. CRC Press Boca Raton, FL, Third edition.

Glowacka, E., González, J., and Fabriol, H. (1999). Recent vertical deformation in Mexicali valley and its relationship with tectonics, seismicity, and the exploitation of the Cerro Prieto geothermal field, Mexico. *Pure and Applied Geophysics*, 156(4):591–614.

Grapenthin, R., Sigmundsson, F., Geirsson, H., Arnadóttir, T., and Pinel, V. (2006). Icelandic rhythmics: Annual modulation of land elevation and plate spreading by snow load. *Geophysical Research Letters*, 33(24).

Hatton, J. (1970). Ground subsidence of a geothermal field during exploitation. *Geothermics*, 2:1294–1296.

Healy, J. H., Rubey, W. W., Griggs, D. T., and Raleigh, C. B. (1968). The Denver Earthquakes. *Science*, 161(3848):1301–1310.

Heimlich, C., Gourmelen, N., Masson, F., Schmittbuhl, J., Kim, S.-W., and Azzola, J. (2015). Uplift around the geothermal power plant of Landau (Germany) as observed by InSAR monitoring. *Geothermal Energy*, 3(1):2.

Herring, T. A., King, R. W., Floyd, M. A., and McClusky, S. C. (2015). Introduction to GAMIT/GLOBK, release 10.6. Technical report, Mass. Inst. Technol., Cambridge, MA, USA.

Hjartardóttir, Á. R., Einarsson, P., and Björgvinsdóttir, S. G. (2016). Fissure swarms

and fracture systems within the Western Volcanic Zone, Iceland–Effects of spreading rates. *Journal of Structural Geology*, 91:39–53.

Hooper, A. (2008). A multi-temporal insar method incorporating both persistent scatterer and small baseline approaches. *Geophys. Res. Lett.*, 35.

Hooper, A., Bekaert, D., Spaans, K., and Arıkan, M. (2012). Recent advances in SAR interferometry time series analysis for measuring crustal deformation. *Tectonophysics*, 514:1–13.

Hreinsdóttir, S., Árnadóttir, T., Decriem, J., Geirsson, H., Tryggvason, A., Bennett, R. A., and LaFemina, P. (2009). A complex earthquake sequence captured by the continuous GPS network in SW Iceland. *Geophysical Research Letters*, 36.

Jónsson, S., Segall, P., Pedersen, R., and Björnsson, G. (2003). Post-earthquake ground movements correlated to pore-pressure transients. *Nature*, 424(6945):179–183.

Keiding, M., Árnadóttir, T., Jónsson, S., Decriem, J., and Hooper, A. (2010). Plate boundary deformation and man-made subsidence around geothermal fields on the Reykjanes Peninsula, Iceland. *J. Volc. Geotherm. Res.*, 194:139–149.

Kirkpatrick, S., Gelatt, C. D., and Vecchi, M. P. (1983). Optimization by simulated annealing. *Science*, 220(4598):671–680.

Liu, P., Li, Q., Li, Z., Hoey, T., Liu, Y., and Wang, C. (2015). Land subsidence over oilfields in the Yellow River Delta. *Remote Sensing*, 7(2):1540–1564.

Lofgren, B. E. (1978). Monitoring crustal deformation in the Geysers-Clear Lake geothermal area, California. Technical report, Geological Survey, Sacramento, CA (USA).

Massonnet, D., Rossi, M., Carmona, C., Adragna, F., Peltzer, G., Feigl, K., and Rabaute, T. (1993). The displacement field of the Landers earthquake mapped by radar interferometry. *Nature*, 364(6433):138–142.

Masterlark, T. and Lu, Z. (2004). Transient volcano deformation sources imaged with interferometric synthetic aperture radar: application to Seguam Island, Alaska. *Journal of Geophysical Research: Solid Earth*, 109(B1).

McGarr, A., Simpson, D., and Seeber, L. (2002). Case Histories of Induced and Triggered Seismicity. In *International Handbook of Earthquake & Engineering Seismology. Volume 81A*, pages 647–664.

McTigue, D. F. (1987). Elastic stress and deformation near a finite spherical magma body: Resolution of the point source paradox. *J. Geophys. Res.*, 92:12,931–12,940.

Metropolis, N., Rosenbluth, A. W., Rosenbluth, M. N., Teller, A. H., and Teller, E. (1953). Equation of state calculations by fast computing machines. *The journal of chemical physics*, 21(6):1087–1092.

Minson, S. E., Simons, M., and Beck, J. L. (2013). Bayesian inversion for finite fault earthquake source models I–theory and algorithm. *Geophys. J. Int.*, 194:1701–1726.

Misra, P. and Enge, P. (2006). *Global Positioning System: Signals, Measurements and Performance*. Ganga-Jamuna Press, 2nd edition.

Mogi, K. (1958). Relations between the eruptions of various volcanoes and the deformations of the ground surfaces around them. *Bulletin of the Earthquake Reasearch Institute, University of Tokyo*, 36:99–134.

Mossop, A. and Segall, P. (1997). Subsidence at The Geysers geothermal field, N. California from a comparison of GPS and leveling surveys. *Geophysical Research Letters*, 24(14):1839–1842.

Mossop, A. and Segall, P. (1999). Volume strain within the Geysers geothermal field. *Journal of Geophysical Research: Solid Earth*, 104(B12):29113–29131.

Nielsen, N. (1930). Tektonik und Vulkanismus Islands unter Berücksichtigung der Wegener-Hypothese. *Geologische Rundschau*, 21:347–349. [In German].

Nordquist, G., Protacio, J. A. P., and Acuña, J. A. (2004). Precision gravity monitoring of the Bulalo geothermal field, Philippines: independent checks and constraints on numerical simulation. *Geothermics*, 33(1):37–56.

Okada, Y. (1985). Surface deformation due to shear and tensile faults in a half-space. *Bulletin of the Seismological Society of America*, 75(4):1135–1154.

Ottemöller, L., Nielsen, H., Atakan, K., Braunmiller, J., and Havskov, J. (2005). The 7 may 2001 induced seismic event in the Ekofisk oil field, North Sea. *Journal of Geophysical Research: Solid Earth*, 110(B10).

Pedersen, R., Jónsson, S., Árnadóttir, T., Sigmundsson, F., and Feigl, K. L. (2003). Fault slip distribution of two June 2000 M_w 6.5 earthquakes in South Iceland estimated from joint inversion of InSAR and GPS measurements. *Earth and Planetary Science Letters*, 213(3):487–502.

Pedersen, R., Sigmundsson, F., Feigl, K. L., and Árnadóttir, T. (2001). Coseismic interferograms of two Ms= 6.6 earthquakes in the South Iceland Seismic Zone, June 2000. *Geophysical Research Letters*, 28(17):3341–3344.

Raleigh, C. B., Healy, J. H., and Bredehoeft, J. D. (1976). An Experiment in Earthquake Control at Rangely, Colorado. *Science*, 191(4233):1230–1237.

Rutqvist, J. and Oldenburg, C. M. (2008). Analysis of injection-induced microearthquakes in a geothermal steam reservoir, the Geysers Geothermal Feld, California. *Lawrence Berkeley National Laboratory*.

Sæmundsson, K. (1967). Vulkanismus und Tektonik des Hengill-Gebietes in SW-Island. *Acta Nat. Isl.*, 2:105p. [In German].

Segall, P. (1989). Earthquakes triggered by fluid extraction. *Geology*, 17(10):942–946.

Segall, P. (2010). *Earthquake and Volcano Deformation*. Princeton University Press.

Shirzaei, M., Ellsworth, W. L., Tiampo, K. F., González, P. J., and Manga, M. (2016). Surface uplift and time-dependent seismic hazard due to fluid injection in eastern Texas. *Science*, 353(6306):1416–1419.

Sigmundsson, F., Einarsson, P., and Bilham, R. (1992). Magma chamber deflation recorded by the Global Positioning System: The Hekla 1991 eruption. *Geophysical Research Letters*, 19(14):1483–1486.

Sigmundsson, F., Hooper, A., Hreinsdóttir, S., Vogfjörd, K. S., Ófeigsson, B. G., Heimisson, E. R., Dumont, S., Parks, M., Spaans, K., Gudmundsson, G. B., Drouin, V., Árnadóttir, T., Jónsdóttir, K., Gudmundsson, M. T., Högnadóttir, T., Fridriksdóttir, H. M., Hensch, M., Einarsson, P., Magnússon, E., Samsonov, S., Brandsdóttir, B., White, R. S., Ágústsdóttir, T., Greenfield, T., Green, R. G., Hjartardóttir, Á. R., Pedersen, R., Bennett, R. A., Geirsson, H., La Femina, P. C., Björnsson, H., Pálsson, F., Sturkell, E., Bean, C. J., Möllhoff, M., Braiden, A. K., and Eibl, E. P. S. (2015). Segmented lateral dyke growth in a rifting event at Bárðarbunga volcanic system, Iceland. *Nature*, 517(7533):191–195.

Sigmundsson, F., Vadon, H., and Massonnet, D. (1997). Readjustment of the Krafla spreading segment to crustal rifting measured by satellite radar interferometry. *Geophysical Research Letters*, 24(15):1843–1846.

Simpson, D. W., Leith, W. S., and Scholz, C. H. (1988). Two types of reservoir-induced seismicity. *Bulletin of the Seismological Society of America*, 78(6):2025–2040.

Steigerwald, L. (2017). The Hengill Triple Junction, Iceland: Classification of Tectonic Surface Features. Master's thesis, University of Iceland.

Stewart, R. H. (1988). Seasat: Results of the Mission. *Bulletin American Meteorological Society*, 69(12):1441–1447.

Sturkell, E., Sigmundsson, F., Geirsson, H., Ólafsson, H., and Theodórsson, T. (2008). Multiple volcano deformation sources in a post-rifting period: 1989–2005 behaviour of Krafla, Iceland constrained by levelling, tilt and GPS observations. *Journal of Volcanology and Geothermal Research*, 177(2):405–417.

Tryggvason, E. (1968). Measurement of surface deformation in Iceland by precision leveling. *Journal of Geophysical Research*, 73(22):7039–7050.

Tryggvason, E. (1994). Observed ground deformation at Hekla, Iceland prior to and during the eruptions of 1970, 1980–1981 and 1991. *Journal of Volcanology and Geothermal Research*, 61(3-4):281–291.

Turcotte, D. L. and Schubert, G. (2002). *Geodynamics*. Cambridge University Press, 2nd edition.

Vadon, H. and Sigmundsson, F. (1997). Crustal deformation from 1992 to 1995 at the Mid-Atlantic Ridge, southwest Iceland, mapped by satellite radar interferometry. *Science*, 275(5297):194–197.

Vasco, D. W., Karasaki, K., and Nakagome, O. (2002a). Monitoring production using surface deformation: the Hijiori test site and the Okuaizu geothermal field, Japan. *Geothermics*, 31(3):303–342.

Vasco, D. W., Wicks Jr, C., Karasaki, K., and Marques, O. (2002b). Geodetic imaging: reservoir monitoring using satellite interferometry. *Geophysical Journal International*, 149(3):555–571.

Yang, X. M., Davis, P. M., and Dieterich, J. H. (1988). Deformation from inflation of a dipping finite prolate spheroid in an elastic half-space as a model for volcanic stressing. *Journal of Geophysical Research: Solid Earth*, 93(B5):4249–4257.

Yerkes, R. F. and Castle, R. O. (1976). Seismicity and faulting attributable to fluid extraction. *Engineering Geology*, 10(2-4):151–167.

Zang, A., Oye, V., Jousset, P., Deichmann, N., Gritto, R., McGarr, A., Majer, E., and Bruhn, D. (2014). Analysis of induced seismicity in geothermal reservoirs – An overview. *Geothermics*, 52:6–21.

Zoback, M. D. and Harjes, H.-P. (1997). Injection-induced earthquakes and crustal stress at 9 km depth at the KTB deep drilling site, Germany. *Journal of Geophysical Research: Solid Earth*, 102(B8):18477–18491.

Published articles and submitted manuscripts

Paper I

Anthropogenic and natural ground deformation in the Hengill geothermal area, Iceland

Daniel Juncu, Thóra Árnadóttir, Andy Hooper and Gunnar Gunnarsson. 2017
Journal of Geophysical Research: Solid Earth, **122(1)**, 692–709. doi:10.1002/2016JB013626.

AGU PUBLICATIONS

JGR

Journal of Geophysical Research: Solid Earth

RESEARCH ARTICLE
10.1002/2016JB013626

Anthropogenic and natural ground deformation in the Hengill geothermal area, Iceland

D. Juncu[1], Th. Árnadóttir[1], A. Hooper[2], and G. Gunnarsson[3]

[1]Nordic Volcanological Center, Institute of Earth Sciences, University of Iceland, Reykjavík, Iceland, [2]COMET, School of Earth and Environment, University of Leeds, Leeds, UK, [3]OR—Reykjavík Energy, Reykjavík, Iceland

Key Points:
- Geodetic data show man-made subsidence in the geothermal fields in the Hengill area, Iceland, due to extraction of fluids
- Evidence that pressure drawdown is the driving mechanism behind the observed surface subsidence around the two Hengill power plants

Supporting Information:
- Table S1
- Table S2

Correspondence to:
D. Juncu,
daj22@hi.is

Citation:
Juncu, D., T. Árnadóttir, A. Hooper, and G. Gunnarsson (2017), Anthropogenic and natural ground deformation in the Hengill geothermal area, Iceland, *J. Geophys. Res. Solid Earth*, *122*, 692–709, doi:10.1002/2016JB013626.

Received 7 OCT 2016
Accepted 13 DEC 2016
Accepted article online 16 DEC 2016
Published online 28 JAN 2017

Abstract We investigate crustal deformation due to the extraction of water and steam from a high-enthalpy geothermal reservoir; a common occurrence, yet not well understood. The cause of this deformation can be a change in pressure or in temperature in the reservoir, both of which can be caused by extraction or injection of geothermal fluids. Our study area, the Hengill mountains in SW Iceland, is an active volcanic center and a plate triple junction that hosts two power plants producing geothermal energy. This combination of natural and anthropogenic processes causes a complex displacement field at the surface. We analyze geodetic data—Global Navigation Satellite System and Interferometric Synthetic Aperture Radar—to obtain the surface velocity field, which we then simulate using an inverse modeling approach. We focus on the deformation around the geothermal power plants but need to model the regional tectonic and volcanic deformation as well, because the signals are overlapping. We find that plate motion and a deep contracting body can explain the broad scale signal in the area. Local deformation near the two power plants, Hellisheidi and Nesjavellir, can be explained by extraction of geothermal fluids. We estimate reservoirs extending from 0.6 to 3.0 km depth at Hellisheidi, and 1.0 to 3.0 km depth at Nesjavellir for observed pressure decrease rates of 0.25 MPa/yr and 0.1 MPa/yr, respectively. We find that the main cause for the subsidence in the geothermal area is the observed pressure drawdown.

1. Introduction

Deformation of the Earth's crust caused by utilization of natural resources has been observed in many places. Examples include the following: exploitation of hydrocarbons [e.g., *Fielding et al.*, 1998], groundwater [e.g., *Chi and Reilinger*, 1984], and geothermal fluids [e.g., *Segall*, 1985; *Mossop and Segall*, 1997; *Allis and Zhan*, 2000; *Fialko and Simons*, 2000; *Keiding et al.*, 2010; *Vasco et al.*, 2013; *Jeanne et al.*, 2014; *Ali et al.*, 2016; *Drouin*, 2016; *Barbour et al.*, 2016]. Here we present a case study of crustal deformation driven by the use of a high-temperature geothermal field, a phenomenon that is not well understood. One challenge is to identify the cause of the deformation, as the volume change of a geothermal subsurface reservoir has been assumed to be caused mainly by (a) changes in pore/fracture pressure due to extraction or injection of fluids [e.g., *Allis and Zhan*, 2000; *Barbour et al.*, 2016] or (b) changes in temperature of the host rock due to production or injection [e.g., *Ali et al.*, 2016].

Mount Hengill is a volcanic system in SW Iceland, located on the plate boundary between the North American and Eurasian plates. More precisely, it marks the triple junction between the spreading-type Reykjanes Peninsula (RP), the Western Volcanic Zone (WVZ), and the transform-type South Iceland Seismic Zone (SISZ), see Figure 1. The volcanic basement hosts a high-temperature field harnessed by two power plants: Hellisheidi and Nesjavellir. The local geology is complex and composed of highly fractured interbedded hyaloclastite and lava formations [*Franzson et al.*, 2010; *Sæmundsson*, 1967]. There are many normal faults orientated along the SW-NE trending fissure swarm, as well as active N-S strike-slip faults [*Clifton et al.*, 2002].

Due to its vicinity to the SISZ, many earthquakes are recorded around Hengill. In May 2008 a seismic sequence with two M_W 6 earthquakes close to the Ölfus River (see Figure 2) occurred in the western end of the SISZ [*Hreinsdóttir et al.*, 2009]. Coseismic deformation from the two main events could be observed throughout the Hengill range [*Decriem et al.*, 2010] and postseismic deformation affected the surrounding areas during the years following the ruptures [*Geirsson et al.*, 2010]. The 2008 events are considered a continuation of a seismic sequence that started with two earthquakes in 2000 farther east in the SISZ, with moment magnitudes of 6.4–6.5 [e.g., *Árnadóttir et al.*, 2001; *Pedersen et al.*, 2003; *Decriem et al.*, 2010]. Earthquake sequences

AGU Journal of Geophysical Research: Solid Earth 10.1002/2016JB013626

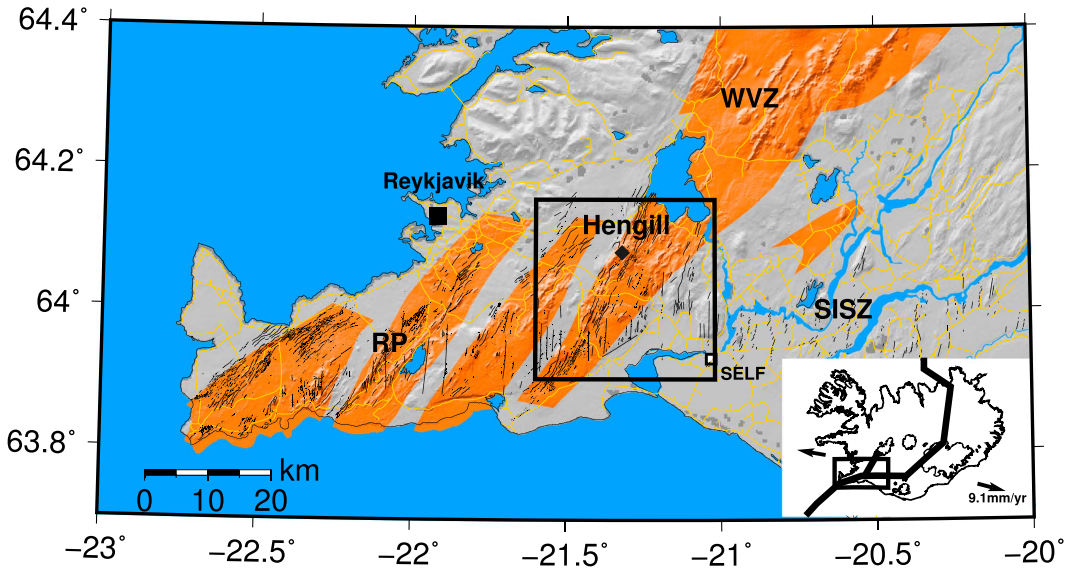

Figure 1. Southwest Iceland and the study area around Mount Hengill. Orange areas denote fissure swarms. Surface faults are shown as black lines and are taken from *Clifton et al.* [2002] and *Einarsson* [2008]. The small map of Iceland in the bottom right shows the location of plate boundaries taken from *Árnadóttir et al.* [2009] and plate velocities calculated using the MORVEL model [*DeMets et al.*, 2010].

in the SISZ recur at average intervals of 80–100 years, the last sequences in 1732–1734, 1784, and 1896 [*Einarsson*, 1991].

Hengill experienced volcanic unrest, with an increase in earthquake activity and uplift, between 1993 and 1998 [*Feigl et al.*, 2000; *Sigmundsson et al.*, 1997]. Seismic activity was strongly increased and climaxed in two earthquakes in June and November 1998 with magnitudes of M_W 5.4 and 5.1, respectively [*Vogfjörd and Slunga*, 2003; *Jakobsdóttir*, 2008]. *Feigl et al.* [2000] examined Interferometric Synthetic Aperture Radar (InSAR) data and found surface uplift rates of up to 19 mm/yr, which they interpreted to have been caused by pressure increase in a magma source at 7 km depth (shown with a yellow diamond in Figure 2).

Magmatic intrusions are the energy source for the geothermal fields in Hengill. Two power plants have been constructed to harness this resource. Nesjavellir has been operational since 1990 with an extraction rate of around 5 Mton/yr (water-steam mixture) in the first year and an average rate of around 16 Mton/yr in 2012–2015 [*Gunnlaugsson*, 2016a]. At Hellisheidi the production started in 2006 with a rate of 7 Mton/yr and was increased to an average rate of 38 Mton/yr in 2012–2015 [*Gunnlaugsson*, 2016b]. To maintain reservoir pressure, wastewater reinjection is being done at Hellisheidi, most of which around Húsmúli. The injection at this site received special attention for having triggered several earthquake swarms including two M_l 3.8 earthquakes in October 2011, a few weeks after it was initiated with a flow rate of around 550 l/s [*Halldorsson et al.*, 2012]. The total injection at Hellisheidi was on average 22 Mton in 2012–2015, of which 13 Mton were injected at Húsmúli [*Gunnlaugsson*, 2016b].

To gain a better understanding of the deformation in the Hengill area, we apply models that simulate the elastic response of the rock to pressure changes in the geothermal reservoir. We combine these models with a nonlinear inversion algorithm to find the best match of modeled and observed surface displacements. The problem in the Hengill area, however, is that there are several different processes that cause surface motion,

AGU Journal of Geophysical Research: Solid Earth 10.1002/2016JB013626

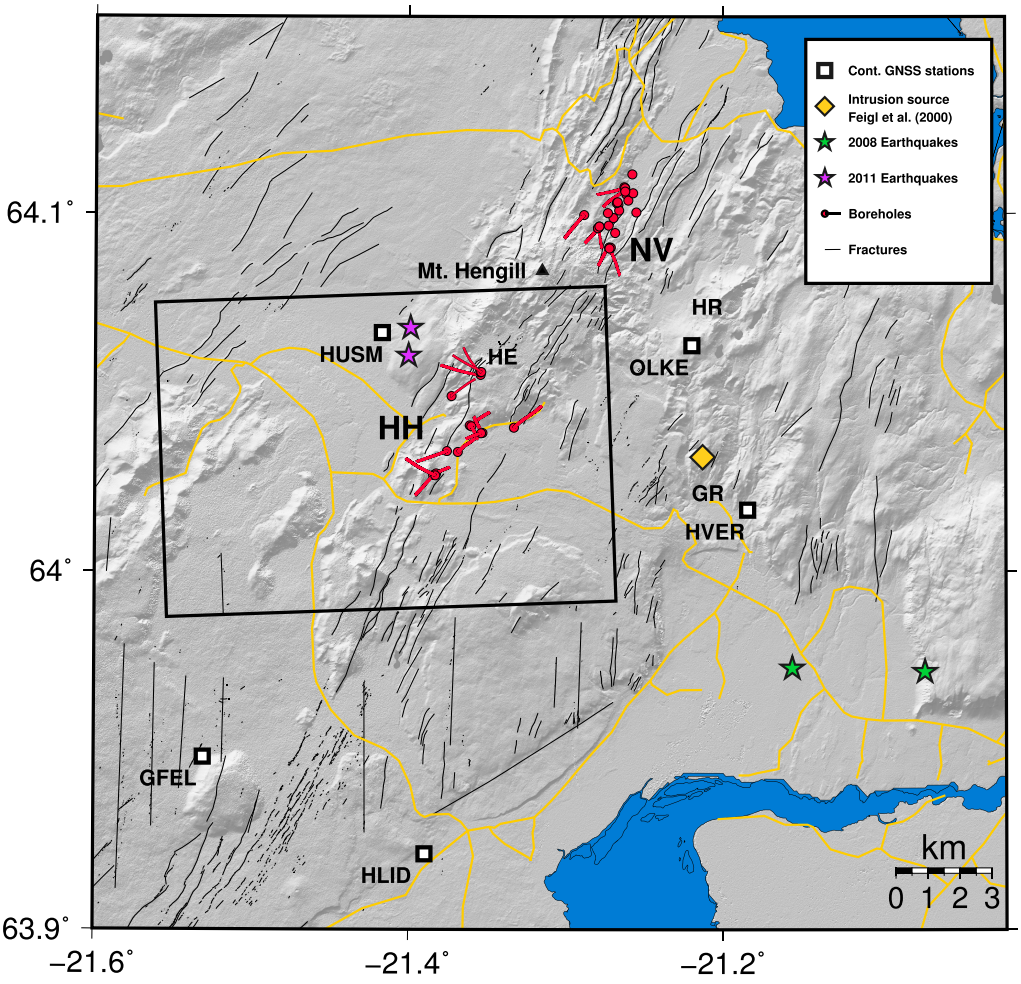

Figure 2. The Hengill area. HH denotes the Hellisheidi area, NV the Nesjavellir area. Continuous GNSS stations (white squares), mapped surface fractures (black lines) and the largest earthquakes in the area since 2008 (green and purple stars). The most productive boreholes at Hellisheidi and Nesjavellir are marked by red circles and lines. The black rectangle outlines the area of Figure 11. The three central volcanoes Hengill, Hrómundartindur, and Grensdalur are marked by HE, HR, and GR, respectively. The magmatic intrusion inferred by *Feigl et al.* [2000] is denoted with a yellow diamond.

in addition to the geothermal signal. In order to adequately study the local signals, we need a modeling approach that accounts for the regional deformation signal.

We concentrate our study on deformation during 2012–2015, as the production was fairly constant during this time. This also minimizes the influence of postseismic deformation from the two M 6 2008 earthquakes and excludes coseismic deformation from the two M_l 3.8 Húsmúli earthquakes in 2011. Also, we do not expect postseismic deformation from the small 2011 events after mid-2012, as confirmed by the continuous Global Navigation Satellite System (GNSS) station HUSM.

AGU Journal of Geophysical Research: Solid Earth 10.1002/2016JB013626

2. Observables

2.1. GNSS Data

We use two different modes of GNSS observations: continuous and campaign observations. With the former term we refer to GNSS stations that are installed in the field continuously and whose daily station positions we calculate from 24 h of measurements. Campaign stations were measured during annual campaigns (in 2012, 2013, 2014, and 2015) conducted by the Institute of Earth Sciences where stations are observed for at least 72 h. A dense GNSS network in Hengill was measured by Iceland Geosurvey (ÍSOR) in 2012, albeit with shorter observation sessions and less frequently. The station velocity estimates derived from data from the continuous stations are superior compared to those that are based on campaign data, because of the higher number of data points. Also, the accuracy of the positions derived from continuous measurements is higher, because position accuracy increases with deployment time, as error sources can be estimated more accurately [*Dzurisin*, 2007] and no changes in antenna height position are introduced. The campaign mode, however, is an important addition that helps increase the spatial density of the GNSS network.

In this study we use data from five continuous and 61 campaign stations (Figure 3). The data were analyzed with the GAMIT software, version 10.6 [*Herring et al.*, 2015]. We include data from continuous GNSS stations in Iceland and over 100 global reference stations to determine the daily solutions in the ITRF08 reference frame [*Altamimi et al.*, 2012]. We then used the GLOBK software, version 5.29 [*Herring et al.*, 2015], to estimate GNSS station positions and velocities in the study area, for the time interval 2012–2015 relative to stable North America (see Figure 3). We observe vertical and horizontal motion on the order of 10–25 mm/yr in the vicinity of the Hellisheidi power plant. The eastward oriented horizontal velocities in the south are mostly caused by spreading across the plate boundary between North America and Eurasia.

2.2. InSAR Data

In addition to the GNSS data set we use satellite-borne synthetic aperture radar (SAR) data, from the TerraSAR-X mission, track 41. We use the ascending (south-to-north orbit) data that the satellite acquires using a right looking configuration. Properties of satellite and orbit for track 41 can be found in Table 1. The SAR acquisitions are processed pairwise using interferometry—SAR interferometry is commonly denoted InSAR—essentially, measuring relative ground displacements (in the line of sight (LOS) of the satellite) through changes in phase between two images. In-depth theory on InSAR methodology can be found in, e.g., *Dzurisin* [2007].

We create interferograms with the DORIS software [*Kampes et al.*, 2003]. To account for topographic contributions we use the 25 m resolution intermediate TanDEM-X digital elevation model. Since we have access to multiple SAR acquisitions from a single track, we use a multitemporal InSAR approach [*Hooper*, 2008], in particular the small-baseline method which is implemented in the StaMPS software [*Hooper et al.*, 2012]. The algorithm uses a set of interferometric pairs (21 in our case) of a given track and identifies pixels that decorrelate little over short time intervals [*Hooper*, 2008]. Those pixels are then used to track the ground deformation over the time range of all acquisitions. StaMPS creates a time series of deformation (Figure 4) for these pixels and estimates an average velocity for the observation time. We use a subset of nine interferograms to estimate LOS velocities for the 2012–2015 time interval. The dates of the images that have been used for these interferograms are given in Table 2. In addition to being able to cover longer time spans, the multitemporal approach has the advantage of minimizing decorrelation noise. The average LOS unit vector for the imaged area is [−0.50 −0.12 0.86] (east, north, up) which implies that the measurements are mainly sensitive to vertical and E-W motion.

We remove the spatially correlated DEM (Digital Elevation Model) error from the interferograms and apply a linear correction to those interferograms we suspect are biased by variations in atmospheric delay [*Bekaert et al.*, 2015a]. The resulting time series plot is shown in Figure 4. Local deformation signals can be observed in the vicinity of both power plants and in the central east of the image. Regionally, we see a NW-SE gradient in deformation across the area, probably related to spreading across the plate boundary (see Figure 4).

Errors in the InSAR data are spatially correlated, which means that we need to find the full variance-covariance matrix to describe the error distribution of the InSAR velocity field v. To this end we follow the procedure of *Bekaert et al.* [2015b]. The method uses the variance of the difference in error between data points depending on their distance, i.e., a semivariogram, which can be extracted from the data set. Once the semivariogram is obtained, we calculate the data error covariance according to the analysis described in Appendix A.

AGU Journal of Geophysical Research: Solid Earth 10.1002/2016JB013626

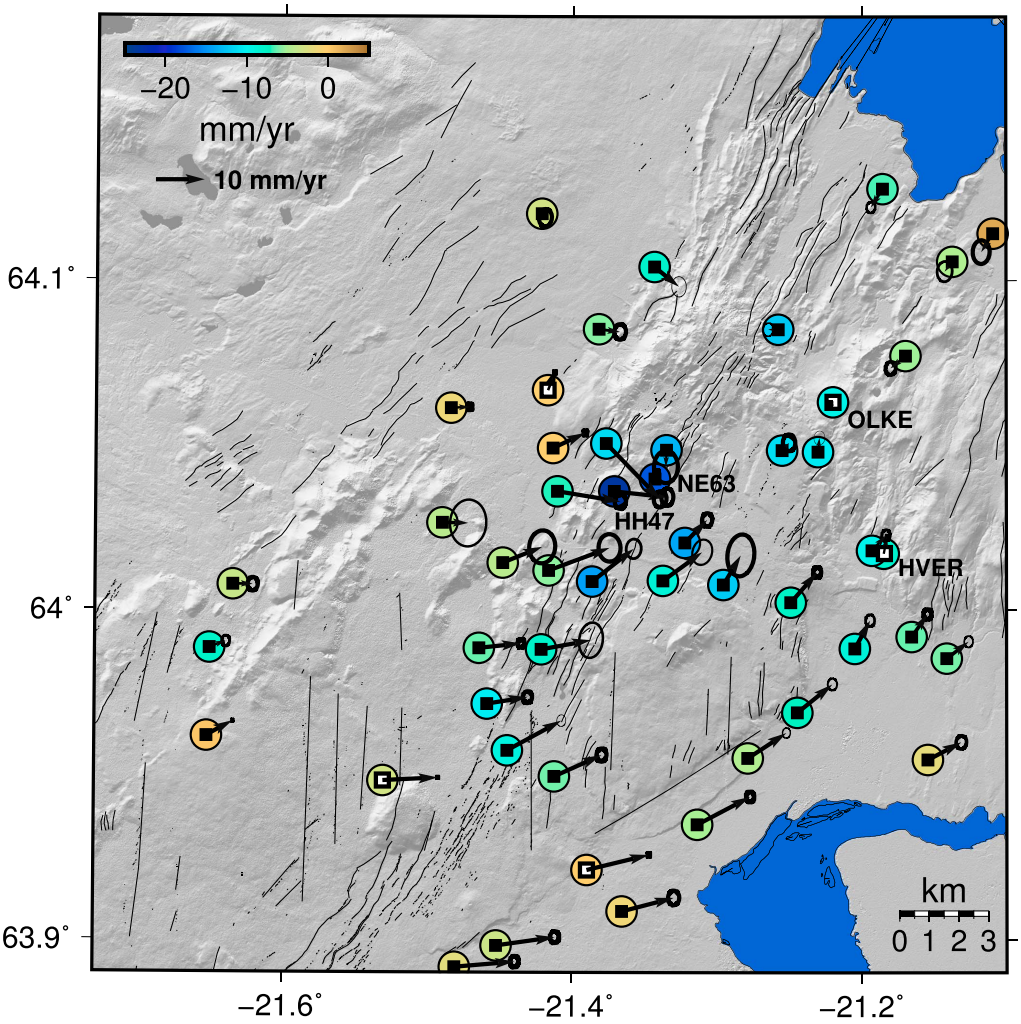

Figure 3. GNSS station velocities 2012–2015 relative to stable North America. Horizontal velocities are shown by arrows, with 95% confidence interval ellipses. Vertical velocities are shown by colored circles. Continuous GNSS stations are shown with white squares. The maximum vertical velocities are at campaign stations HH47 and NE63 with 23 and 18 mm/yr subsidence, respectively.

2.3. Production Data, Pressure, and Temperature Measurements

Reykjavík Energy and ÍSOR monitor pressure and temperature in several boreholes in the production area in Nesjavellir and Hellisheidi. Hellisheidi is the larger plant and had fairly constant production rates between 2012 and 2014 in the range of 40 Mton/yr. It was lower in the years before, however, and has also been reduced again to around 32 Mton/yr in 2015 [*Gunnlaugsson*, 2016b]. At Nesjavellir the production rate has been relatively constant between 2009 and 2015, in a range between 14 and 16 Mton/yr [*Gunnlaugsson*, 2016a].

AGU Journal of Geophysical Research: Solid Earth 10.1002/2016JB013626

Table 1. Configuration of Satellite and Orbit for TerraSAR-X Track 41

TerraSAR-X T41	Configuration
Heading	346°
Look direction	right
Look angle	27.2° – 29.5°
Altitude	515 km
Latitude	64.05°
Wavelength	31 mm (X band)
Resolution	3 m
Covered area	50 km × 30 km

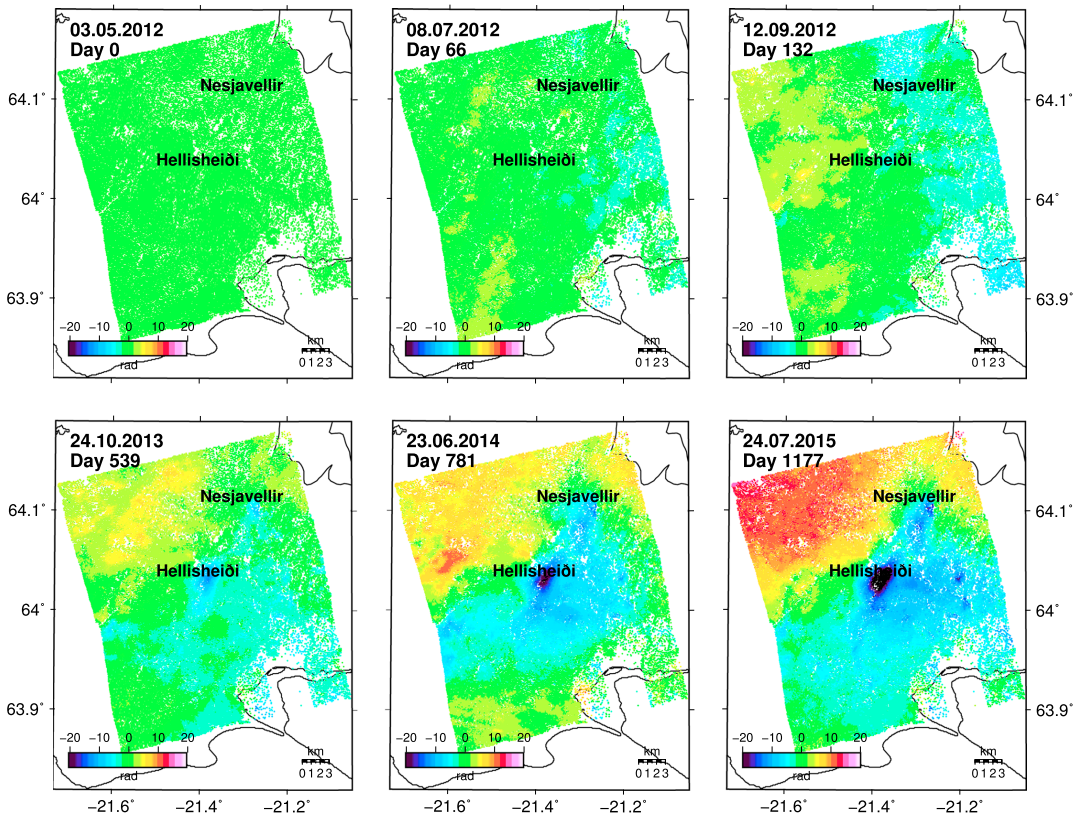

Figure 4. InSAR time series. Line of Sight (LOS) motion as change of phase observed from the satellite between 2012 and 2015. Negative phase values represent motion of the ground away from the satellite, positive values represent motion toward the satellite. Reference value is the mean value of the whole area.

AGU Journal of Geophysical Research: Solid Earth 10.1002/2016JB013626

Table 2. Interferometric Pairs of the SAR Acquisitions Used for Estimating the InSAR Velocity Field[a]

Interferogram	Δt (days)	b_p (m)
5/2012–7/2012	66	11.5
5/2012–9/2012	132	251.8
5/2012–10/2013	539	−82.5
7/2012–9/2012	66	240.3
7/2012–10/2013	473	−94.0
9/2012–10/2013	407	−334.3
10/2013–6/2014	242	176.4
10/2013–7/2015	638	110.0
6/2014–7/2015	396	−66.4

[a]The first column gives the month and year of the interferograms, second column the time interval, and the last column the perpendicular baseline.

Measurements of both pressure and temperature have been conducted in selected boreholes by ÍSOR [*Haraldsdóttir*, 2014; *Tryggvason*, 2014]. Rates of pressure drop seem to be consistently linear and range between 0.2 and 0.3 MPa/yr in the Hellisheidi region and 0.06 and 0.14 MPa/yr around Nesjavellir (Figure 5). The temperature measurements are less consistent. A linear rate of temperature decrease can be observed in, e.g., borehole HE-07 at 1100 m depth with around 3°C/yr. Temperature decrease is only observed in boreholes where the temperature is on the boiling point curve, the cooling being consistent with the pressure drop. This can be explained by absorption of latent heat due to pressure-induced boiling. The area most affected by this is the central part of the Hellisheidi field [*Gunnarsson et al.*, 2011].

3. Inverse Modeling

Our approach to modeling the observed deformation is using elastic half-space models relating subsurface processes to surface deformation. We embed these forward models in a nonlinear inversion framework to find a set of model parameters that can best reproduce the geodetic data. For the geothermal reservoirs we use the pressurized prolate spheroid model derived by *Yang et al.* [1988], which has been applied in comparable scenarios [*Fialko and Simons*, 2000; *Keiding et al.*, 2010]. This model consist of a pressurized body—representing a geothermal reservoir—emplaced in an elastic half-space (the Earth's crust). Pressure changes within the body cause stresses in the crust that result in deformation. For the broad scale deformation that occurs in eastern Hengill we assume a point source [*Mogi*, 1958]. We compare the calculated surface deformation with the observed deformation from our GNSS and InSAR data sets and adjust the source parameters to obtain the best agreement with the data. Following previous studies of deformation in geothermal areas we assume a shear modulus of $\mu = 10$ GPa and a Poisson's ratio of $\nu = 0.25$ [see *Fialko and Simons*, 2000; *Keiding et al.*, 2010].

The high number of InSAR data points ($\sim 10^4$) is impractical for the joint modeling of GNSS and InSAR data since it increases computation time and can create an imbalance in relative weights of the two data sets (the amount of GNSS measurements is on the order of 10^2). Therefore, we subsample the data set based on the variance of pixels with a quadtree algorithm [*Jónsson et al.*, 2002] to obtain a similar number of InSAR data as GNSS data. This method results in an InSAR data set that has a higher resolution in regions of larger displacement gradients and a lower resolution in regions with smaller gradients.

Since this is a nonlinear optimization problem with an infinite number of solutions, we apply a Bayesian optimization scheme. We use the cascading adaptive transitional metropolis in parallel (CATMIP) algorithm developed by *Minson et al.* [2013], a modified form of the Metropolis–Hastings algorithm [*Metropolis et al.*, 1953; *Hastings*, 1970], which is used to sample the posterior probability density function (PDF) of the model parameter space. It uses an annealing procedure similar to simulated annealing optimization [*Kirkpatrick et al.*, 1983]. During the annealing, the algorithm undergoes a succession of "cooling" steps, producing a new, intermediate PDF each time, until it reaches its final "temperature" which yields the optimal solution. At each step the samples from the previous stage are being resampled according to their relative likelihood, and each of

AGU Journal of Geophysical Research: Solid Earth 10.1002/2016JB013626

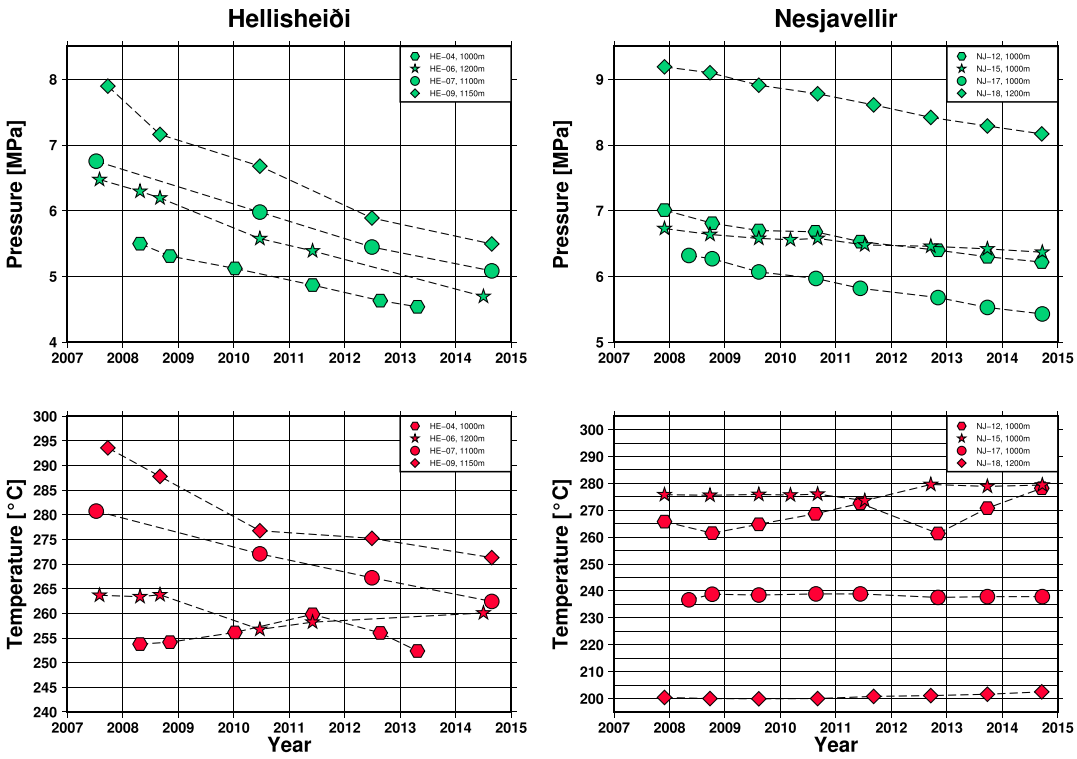

Figure 5. (top row) Pressure changes and (bottom row) temperature changes over time in different boreholes. (left column) Hellisheidi, (right column) Nesjavellir. Measurement depths are given in the legend. Data from Reykjavik Energy [*Gunnlaugsson*, 2016a, 2016b] and ÍSOR [*Haraldsdóttir*, 2014; *Tryggvason*, 2014].

those resamples serves as a seed for a separate Markov chain. This has the effect that more Markov chains are generated in regions of higher probability, which accelerates the algorithm toward the target posterior distribution.

The likelihood function $p(\mathbf{D}|\theta)$ lets us calculate the probability of the observed data $\mathbf{D}$ given a model θ,

$$p(\mathbf{D}|\theta) = \frac{1}{(2\pi)^{N_{dp}/2}|\mathbf{C}|^{\frac{1}{2}}} e^{-\frac{1}{2}\mathbf{r}^T\mathbf{C}^{-1}\mathbf{r}}, \quad (1)$$

where N_{dp} is the number of data points, $\mathbf{C}$ the covariance, and $\mathbf{r}$ the residual between observed and model data points. T is the matrix transpose.

The posterior PDF, $p(\grave{}|\mathbf{D})$, can be obtained following Bayes Theorem, which states that it is proportional to $p(\mathbf{D}|\grave{})$:

$$p(\theta|\mathbf{D}) \propto p(\mathbf{D}|\theta)\, p(\theta), \quad (2)$$

where $p(\grave{})$ is the prior PDF that describes the probability of each value of $\grave{}$. For a detailed description of the algorithm, see *Minson et al.* [2013].

4. Results

We model the observed geodetic data to learn more about the mechanisms that cause the deformation. In the Hengill area this a challenging problem because we observed signals from an interplay of tectonics,

AGU Journal of Geophysical Research: Solid Earth 10.1002/2016JB013626

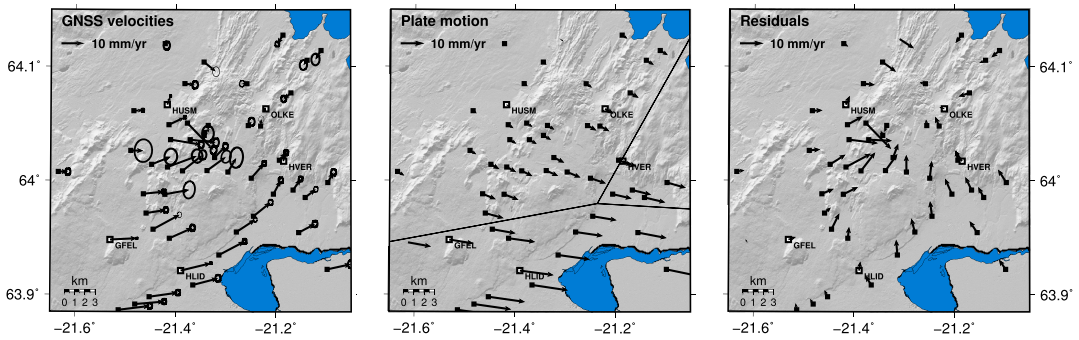

Figure 6. (left) GNSS horizontal velocities 2012–2015, (middle) predicted plate velocities using plate model from *Árnadóttir et al.* [2009] and (right) residual velocities. The velocities are shown relative to stable North America.

magmatism, and man-made deformation in two geothermal fields. The rate of plate spreading across Iceland is around 2 cm/yr and ~1 cm/yr in the study area. That is the same order of magnitude as the rate of subsidence in the vicinity of the power plants, which also causes horizontal motion toward the center of subsidence. The continuous GNSS stations OLKE and HVER as well as several campaign stations south of HVER are subsiding at a rate of up to 1 cm/yr (see Figure 3 and Table S1 in the supporting information), suggesting a wide area of subsidence probably indicating a deep source. Hence, we are aware of at least three different processes that cause deformation of similar magnitudes in the Hengill area. In order to estimate the deformation around the two power plants, we therefore also need to account for the plate spreading and broader scale deformation signal in the area. Our strategy is to first simplify the data set by correcting the horizontal velocities for the plate motion signal. Due to the limited aperture of the data in our study of Hengill and the number of local sources, we are not able to estimate the plate motion signal independently. We therefore choose to use a plate motion model from using the plate motion model from a study of country-wide GNSS motion by *Árnadóttir et al.* [2009]. In the Hengill area, the model consists of the obliquely spreading RP, the spreading WVZ, and the transform-type SISZ (see Figure 1). This allows us to better isolate the local geothermal signals as well as the broader signal in eastern Hengill, see Figures 6 and 7.

After substracting the plate motion from the InSAR data, the local deformation signals around the power plants become more distinct and the long wavelength NW–SE gradient is reduced (Figure 7). In the GNSS data,

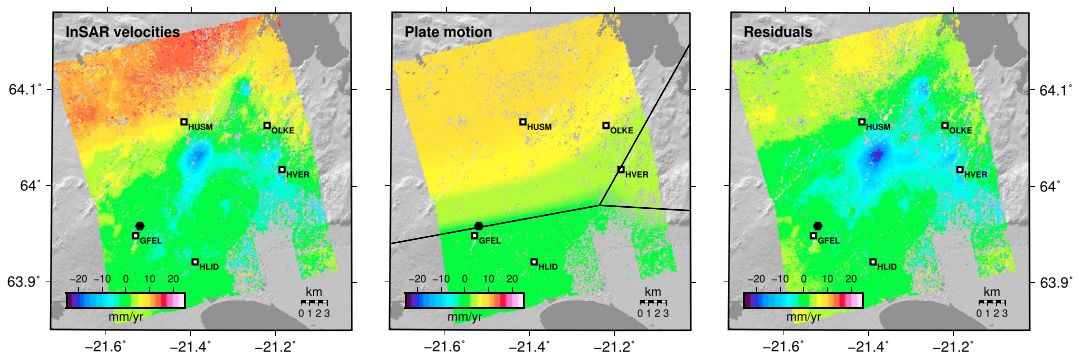

Figure 7. (left) InSAR mean velocity field for the 2012–2015 time interval derived from the time series shown in Figure 4, (middle) predicted plate velocity using plate model from *Árnadóttir et al.* [2009] and (right) residual velocities. The plate boundaries are plotted as black lines. All velocities are in LOS direction, positive toward the satellite, negative away from it. The black hexagon shows the location of the reference point of the velocities (v_{los} = 0).

AGU Journal of Geophysical Research: Solid Earth 10.1002/2016JB013626

Table 3. Estimated Parameters of the Deformation Sources and Their 90% Confidence Intervals (CI)[a]

Hellisheidi	Joint	90% CI	InSAR	90% CI	GNSS	90% CI
Hellisheidi						
Longitude (°W)	21.371	(21.365; 21.378)	21.376	(21.358; 21.389)	21.369	(21.358; 21.382)
Latitude (°N)	64.033	(64.030; 64.036)	64.032	(64.023; 64.038)	64.030	(64.020; 64.037)
Depth (km)	0.6	(0.3; 0.9)	0.7	(0.3; 2.5)	0.6	(0.2; 1.4)
Semimajor axis (km)	2.6	(1.9; 3.4)	2.5	(1.7; 5.4)	3.7	(2.3; 6.3)
Semiminor axis (km)	1.2	(1.0; 1.5)	1.1	(0.7; 1.5)	1.0	(0.7; 1.3)
Strike (deg)	46	(25; 68)	48	(16; 76)	31	(13; 60)
Nesjavellir						
Longitude (°W)	21.267	(21.254; 21.284)	21.274	(21.259; 21.288)	21.275	(21.255; 21.294)
Latitude (°N)	64.107	(64.092; 64.127)	64.097	(64.075; 64.122)	64.099	(64.077; 64.128)
Depth (km)	1.0	(0.1; 2.3)	0.8	(0.2; 1.9)	1.0	(0.1; 2.1)
Semimajor axis (km)	3.8	(1.9; 6.4)	3.7	(1.8; 6.3)	3.8	(1.9; 6.1)
Semiminor axis (km)	1.0	(0.4; 1.5)	0.8	(0.2; 1.3)	0.5	(0.1; 1.3)
Strike (deg)	22	(2; 66)	16	(2; 60)	33	(5; 80)
Eastern Hengill						
Longitude (°W)	21.247	(21.230; 21.267)	21.261	(21.129; 21.383)	21.251	(21.226; 21.274)
Latitude (°N)	64.057	(64.048; 64.066)	64.034	(64.004; 64.097)	64.060	(64.049; 64.070)
Depth (km)	6.9	(5.9; 8.1)	16.9	(11.9; 19.6)	7.2	(5.9; 8.5)
ΔV (10^6 m^3/yr)	−2.4	(-1.8; -3.1)	−16.1	(−1.8; −31.0)	−2.5	(−1.6; −3.4)

[a]The depths of the spheroidal sources at Hellisheidi and Nesjavellir are to the top of the body, the depth of the point source in eastern Hengill is to the center. The coordinates represent the center of the respective sources. The semimajor axis is half the long axis of the spheroid, orientated along its strike direction which is measured from the north. The semiminor axes are half the short axes of the spheroid, i.e., the vertical axis and the axis that is perpendicular to the strike. Pressure change is fixed at −0.25 MPa/yr (Hellisheidi) and −0.1 MPa/yr (Nesjavellir). We assume a shear modulus of $\mu = 10$ GPa and a Poisson's ratio of $\nu = 0.25$.

the horizontal velocities point toward Hengill (Figure 6), indicating a deep source in addition to the shallow geothermal sources.

Using only two geothermal sources, we obtain results that do not agree with the actual locations of the geothermal fields, because the nonlinear optimization tries to reduce residuals of the broad scale signal in eastern Hengill. By adding an unconstrained point source [*Mogi*, 1958] to the solution space, we obtain more

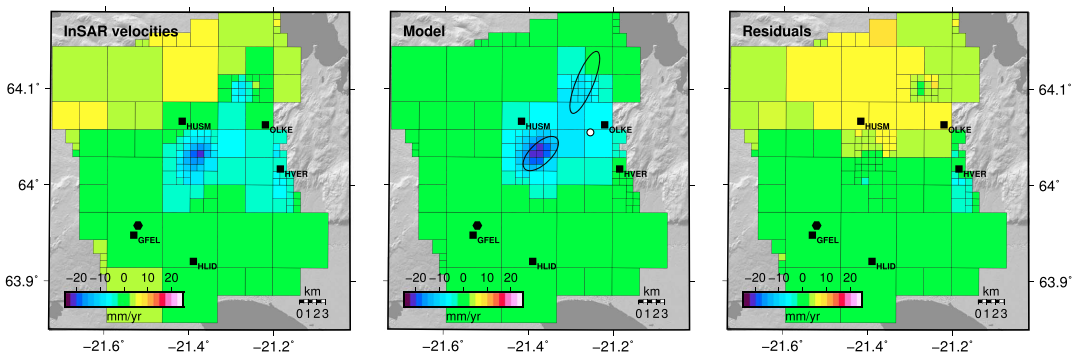

Figure 8. (left) Subsampled InSAR velocities 2012–2015 corrected for plate motion, (middle) estimated velocities, and (right) residuals. All in LOS of the satellite. The velocity reference point is denoted by a black hexagon. Black ellipses show surface projections of the spheroidal source locations, the white circle marks the point source.

AGU Journal of Geophysical Research: Solid Earth 10.1002/2016JB013626

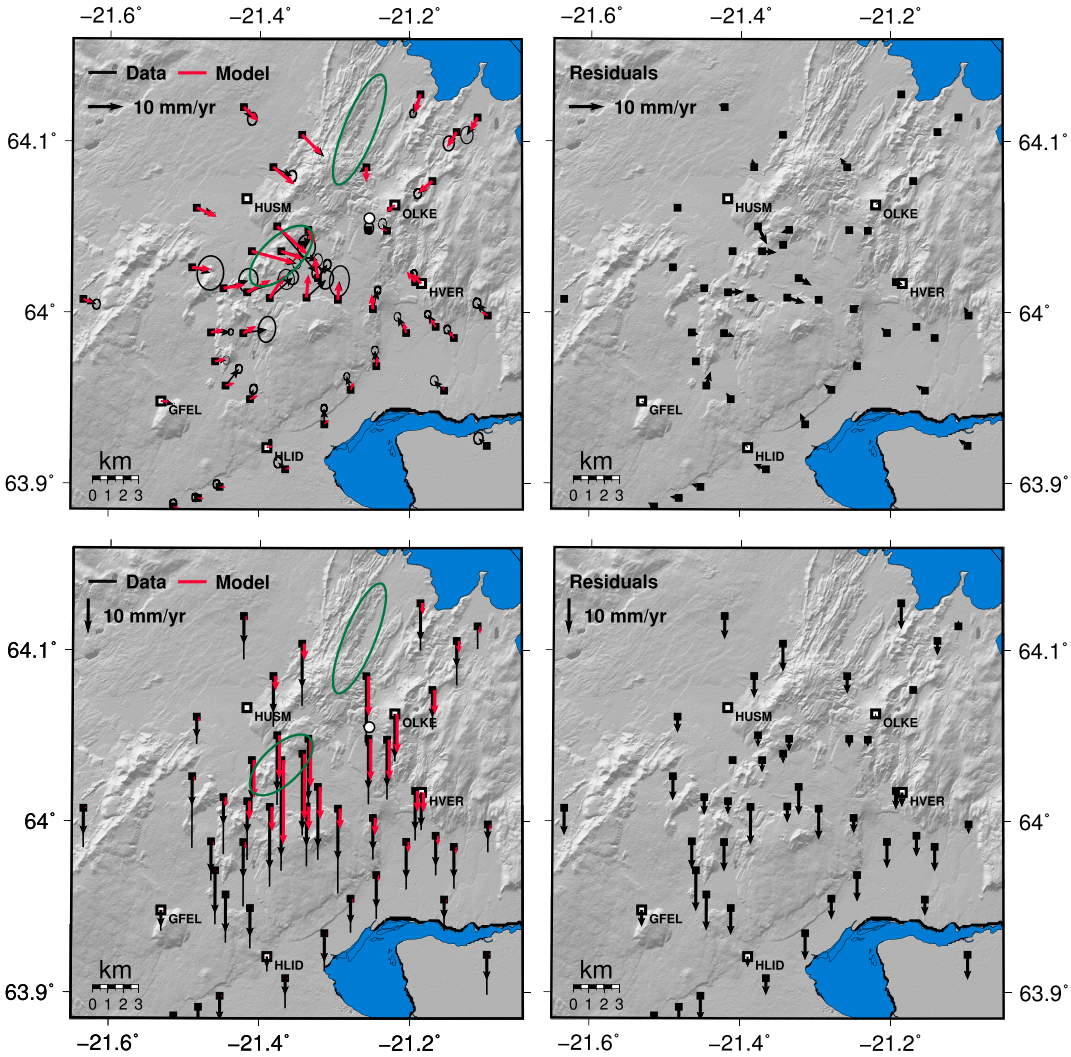

Figure 9. Observed GNSS station velocities after correcting for plate motion (black arrows) and estimated station velocities (red arrows) for the 2012–2015 time interval. (top row) Horizontal deformation corrected for plate motion using the ISNET model [*Árnadóttir et al.*, 2009]. (bottom row) Vertical deformation. Plots on the left-hand side show observed motion with black arrows and 95% confidence intervals and model predictions with red arrows. The plots on the right show residuals. All velocities are referenced to the continuous GNSS station SELF (see Figure 1). Dark green ellipsoids are geothermal source locations, the white circle depicts the deep point contraction source.

AGU Journal of Geophysical Research: Solid Earth 10.1002/2016JB013626

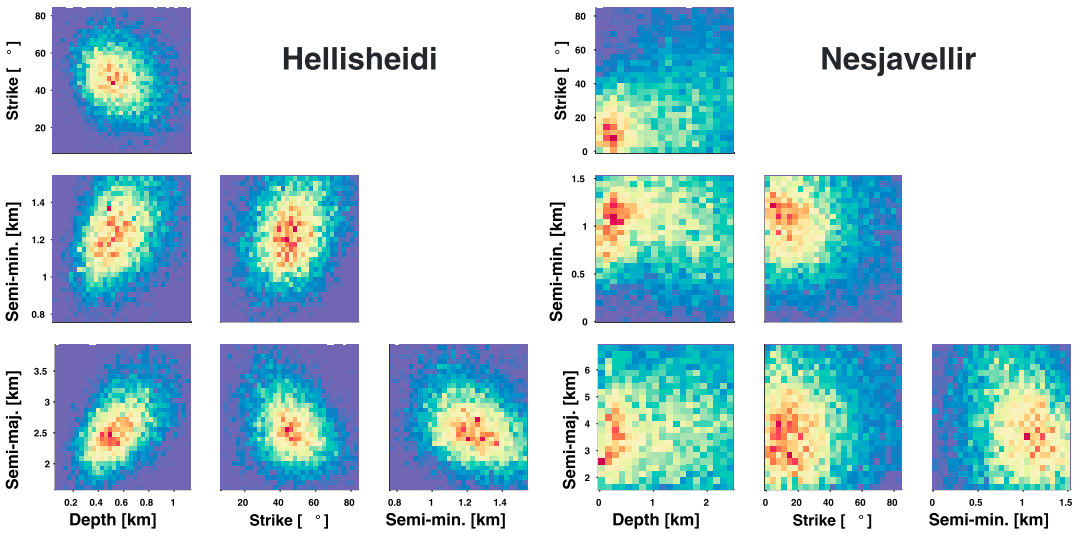

Figure 10. Posterior probability distribution for the model parameters of the spheroidal geothermal reservoirs. Depth is to the top of the reservoir. The coordinates represent the center of the respective sources. The semimajor axis is half the long axis of the spheroid, orientated along its strike direction which is measured from north. The semiminor axes are half the short axes of the spheroid, i.e., the vertical axis and the axis that is perpendicular to the strike. Pressure change is fixed at −0.25 MPa/yr (Hellisheidi) and −0.1 MPa/yr (Nesjavellir).

reasonable solutions for the geothermal sources and an additional deep source in eastern Hengill. For this source we obtain parameters (and 90% confidence intervals) of $6.9^{+1.2}_{-1.0}$ km depth and $2.4^{+0.7}_{-0.6}$ million m^3/yr volume decrease at the coordinates 64.057 ± 0.009°N and $21.253^{+0.020}_{-0.017}$°W (see Table 3). The location of this source falls into the area between the three central volcanoes of Hengill, Hrómundartindur, Hengill, and Grensdalur [*Feigl et al.*, 2000]. In this area both the InSAR data (see Figures 4 and 8) as well as the GNSS stations show significant displacement (subsidence rates of around 10 mm/yr at OLKE, HVER, and neighboring stations; see Figures 3 and 9). Our result is about ∼3 km NW of the magmatic intrusion suggested by *Feigl et al.* [2000] for the 1994–1998 uplift episode (which was 21.213°W/64.032°N/7.0 km depth). The proximity of the source locations suggests that the sources for the inflation and deflation are most likely related.

For the local signals around the geothermal power plants we use two spheroid-shaped pressure sources [*Yang et al.*, 1988]. We fix the pressure change at Hellisheidi to −0.25 MPa/yr which is the average rate of measured pressure decrease in the reservoir (see section 2.3). We find a shallow source of deformation (1.8 ± 0.4 km depth) below Hellisheidi with a volume of around 16 km^3 (Table 3). This translates to a decrease in reservoir volume ΔV of $4 \cdot 10^5$ m^3/yr using the relation given by *Eshelby* [1957]:

$$\Delta V = V \Delta P / \mu \,, \tag{3}$$

where V is the total reservoir volume, ΔP the change in pressure, and μ the shear modulus.

At Nesjavellir we fix the pressure change to −0.1 MPa/yr and find a reservoir with a depth of $2.0^{+1.4}_{-1.1}$ km and volume of around 17 km^3. The rate of volume decrease is approximately $2 \cdot 10^5$ m^3/yr. The source parameters are less well constrained than at Hellisheidi (Figure 10) due to fewer GNSS stations and low signal-to-noise ratio, compared to Hellisheidi.

It should be noted that the obtained volumes depend on the pressure change that is assumed for each reservoir. Considering the range of observed rates of pressure decay (see section 2.3), the reservoir volume at Hellisheidi may be as large as 17 km^3 (for a pressure change of −0.2 MPa/yr) or as low as 14 km^3 ($\Delta P = -0.3$ MPa/yr). At Nesjavellir the volume may range from 16 km^3 ($\Delta P = -0.14$ MPa/yr) to 18 km^3 ($\Delta P = -0.06$ MPa/yr). However, the uncertainties we obtain for the source dimensions (see Table 3) indicate even larger ranges for the total reservoir volumes.

AGU Journal of Geophysical Research: Solid Earth 10.1002/2016JB013626

The two spheroidal sources yield results that agree with the geodetic data within residuals of 5 mm/yr in the areas around the power plants. These models reproduce the regions of highest deformation in the InSAR data set (up to 26 mm/yr LOS velocity around the Hellisheidi power plant), as well as the largest GNSS velocities (Figure 3). At Hellisheidi, the model captures the maximum magnitude of the subsidence signal with residuals below 5 mm/yr and has a similarly SW-NE elongated shape. In the northeastern part of Hellisheidi field, however, the deformation is overestimated in the model when compared to the InSAR data (Figure 8). Around Nesjavellir the model has significant misfits, which can be seen in the InSAR data (Figure 8) and the vertical GNSS velocities of the stations further east of Nesjavellir (Figure 9). It may be that the Nesjavellir source is being overpredicted in order to accomodate the horizontal GNSS velocities.

The geothermal source models we obtain are shallow, which is consistent with the production depths in Hengill. Studies of other geothermal areas find similar source depths, e.g., depth ranges from 1 to 3 km for spheroidal sources in the Coso area in California [*Fialko and Simons*, 2000].

5. Discussion

Crustal deformation due to geothermal power production is mainly caused by contraction or expansion of the rock matrix in the reservoirs. It can be driven by changes in temperature as well as pressure, which may be in a feedback relation to each other. In order to keep the modeling simple, we first examine the effect of pressure change in our simulations and then use the results to evaluate whether this was a reasonable choice. We justify our choice with the fact that changes in pressure have been observed consistently throughout both reservoirs whereas temperature changes occur only in a few boreholes (see Figure 5). We use the measured reservoir pressure changes as a fixed parameter in our models and show that they can explain the deformation at Hellisheidi. This indicates that pressure changes are likely to be a key factor in the deformation.

5.1. Comparing Modeled Volume Changes to Extraction Rates

Pressure change can be translated into a change of reservoir volume, see equation (3). Other deformation studies have compared this model-estimated change of reservoir volume to volumetric fluid extraction rates, estimated from mass extraction rates given by the power plant operator [e.g., *Eysteinsson*, 2000; *Keiding et al.*, 2010; *Drouin*, 2016; *Barbour et al.*, 2016]. They often find discrepancy between estimated and observed volume change of more than 1 order of magnitude. This is not surprising since this approach is overly simplistic, mainly for two reasons: first, in a high-temperature geothermal field, the ratio of water to steam within the reservoir is not known. Thus, there is a large uncertainty when converting mass flow to volume flow. Second (and more importantly), the extracted fluid volume does not equal the total volume change of the reservoir. Instead, if we want to compare the change in rock volume to known production rates, we have to consider how they are related. For a reservoir with a volume V, the mass of produced fluid Δm can be related to the change in reservoir pressure ΔP through the *storativity* s of the rock, i.e., following *Axelsson* [2012]: $\Delta m = sV\Delta P$. Using equation (3) we can introduce the change in reservoir volume ΔV into this equation and find an expression that relates the mass extraction rate to the estimated ΔV (for spheroidal reservoirs)

$$\Delta m = s\mu\Delta V, \tag{4}$$

where μ is the shear modulus. Thus, in order to compare reservoir volume change to extraction rates, ideally, we should know the storativity. Since the storativity is not known in this case, we can only make a circular argument by solving for the value of s and then decide whether it is a reasonable value or not. To do this, we have to take into account that the mass extraction is balanced by natural recharge. According to reservoir models, we assume a total recharge rate for both Hellisheidi and Nesjavellir of 50% and then obtain a storativity of around $5 \cdot 10^{-6}$ kg m^{-3} Pa^{-1} for Hellisheidi (with $\Delta m = 18$ Mton/yr, $\Delta V = 4 \cdot 10^5$ m^3/yr and $\mu = 10$ GPa) and $4 \cdot 10^{-6}$ kg m^{-3} Pa^{-1} for Nesjavellir (with $\Delta m = 8$ Mton/yr, $\Delta V = 2 \cdot 10^5$ m^3/yr, and $\mu = 10$ GPa). These estimates of storativity are within the range of liquid-dominated reservoirs ($0.1 - 10 \cdot 10^{-6}$ kg m^{-3} Pa^{-1}, see Table 3 in *Axelsson* [2012]).

5.2. Impact of Thermal Contraction

Thermal contraction of the rock matrix might be another important contribution to the total deformation. We can use the observed rates of temperature drop to approximate the magnitude of deformation that we could expect from thermal contraction of the rock matrix. Observed temperature changes at the Hellisheidi power plant indicate a decrease of up to 3°C/yr in several boreholes, while others show no change (see Figure 5).

AGU Journal of Geophysical Research: Solid Earth 10.1002/2016JB013626

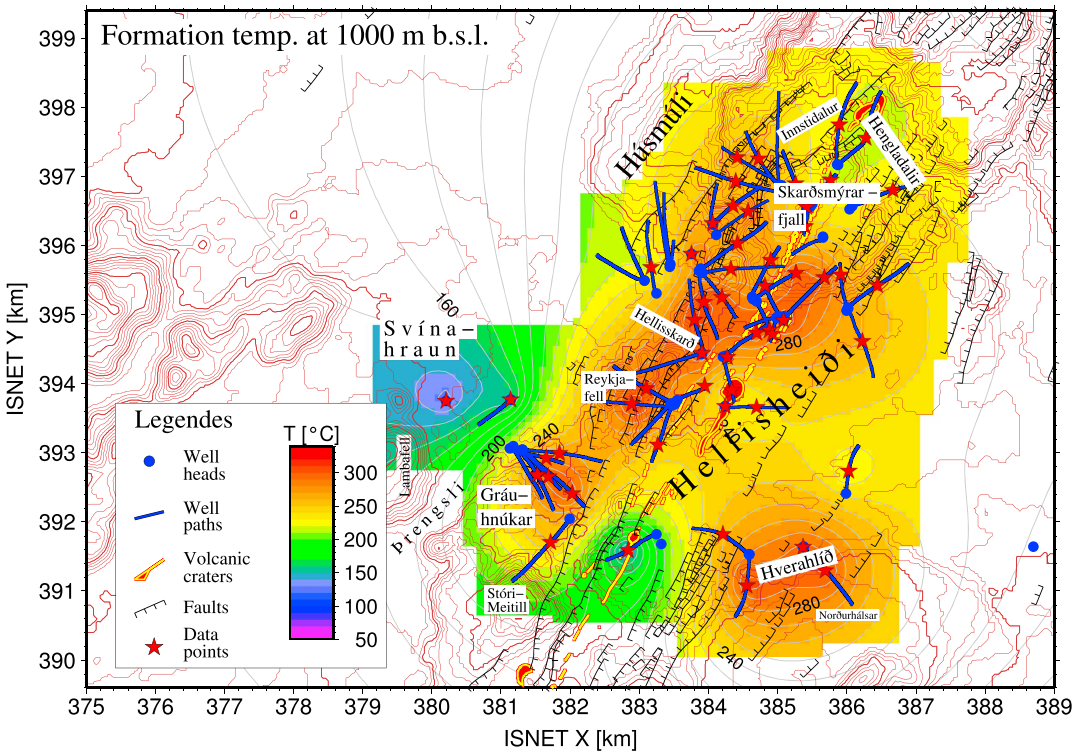

Figure 11. Temperature distribution, boreholes (blue dots and lines), and data points (red stars) in the Hellisheidi reservoir at 1000 m depth.

We assume that temperature is reduced mainly due to latent heat effects of boiling caused by dropping pressure, and this appears only in the part of the reservoir that has a combination of high temperatures and low pressures. These conditions can be found in the uppermost part of the central region of the reservoir (see Figure 11). We approximate the size of the area to 1.5 km^2 with a thickness of around 300 m. We use the thermal expansion relation $\Delta V_{th} = \alpha V \Delta T$ [*Turcotte and Schubert*, 2002]—where ΔT, V, and α are the temperature change, volume, and thermal expansion coefficient of the rock, respectively—to estimate the volume change due to thermal contraction, ΔV_{th}. Assuming a coefficient of thermal expansion (for a rock with basalt-like composition) of $\alpha = 2 \cdot 10^{-5}$°/C [*Robertson*, 1988] and a rock volume of 0.5 m^3 (see above), we obtain a contraction of about $3 \cdot 10^4$ m^3/yr. That is less than 10% of the volume change that we estimate for the spheroidal source at Hellisheidi (see section 4). This indicates that for this area, the deformation caused by temperature changes is probably minor when compared to deformation caused by changes in pressure.

5.3. Nature of the Deep Source in Eastern Hengill

We want to test if the subsidence observed in the eastern part of Hengill may be related to the intrusion that *Feigl et al.* [2000] inferred for the time interval 1994–1998. The total volume of injected magma inferred by *Feigl et al.* [2000] amounts to ~40 million m^3. If the whole volume would solidify after the intrusion, it would cause a subsequent volume decrease of 4 million m^3, assuming a density ratio between liquid and solid magma of 0.9 [*Caricchi et al.*, 2014]. Our modeling results (Table 3) imply a volume loss of 7 million m^3 over the time interval 2012–2015, which is larger than the estimate of the contraction of the intrusion due to solidification by a factor of around 2. The difference is likely to be even larger since there is probably contraction before and after the 2012–2015 time interval. The mismatch both in volumes and in source locations

AGU Journal of Geophysical Research: Solid Earth 10.1002/2016JB013626

(see section 4) could suggest that interpreting the inflation and deflation as solely caused by a magmatic intrusion and the cooling thereof might be—at least partly—incorrect. Other studies have shown that inflation in volcanic areas can be explained by natural hydrothermal fluid injection and gas formation [*Hurwitz et al.*, 2007; *Hutnak et al.*, 2009]. These processes yield a volume increase that is more reversible than one caused by magma injection alone, and thus may better explain the magnitude of deflation that we estimate. A distinct location for pore pressure-driven deformation would also be harder to constrain because of the mobility of the fluids, which might further explain the difference in modeled locations between inflation and deflation episodes. Furthermore, *Tryggvason et al.* [2002] conducted a seismic tomography study (using seismic data from 1973 to 1999) and found a low-velocity anomaly below Hengill, which they intepreted as evidence for the presence of supercritical fluids at depth. If close to the critical point, these fluids could have been the explanation for the inflation.

6. Conclusion

We obtain the surface deformation field in the Hengill region from 2012 to 2015 from both GNSS and SAR observations and correct the data for plate motion using the results from *Árnadóttir et al.* [2009]. We perform a joint inversion on the residual velocities using models of pressurized spheroids and spheres in an elastic half-space. The inversion shows that the remaining data can be reproduced by three deformation sources. We find two shallow spheroidal sources representing contracting geothermal reservoirs in the Hellisheidi and Nesjavellir production fields. We also estimate a deep contracting source below eastern Hengill in the vicinity of the 1994–1998 inflation source [*Feigl et al.*, 2000]. The results show how complex deformation signals can be in Iceland, where tectonic, magmatic, and anthropogenic deformation can overlap, and how important it is to take all these processes into account.

The eastern Hengill deformation source has a depth of $6.9^{+1.2}_{-1.0}$ km and a volume loss of around 2 million m^3/yr. We can not conclusively link it to the intrusion suggested by *Feigl et al.* [2000]. To better understand this signal, the whole deformation history since the end of the uplift episode should be considered. It may also be worthwhile to revisit the deformation data for the intrusive episode and investigate if it may be explained by processes other than magma intrusion, e.g., natural hydrothermal fluid injection, gas formation, or thermal expansion.

The Hellisheidi geothermal source model we estimate extends from about 0.6 to 3.0 km depth and is orientated roughly along the regional fissure swarm. The Nesjavellir source extends from about 1.0 to 3.0 km depth. This source is less well constrained than the Hellisheidi source, due to a lower GNSS station density and a weaker deformation signal.

Using the observed pressure change in the geothermal fields, we are able to reproduce the subsidence signal at the surface. Therefore, we argue that it is likely that the pressure decrease is responsible for most of the deformation observed in the geothermal areas.

Appendix A: The Variance-Covariance Matrix of the InSAR Data Set

For obtaining the variance-covariance matrix of the InSAR data we follow the procedure by *Bekaert et al.* [2015b]. We start with the variance of the difference of two correlated variables, which is given by

$$\sigma^2_{\mathrm{pq}} = \sigma^2_p + \sigma^2_q - 2\,C_{\mathrm{pq}}\,, \tag{A1}$$

where σ^2_{pq} is the difference in variances between any random pair of points, p and q, in the InSAR image, σ^2_{p} is the variance of point p, and C_{pq} is the covariance of points p and q, which is what we are interested in.

Now, if we assume all points by themselves have the same variance ($\sigma^2_p = \sigma^2_q$), equation (A1) reduces to that of a semivariogram,

$$\gamma_{\mathrm{pq}}(x) = \sigma^2_0 - C_{\mathrm{pq}}(x)\,, \tag{A2}$$

where x is the distance between points p and q, σ^2_0 is the variance at each point, and

$$\gamma_{\mathrm{pq}} = \frac{1}{2}\sigma^2_{\mathrm{pq}}\,. \tag{A3}$$

AGU Journal of Geophysical Research: Solid Earth 10.1002/2016JB013626

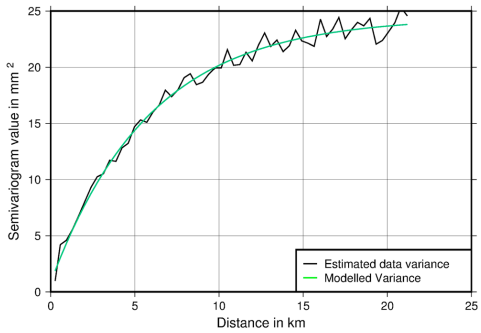

Figure A1. Semivariogram value over the distance between points. The model (green line) is calculated from equation (A6). $\sigma^2_{\text{bin}} = 23.6\ \text{mm}^2$, $N = 0.8\ \text{mm}^2$, $R = 17.5$ km.

Acknowledgments
The authors would like to thank Einar Gunnlaugsson from Reykjavik Energy (RE) for providing production data from Hellisheidi and Nesjavellir; Bjarni Reyr Kristjánsson (RE) for discussions and advice regarding the geothermal power plant operations; RE and ÍSOR for GNSS data from the dense Hengill network; the Icelandic Meteorological Office (IMO) for operating the cGPS network in Iceland; Sigrún Hreinsdóttir (GNS, New Zealand) for global GNSS solutions; Tabrez Ali (University of Wisconsin, Madison, USA) for help and ideas regarding deformation in geothermal areas; Halldór Geirsson (IES) for helpful comments on the work in progress; Sarah Minson (U.S. Geological Survey) for help with CATMIP and letting us use her code; David Bekaert (University of Leeds, UK) for helpful advice on the InSAR processing; Sigurjón Jónsson (King Abdullah University of Science and Technology, KSA) for providing his Quadtree code; Guðni Axelsson (ÍSOR) for helpful discussions concerning geothermal reservoirs; the crustal deformation group at IES for help with the GNSS measurements in SW Iceland and discussions on the work in progress. For computing the elastic half-space models we use *DMODELS* [*Battaglia et al.*, 2013]. Many of the figures were prepared using the GMT software [*Wessel and Smith*, 1991; *Wessel et al.*, 2013]. The earthquake locations in Figure 2 were provided by IMO. The intermediate TanDEM-X digital elevation model used in the InSAR processing was provided by DLR under project IDEM_GEOL0123. COMET is the NERC Centre for the Observation and Modelling of Earthquakes, Volcanoes and Tectonics. This work was supported in part by grants from the Iceland Research Fund and the University of Iceland Research Fund. The data for this paper are available by contacting the corresponding author at daj22@hi.is.

We use a bootstrapping approach [see, e.g., *Efron and Tibshirani*, 1986] to calculate the right-hand side of equation (A3). To this end, we first compute the best estimate of the velocity field, $\hat{v}$, from the interferograms using weighted least squares based on the covariance between each of them. Then, we calculate n realizations of the velocity field v_{boot} by resampling from the set of interferograms. We can calculate the residuals between v_{boot} and $\hat{v}$ as,

$$r^k = v^k_{\text{boot}} - \hat{v}\,, \tag{A4}$$

where k represents one of the n bootstrap realizations.

Now, we can use the residuals to estimate the variance, σ^2_{pq}, between pairs of points,

$$\sigma^2_{\text{pq}} = \sum_k^n \frac{\left(r^k_{\text{pq}}\right)^2}{n-1}\,, \tag{A5}$$

where r^k_{pq} is the difference in r^k between a random pair of points p and q ($r^k_{\text{p}} - r^k_{\text{q}}$).

Binning σ^2_{pq} depending on distance between points yields the semivariogram which we can describe with a Gaussian semivariogram model,

$$\gamma_m(x) = N + \sigma_0^2\,(1 - \text{e}^{-3\frac{x}{R}})\,, \tag{A6}$$

where N is often called nugget term, representing variations on small spatial scale, R is the range, i.e., the distance limit after which data is no longer correlated and the variance σ_0^2 is also known as the sill. Using the binned variances, we can estimate N, σ_0^2 and R, plug σ_0^2 and γ into equation (A2) and solve it for C_{pq}. Then we can calculate the variance-covariance matrix of our data as follows:

$$C_{\text{pq}}(x) = \sigma^2_{\text{bin}} \cdot e^{-3\frac{x}{R}} - N\,, \tag{A7}$$

Using the estimated semivariogram of our data (see Figure A1), we use the model of equation (A2) and invert for the values of N, σ_0^2, and R: $\sigma^2_{\text{bin}} = 23.6\ \text{mm}^2$, $N = 0.8\ \text{mm}^2$, $R = 17.5$ km. From here we calculate the variance-covariance matrix of our data using equation (A7). These estimates give a standard deviation of the InSAR data of 4.9 mm/yr.

References

Ali, S., et al. (2016), Time-series analysis of surface deformation at Brady Hot Springs geothermal field (Nevada) using interferometric synthetic aperture radar, *Geothermics*, *61*, 114–120.
Allis, R., and X. Zhan (2000), Predicting subsidence at Wairakei and Ohaaki geothermal fields, New Zealand, *Geothermics*, *29*, 479–497.
Altamimi, Z., I. Metivier, and X. Collilieux (2012), ITRF2008 plate motion model, *J. Geophys. Res.*, *117*, B07402, doi:10.1029/2011JB008930.
Árnadóttir, T., S. Hreinsdóttir, G. Gudmundsson, P. Einarsson, M. Heinert, and C. Völksen (2001), Crustal deformation measured by GPS in the South Iceland Seismic Zone due to two large earthquakes in June 2000, *Geophys. Res. Lett.*, *28*(21), 4031–4033.
Árnadóttir, T., B. Lund, W. Jiang, H. Geirsson, H. Björnsson, P. Einarsson, and T. Sigurdsson (2009), Glacial rebound and plate spreading: Results from the first countrywide GPS observations in Iceland, *Geophys. J. Int.*, *177*, 691–716.

AGU Journal of Geophysical Research: Solid Earth 10.1002/2016JB013626

Axelsson, G. (2012), The physics of geothermal energy, in *Comprehensive Renewable Energy*, edited by A. Sayigh, pp. 3–50, Elsevier, Oxford, U. K.
Barbour, A. J., E. L. Evans, S. H. Hickman, and M. Eneva (2016), Subsidence rates at the southern Salton Sea consistent with reservoir depletion, *J. Geophys. Res. Solid Earth*, *121*, 5308–5327, doi:10.1002/2016JB012903.
Battaglia, M., P. Cervelli, and J. Murray (2013), Modeling crustal deformation near active faults and volcanic centers—A catalog of deformation models, U.S. Geol. Surv. Tech. and Meth. 13-B1, 96 p., USGS, Reston, Va.
Bekaert, D., R. Walters, T. Wright, A. Hooper, and D. Parker (2015a), Statistical comparison of InSAR tropospheric correction techniques, *Remote Sens. Environ.*, *170*, 40–47.
Bekaert, D., A. Hooper, and T. Wright (2015b), Reassessing the 2006 Guerrero slow-slip event, Mexico: Implications for large earthquakes in the Guerrero Gap, *J. Geophys. Res. Solid Earth*, *120*, 1357–1375, doi:10.1002/2014JB011557.
Caricchi, L., J. Biggs, C. Annen, and S. Ebmeier (2014), The influence of cooling, crystallisation and re-melting on the interpretation of geodetic signals in volcanic systems, *Earth Planet. Sci. Lett.*, *388*, 166–174.
Chi, S., and R. Reilinger (1984), Geodetic evidence for subsidence due to groundwater withdrawal in many parts of the United States of America, *J. Hydrol.*, *67*(1), 155–182.
Clifton, A., F. Sigmundsson, K. Feigl, G. Guðmundsson, and T. Árnadóttir (2002), Surface effects of faulting and deformation resulting from magma accumulation at the Hengill triple junction, SW Iceland, 1994–1998, *J. Volcanol. Geotherm. Res.*, *115*, 233–255.
Decriem, J., et al. (2010), The 2008 May 29 earthquake doublet in SW Iceland, *Geophys. J. Int.*, *181*, 1128–1146.
DeMets, C., R. G. Gordon, and D. F. Argus (2010), Geologically current plate motions, *Geophys. J. Int.*, *181*(1), 1–80.
Drouin, V. (2016), Constraints on deformation processes in Iceland from space geodesy: Seasonal load variations, plate spreading, volcanoes and geothermal fields, PhD thesis, Faculty of Earth Sci., Univ. of Iceland, Reykjavik, Iceland.
Dzurisin, D. (2007), *Volcano Deformation*, Springer, Berlin.
Efron, B., and R. Tibshirani (1986), Bootstrap methods for standard errors, confidence intervals, and other measures of statistical accuracy, *Stat. Sci.*, *1*(1), 54–75.
Einarsson, P. (1991), Earthquakes and present-day tectonism in Iceland, *Tectonophysics*, *189*(1), 261–279.
Einarsson, P. (2008), Plate boundaries, rifts and transforms in Iceland, *Jokull*, *58*(12), 35–58.
Eshelby, J. D. (1957), The determination of the elastic field of an ellipsoidal inclusion, and related problems, *Proc. R. Soc. A*, *241*, 376–396, The Royal Society.
Eysteinsson, H. (2000), Elevation and gravity changes at geothermal fields on the Reykjanes Peninsula, SW Iceland, paper presented at 2000 World Geothermal Congress, pp. 559–564, Kyushu-Tohoku, Japan, 28 May–10 Jun.
Feigl, K. L., J. Gasperi, F. Sigmundsson, and A. Rigo (2000), Crustal deformation near Hengill volcano, Iceland 1993–1998: Coupling between magmatic activity and faulting inferred from elastic modeling of satellite radar interferograms, *J. Geophys. Res.*, *105*(25), 655–25.
Fialko, Y., and M. Simons (2000), Deformation and seismicity in the Coso geothermal area, Inyo County, California: Observations and modeling using satellite radar interferometry, *J. Geophys. Res.*, *105*, 21,781–21,793.
Fielding, E., R. Blom, and R. Goldstein (1998), Rapid subsidence over oil fields measured by SAR interferometry, *Geophys. Res. Lett.*, *25*, 3215–3218.
Franzson, H., E. Gunnlaugsson, K. Árnason, K. Sæmundsson, B. Steingrímsson, and B. Harðarson (2010), The Hengill geothermal system, conceptual model and thermal evolution, paper presented at 2010 World Geothermal Congress, Bali, Indonesia, 25–29 Apr.
Geirsson, H., et al. (2010), Overview of results from continuous GPS observations in Iceland from 1995 to 2010, *Jokull*, *60*, 3–22.
Gunnarsson, G., A. Arnaldsson, and A. Oddsdóttir (2011), Model simulations of the Hengill Area, southwestern Iceland, *Transp. Porous Media*, *90*, 3–22.
Gunnlaugsson, E. (2016a), Nesjavellir–vinnsluskýrsla 2015, *Tech. Rep.*, Orkuveita Reykjavíkur (Reykjavik Energy), Reykjavik, Iceland.
Gunnlaugsson, E. (2016b), Hellisheiði–vinnsluskýrsla 2015, *Tech. Rep.*, Orkuveita Reykjavíkur (Reykjavik Energy), Reykjavik, Iceland.
Halldorsson, B., S. Olafsson, J. T. Snaebjörnsson, S. Sigurðsson, R. Rupakhety, and R. Sigbjörnsson (2012), On the effects of induced earthquakes due to fluid injection at Hellisheidi Geothermal Power Plant, Iceland, paper presented at 15th WCEE, Lissabon, Portugal.
Haraldsdóttir, S. H. (2014), Mælingareftirlit á vinnslusvæðum Hellisheiðarvirkjunar árið 2014, *Tech. Rep. 2014/052*, ÍSOR, Reykjavik, Iceland.
Hastings, W. K. (1970), Monte Carlo sampling methods using Markov chains and their applications, *Biometrika*, *57*(1), 97–109.
Herring, T., R. W. King, M. A. Floyd, and S. C. McClusky (2015), Introduction to GAMIT/GLOBK, release 10.6, Tech. Rep., Mass. Inst. Technol., Cambridge, Mass.
Hooper, A. (2008), A multi-temporal insar method incorporating both persistent scatterer and small baseline approaches, *Geophys. Res. Lett.*, *35*, L16302, doi:10.1029/2008GL034654.
Hooper, A., D. Bekaert, K. Spaans, and M. Arıkan (2012), Recent advances in SAR interferometry time series analysis for measuring crustal deformation, *Tectonophysics*, *514*, 1–13.
Hreinsdóttir, S., T. Árnadóttir, J. Decriem, H. Geirsson, A. Tryggvason, R. Bennett, and P. LaFemina (2009), A complex earthquake sequence captured by the continuous GPS network in SW Iceland, *Geophys. Res. Lett.*, *36*, L12309, doi:10.1029/2009GL038391.
Hurwitz, S., L. B. Christiansen, and P. A. Hsieh (2007), Hydrothermal fluid flow and deformation in large calderas: Inferences from numerical simulations, *J. Geophys. Res.*, *112*, B02206, doi:10.1029/2006JB004689.
Hutnak, M., S. Hurwitz, S. Ingebritsen, and P. Hsieh (2009), Numerical models of caldera deformation: Effects of multiphase and multicomponent hydrothermal fluid flow, *J. Geophys. Res.*, *114*, B04411, doi:10.1029/2008JB006151.
Jakobsdóttir, S. S. (2008), Seismicity in Iceland: 1994–2007, *Jokull*, *58*, 75–100.
Jeanne, P., J. Rutqvist, D. Vasco, J. Garcia, P. F. Dobson, M. Walters, C. Hartline, and A. Borgia (2014), A 3D hydrogeological and geomechanical model of an enhanced geothermal system at the Geysers, California, *Geothermics*, *51*, 240–252.
Jónsson, S., H. Zebker, P. Segall, and F. Amelung (2002), Fault slip distribution of the 1999 M_w 7.1 Hector Mine, California, earthquake, estimated from satellite radar and GPS measurements, *Bull. Seismol. Soc. Am.*, *92*(4), 1377–1389.
Kampes, B. M., R. F. Hanssen, and Z. Perski (2003), Radar interferometry with public domain tools, paper presented at 3rd International Workshop on ERS SAR Interferometry, 'FRINGE03', p. 6, Frascati, Italy.
Keiding, M., T. Árnadóttir, S. Jónsson, J. Decriem, and A. Hooper (2010), Plate boundary deformation and man-made subsidence around geothermal fields on the Reykjanes Peninsula, Iceland, *J. Volcanol. Geotherm. Res.*, *194*, 139–149.
Kirkpatrick, S., C. Gelatt, and M. P. Vecchi (1983), Optimization by simulated annealing, *Science*, *220*(4598), 671–680.
Metropolis, N., A. W. Rosenbluth, M. N. Rosenbluth, A. H. Teller, and E. Teller (1953), Equation of state calculations by fast computing machines, *J. Chem. Phys.*, *21*(6), 1087–1092.
Minson, S., M. Simons, and J. Beck (2013), Bayesian inversion for finite fault earthquake source models I—Theory and algorithm, *Geophys. J. Int.*, *194*, 1701–1726.

AGU Journal of Geophysical Research: Solid Earth 10.1002/2016JB013626

Mogi, K. (1958), Relations between the eruptions of various volcanoes and the deformations of the ground surfaces around them, *Bull. Earthquake Res. Inst. Univ. Tokyo*, *36*, 99–134.
Mossop, A., and P. Segall (1997), Subsidence at the Geysers geothermal field N. California from a comparison of GPS and leveling surveys, *Geophys. Res. Lett.*, *24*(14), 1839–1842.
Pedersen, R., S. Jónsson, T. Árnadóttir, F. Sigmundsson, and K. L. Feigl (2003), Fault slip distribution of two June 2000 M_w 6.5 earthquakes in South Iceland estimated from joint inversion of InSAR and GPS measurements, *Earth Planet. Sci. Lett.*, *213*(3), 487–502.
Robertson, E. C. (1988), Thermal properties of rocks, *88–441*, US Geol. Surv., Reston, Va.
Sæmundsson, K. (1967), Vulkanismus und Tektonik des Hengill-Gebietes in SW-Island, *Acta Nat. Isl.*, *2*, 105.
Segall, P. (1985), Stress and subsidence resulting from subsurface fluid withdrawal in the epicentral region of the 1983 Coalinga earthquake, *J. Geophys. Res.*, *90*(B8), 6801–6816.
Sigmundsson, F., P. Einarsson, S. Røgnvaldsson, G. Foulger, K. Hodgkinson, and G. Thorbergsson (1997), The 1994–1995 seismicity and deformation at the Hengill triple junction, Iceland: Triggering of earthquakes by minor magma injection in a zone of horizontal shear stress, *J. Geophys. Res.*, *102*, 15,151–15,161.
Tryggvason, A., S. T. Rögnvaldsson, and O. G. Flóvenz (2002), Three-dimensional imaging of the *P*-and *S*-wave velocity structure and earthquake locations beneath Southwest Iceland, *Geophys. J. Int.*, *151*(3), 848–866.
Tryggvason, H. (2014), Mælingareftirlit á Nesjavöllum árið 2014, *Tech. Rep. 2014/060*, ÍSOR, Reykjavik, Iceland.
Turcotte, D. L., and G. Schubert (2002), *Geodynamics*, 2nd ed., Cambridge Univ. Press, Cambridge, U. K.
Vasco, D. W., J. Rutqvist, A. Ferretti, A. Rucci, F. Bellotti, P. Dobson, C. Oldenburg, J. Garcia, M. Walters, and C. Hartline (2013), Monitoring deformation at the Geysers Geothermal Field, California using C-band and X-band interferometric synthetic aperture radar, *Geophys. Res. Lett.*, *40*, 2567–2572, doi:10.1002/grl.50314.
Vogfjörd, K., and R. Slunga (2003), Rupture in the South Iceland Seismic Zone forced by magmatic intrusion in the Hengill area, Abstract 9685 presented at 2003 EGS-AGU-EUG Joint Assembly, vol. 1, Nice, France, 6–11 Apr.
Wessel, P., and W. Smith (1991), Free software helps map and display data, *Eos Trans. AGU*, *72*(41), 445–446.
Wessel, P., W. Smith, R. Scharroo, J. Luis, and F. Wobbe (2013), Generic mapping tools: Improved version released, *Eos Trans. AGU*, *94*(45), 409–410.
Yang, X. M., P. M. Davis, and J. H. Dieterich (1988), Deformation from inflation of a dipping finite prolate spheroid in an elastic half-space as a model for volcanic stressing, *J. Geophys. Res.*, *93*(B5), 4249–4257.

Paper II

Injection-induced surface deformation and seismicity at the Hellisheidi geothermal field, Iceland

Daniel Juncu, Thóra Árnadóttir, Halldór Geirsson, Gunnar Guðmundsson, Björn Lund, Gunnar Gunnarsson, Andy Hooper, Sigrún Hreinsdóttir and Karolina Michalczewska

Submitted to *Journal of Volcanology and Geothermal Research*

Injection-induced surface deformation and seismicity at the Hellisheidi geothermal field, Iceland

D. Juncu[1], T. Árnadóttir[1], H. Geirsson[1], G. B. Guðmundsson[2], B. Lund[3], G. Gunnarsson[4], A. Hooper[5], S. Hreinsdóttir[6], and K. Michalczewska[1]

[1]Nordic Volcanological Center, Institute of Earth Sciences, University of Iceland, Reykjavik, Iceland
[2]Icelandic Meteorological Office, Reykjavik, Iceland
[3]Department of Earth Sciences, Uppsala University, Uppsala, Sweden
[4]OR–Reykjavik Energy, Reykjavik, Iceland
[5]COMET, School of Earth and Environment, University of Leeds, Leeds, UK
[6]GNS Science, Lower Hutt, New Zealand

January 22, 2018

Abstract

Induced seismicity is often associated with fluid injection but only rarely linked to surface deformation. At the Hellisheidi geothermal power plant in south-west Iceland we observe up to 2 cm of surface displacements during 2011–2012, indicating expansion of the crust. The displacements occurred at the same time as a strong increase in seismicity was detected and coincide with the initial phase of geothermal wastewater reinjection at Hellisheidi. Reinjection started on September 1, 2011 with a flow rate of around 500 kg/s. Micro-seismicity increased immediately in the area north of the injection sites, with the largest seismic events in the sequence being two M4 earthquakes on October 15, 2011. Semi-continuous GPS sites installed on October 15 and 17, and on November 2, 2011 reveal a transient signal which indicates that most of the deformation occurred in the first months after the start of the injection. The surface deformation is evident in ascending TerraSAR-X data covering June 2011 to May 2012 as well. We use an inverse modeling approach and simulate both the InSAR and GPS data to find the most plausible cause of the deformation signal, investigating how surface deformation, seismicity and fluid injection may be connected to each other. We argue that fluid injection caused an increase in pore pressure which resulted in increased seismicity and fault slip. Both pore pressure increase and fault slip contribute to the surface deformation.

1 Introduction

Fluid induced seismicity is of great concern because it poses a risk to safety, infrastructure and acceptance of energy production operations. It can either be caused directly by changes in pore pressure due to injection or extraction of fluids, or by stress changes that are induced by the injection or extraction (see Ellsworth, 2013; Zang et al., 2014; Segall and Lu, 2015). Causes of induced earthquakes include injection of fluids (e.g. Healy et al., 1968; Majer and Peterson, 2007; Rutqvist and Oldenburg, 2008; Evans et al., 2012), formation of water reservoirs for hydroelectricity generation (e.g Chopra and Chakrabarti, 1973), secondary recovery of hydrocarbons (e.g. Davis and Pennington, 1989) and production of hydrocarbons (Segall, 1989). Injection of fluids at geothermal sites has caused seismic activity, as described by, e.g., Deichmann and Giardini (2009) and Dorbath et al. (2009). Flóvenz et al. (2015) give an overview of examples of injection related seismicity at geothermal fields in Iceland. At the Hellisheidi geothermal field in SW Iceland seismic swarms have been observed at the injection site at Húsmúli starting with the drilling and testing of boreholes and continuing during injection (see e.g. Flóvenz et al., 2015; Gunnarsson et al., 2015).

Finding a connection between induced seismicity and fluid injection is important to improve our understanding of the generation of fluid driven seismicity. Surface deformation can provide evidence of pore pressure increase caused by wastewater injection, which in turn can cause induced seismicity. Only a few studies report measurements of injection-induced surface deformation linked to seismicity. Such observations have been described by, e.g., Ottemöller et al. (2005) at the Ekofisk oil field in the North Sea, Jahr et al. (2008) at a large-scale injection experiment in south-east Germany and Shirzaei et al. (2016) at an injection site for disposals from oil and gas production in Texas, USA. Fialko and Simons (2000) reported injection related deformation and seismicity at the geothermal site Coso, California, USA. All these studies indicate pore pressure changes as a possible cause (or one of the causes) for the induced seismicity.

In this study we present data describing an episode of simultaneous surface deformation and seismicity at the Hellisheidi high temperature geothermal field in SW Iceland (Figure 1). The field is located within the Hengill Volcanic System which last erupted around 2000 yrs BP. The most recent unrest episode took place between 1993 and 1998, with an increase in earthquake activity in combination with surface uplift (Sigmundsson et al., 1997; Feigl et al., 2000; Clifton et al., 2002). Seismic activity peaked in June and November 1998 with two earthquakes of magnitude M_W 5.4 and 5.1, respectively (Vogfjörd and Slunga, 2003; Jakobsdóttir, 2008). Hengill is at the junction of three segments of the boundary between the North American, Eurasian and Hreppar micro-plate. These segments are the obliquely spreading Reykjanes Peninsula (RP) to the southwest, the Western Volcanic Zone (WVZ) to the north and the $\sim$100 km long, transform-type South Iceland Seismic Zone (SISZ) to the east (Figure 1). In the SISZ, earthquake sequences recur at average intervals of 80–120 years on faults that are predominantly strike-slip with N-S orientation, typical of bookshelf tectonics (Stefánsson and Halldórsson, 1988; Einarsson, 1991). The most recent events of the current sequence occurred in June 2000 with two M_W 6.5 earthquakes (Árnadóttir et al., 2001; Pedersen et al., 2003) and in May 2008 with two M_W 6 earthquakes (Hreinsdóttir et al., 2009; Decriem et al., 2010). The 2008 earthquakes were located approximately

15 km east of the study area at Húsmúli. Both the 2000 and the 2008 events triggered micro-earthquakes in the Hengill area.

Geothermal power production at the Hellisheidi field started in 2006 with an extraction rate of 7 Mton/yr which had been increased to 30 Mton/yr by 2011 (Gunnlaugsson, 2016). A consistent decrease in reservoir pressure of 0.2–0.3 MPa/yr has been observed since 2007 (Haraldsdóttir, 2014). The pressure change causes local surface subsidence; up to $\sim$2 cm/yr between 2012 and 2015 (Juncu et al., 2017). In order to maintain pressure in the reservoir, wastewater re-injection was started in 2007 at the Gráhnúkar site (Figure 1). The second injection site, Húsmúli, was commissioned on 1 September 2011 with an initial flow rate of around 500 kg/s (Gunnarsson, 2013b). After the injection started, increased earthquake activity was observed in the Húsmúli area. The largest events after the beginning of the injection were of magnitude 4 and occurred on 15 October 2011 (Bessason et al., 2012, see locations on Figure 1). They were widely felt in the capital area 20 km to the west. Immediately following the M4 events in October, four Global Positioning System (GPS) benchmarks in the vicinity of Húsmúli were observed semi-continuously for several months to monitor surface deformation (Figure 1). In this study, we will use the so collected GPS data jointly with Interferometric Synthetic Aperture Radar (InSAR) data to measure deformation. We analyze and model the GPS and InSAR data to investigate how the fluid injection at Hellisheidi relates to surface deformation and how the deformation is linked to the seismicity.

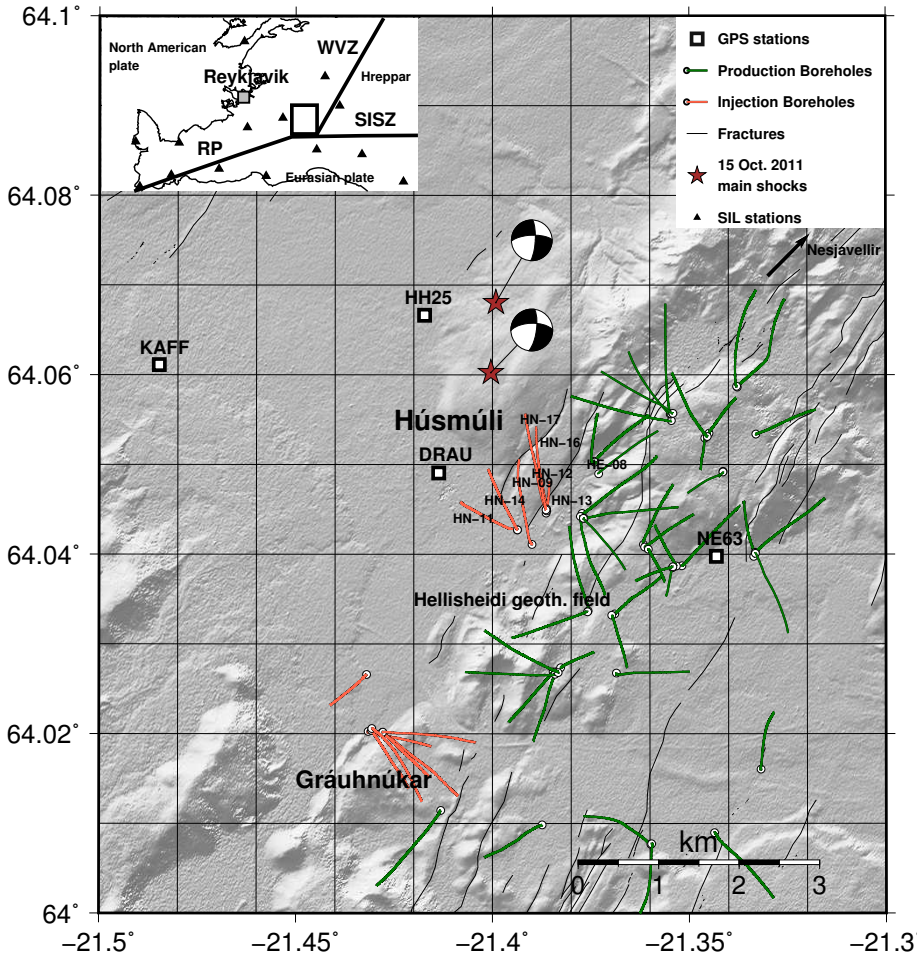

Figure 1: The Hellisheidi geothermal field and the Húsmúli reinjection zone. White squares denote GPS benchmarks used in this study, black lines show mapped surface fractures (Clifton et al., 2002; Einarsson, 2008), green and red lines show trajectories of production and injection boreholes, respectively. The red stars show the location of the 15 October 2011 main shocks, the beach ball plots show their respective focal mechanisms. Seismic stations of the SIL network are shown as black triangles in the insert on the top left. The plate boundary segments are marked as black lines. The segments are: the Reykjanes peninsula (RP), the Western Volcanic Zone (WVZ) and the South Iceland Seismic Zone (SISZ).

2 Seismicity & fluid injection

Seismicity in Iceland is continuously monitored by the national seismic network of Iceland, the SIL network, which has been in operation since 1991 (Böðvarsson et al., 1996, 1999). During 2011 and 2012, twelve seismic stations were located within 50 km of the injection site of which five were within 25 km (Figure 1). The closest SIL seismic station is about 8 km to the west of the injection boreholes. Four of these twelve stations have Lennartz LE-3D/1s sensors, the other eight have Lennartz LE-3D/5s sensors. Most of the stations are equipped with a RD3 digitizer from Nanometrics, the others have a Guralp digitizer. The sampling rate for all stations is 100 Hz. The SIL system automatically detects and locates earthquakes which are then manually quality controlled. The automatic system determines single event locations using the SIL 1D velocity model (Stefánsson et al., 1993). A multi-event double-difference relocation method is available in the system (Slunga et al., 1995). We estimate multi-event locations using a local velocity model for the SISZ (Vogfjörd et al., 2002). Focal mechanisms are calculated for all manually processed events using a spectral amplitude methodology which estimates the double-couple part of the moment tensor (Slunga, 1981; Rögnvaldsson and Slunga, 1993, 1994).

The Húsmúli area first showed signs of induced seismicity with magnitudes up to ∼M2 during the drilling of the production well HE-08 in 2002, and again during drilling and testing of the injection wells HN-12 in 2009 and HN-17 in February 2011 (Figure 1; Björnsson, 2004; Bessason et al., 2012; Gunnarsson, 2013b; Ágústsson et al., 2015). In contrast, the injection at Gráhnúkar (Figure 1), which began in 2007 and had an average injection rate of 170 kg/s in 2011, only caused very little micro-seismicity (Gunnarsson, 2013b; Ágústsson et al., 2015). Injection at Húsmúli started 1 September 2011, with the rate being increased over several days until it reached 480 kg/s on 8 September (Figure 2). Initially, the flow rate was distributed over four boreholes, HN-09, HN-12, HN-14 and HN-17 (Figures 1 & 3). Injection into a fifth borehole, HN-16, began on 23 September. The excess injection pressure was approximately 2.8 MPa (Gunnarsson, 2013a). Pressure increase was observed in nearby boreholes; 0.14 MPa between October 2011 and April 2012 in HN-13 (Gunnarsson, 2013a), and 0.08 MPa between September and November 2011 in HE-08 (Gunnarsson, 2012). Micro-seismicity started to increase around 10 September 2011 (Figure 2), beginning around and north of HN-12 and HN-17 as well as close to HN-14 (Figure 3a). In the following days the activity spread further north of HN-12 and HN-17. Until 16 September this was the main area of activity, highlighting a NNE-SSW striking feature of around 2 km length (see Figure 3b). On 17 September the seismicity spread westward to the area north of HN-14 (Figure 3c). In the following weeks, activity continued in both areas, outlining a second N–S zone parallel to the eastern line of activity (Figure 3d). Two mainshocks occurred on 15 October north of HN-14 within 40 minutes of each other, with local magnitudes of M4 (Figure 3e). For the following three months activity was mainly focused on the eastern and central zones (Figure 3f). In mid-January 2012 the activity shifted approximately 1 km further westwards towards a third structure, south of the GPS station HH25 (Figure 1). This was the main zone of seismic activity until May 2012 (Figure 3g).

The focal mechanisms of the earthquakes, including the two largest events, indicate

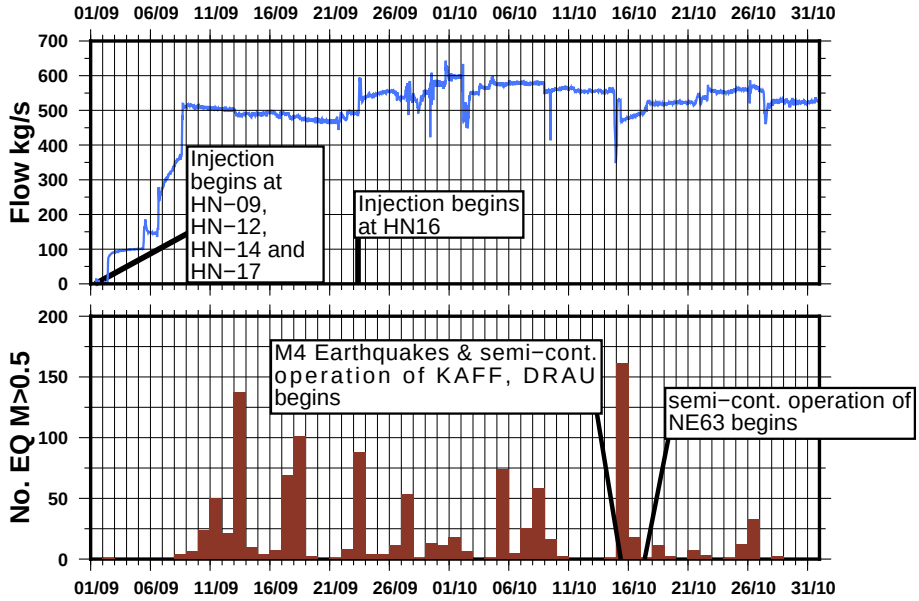

Figure 2: Injection flow rate (top) and daily number of earthquakes (bottom) during September and October 2011 (Bessason et al., 2012). The timeline begins with the start of the injection on September 1, 2011.

primarily right-lateral strike-slip with a small component of normal faulting (Figure 1), on steeply eastward dipping faults. The first of the two M4 events has a strike of 8°, dip of 72° and rake of −152°; the second one has a strike 3°, dip of 76° and rake of −159°. The injection rate has been fairly constant with yearly averages between 380 and 450 kg/s during 2012–2015 (Gunnlaugsson, 2016). Recurrent episodes of increased seismicity have been observed during the same time interval.

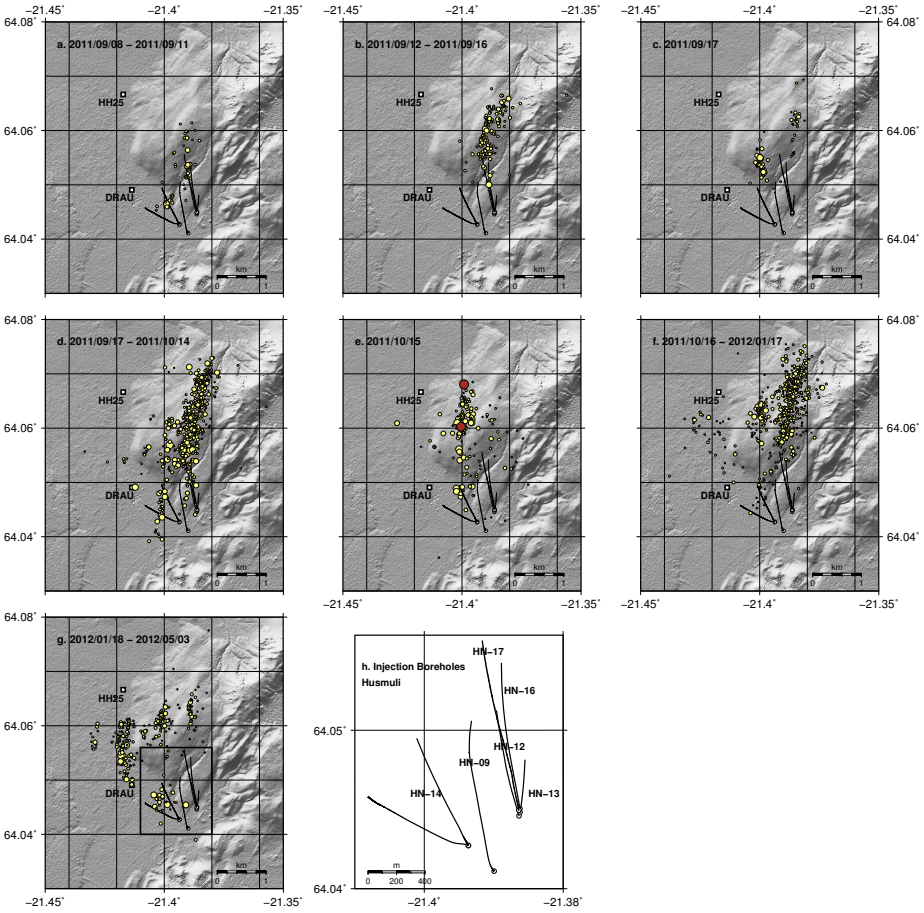

Figure 3: Earthquakes in the vicinity of the reinjection site at Húsmúli (a-g), positions of the small events (yellow circles) are relative relocations. Red circles are M4 main shocks (single event locations), white squares are GPS site locations, labeled with four letter acronyms. Plot h shows borehole locations and names for the injection boreholes within the area outlined with a black rectangle in plot g. The circles indicate the locations of wellheads and the lines show the surface projection of the holes. Borehole depths are between 1.9 km and 3 km.

3 Geodetic data

3.1 GPS

Following the M4 earthquakes on 15 October 2011, four GPS campaign benchmarks in the vicinity of Húsmúli were occupied semi-continuously (continuous deployment but manual data download) for several months. Measurements started on October 15 at DRAU and KAFF, on October 17 at NE63 and on November 2 at HH25 (see Figures 1 and 2). The data were analysed with the GAMIT software, version 10.6 (Herring et al., 2015). Continuous GPS stations in Iceland and over 100 global reference stations were included to determine the daily solutions in the ITRF08 reference frame (Altamimi et al., 2012). To estimate GPS station positions we used the GLOBK software, version 5.29 (Herring et al., 2015).

We use the GPS time series to discern between constant background velocity—consisting of plate motion relative to the reference frame and assumed steady state deformation field—and the transient that started with the injection at Húsmúli (Supplement 1). We calculate the background velocities using pre-transient data to detrend the GPS time-series (Figure 4) and estimate the total transient displacements until mid 2012 to employ them in the joint inversion (Section 4.1). The stations west and northwest of the injection area (HH25, DRAU, KAFF) show a net westward and/or northward motion, whereas NE63, located in the southeast, shows motion to the southeast. We do not include the vertical GPS displacements in this study because we have good constraints on vertical motion from the InSAR data.

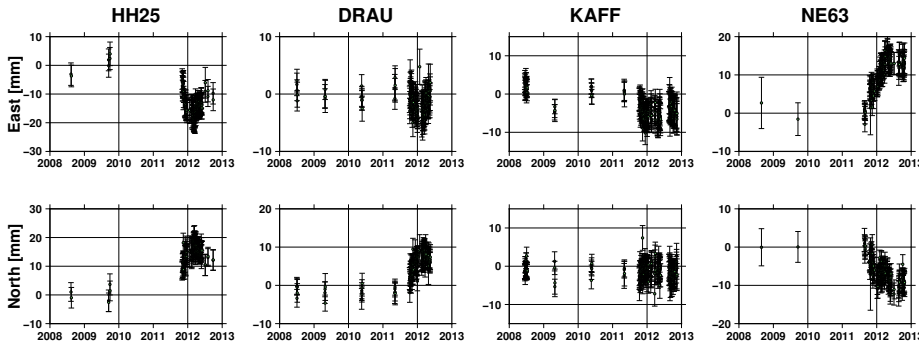

Figure 4: Position time series 2008-2013 of the GPS stations HH25, DRAU, KAFF and NE63. The ITRF08 time series were detrended using the pre-transient velocities (see Supplement 1).

3.2 InSAR

We use satellite-borne synthetic aperture radar (SAR) data, obtained by the TerraSAR-X mission of the German aerospace center (Table 1), in addition to the GPS data to measure surface deformation. Using interferometry (interferometric SAR: InSAR), the SAR acquisitions are processed to obtain relative ground displacements in the line of sight (LOS) of the satellite (see, e.g., Dzurisin, 2007).

TerraSAR-X T41	Configuration
Mode	StripMap
Heading	346.5° (ascending)
Look direction	right
Look Angle	27.2°–29.5°
Altitude	515 km
Latitude	64.05°
Wavelength	31 mm (X-band)
Resolution	3 m
Covered area	50 km x 30 km

Table 1: Satellite and orbit configuration of TerraSAR-X track 41.

We create interferograms with the DORIS software (Kampes et al., 2003) and use the 25 m resolution intermediate TanDEM-X digital elevation model (DEM) to account for topographic contributions to the measured signal. Even though we are only interested in a short time interval covering September 2011 until mid-2012, which is covered by a single interferogram, we use a multitemporal InSAR approach (Hooper, 2008) for which we use the the StaMPS software (Hooper et al., 2012). The multitemporal approach is useful because it results in increased signal-to-noise ratio for the single interferogram that we use. We use a set of 35 interferometric pairs spanning 2009–2015 from TerraSAR-X track 41 to find the pixels that decorrelate little over short time intervals (Hooper, 2008). On the interferograms we suspect to be affected by atmospheric noise we apply a linear phase-correction for tropospheric delay which is based on topography (Bekaert et al., 2015b). We choose an interferogram spanning 30 June 2011 to 03 May 2012 (Figure 5) because of the interferograms that cover the first months after the injection at Húsmúli started, it has the strongest signal-to-noise ratio and shows the least signs of decorrelation. The satellite takes images at close to 30° from the vertical (Table 1) and the average LOS unit vector for the imaged area is $[-0.50, -0.12, 0.86]$ (east, north, up), which means that the measurements are mainly sensitive to vertical and E-W motion. We estimate the full variance-covariance matrix for the spatially correlated InSAR data following the method of Bekaert et al. (2015a). We obtain a variance of $\sigma^2 = 28.8\,\mathrm{mm}^2$, a range of 16.5 km and a nugget term of $0.05\,\mathrm{mm}^2$, which we use to calculate the exponential covariance function. Residual topographic signal and orbit errors are estimated and subtracted during the StaMPS workflow. We assume that any remaining contributions from these sources are taken into account by our approach for estimating the variance-covariance matrix.

To isolate the local signal, we correct the interferogram for plate motion as well as anthropogenic deformation related to the geothermal energy production at the Hengill power plants (i.e., the Hellisheidi and Nesjavellir production areas), using results from Árnadóttir et al. (2009) and Juncu et al. (2017). The most prominent signal that remains is motion of over 20 mm towards the satellite (i.e., mostly upwards and/or westwards) in the Húsmúli area (Figure 5). Because the data have strong spatial correlation, we can downsample them without losing significant information, using a pixel-variance–based quadtree algorithm (Jónsson et al., 2002, see Figure 5).

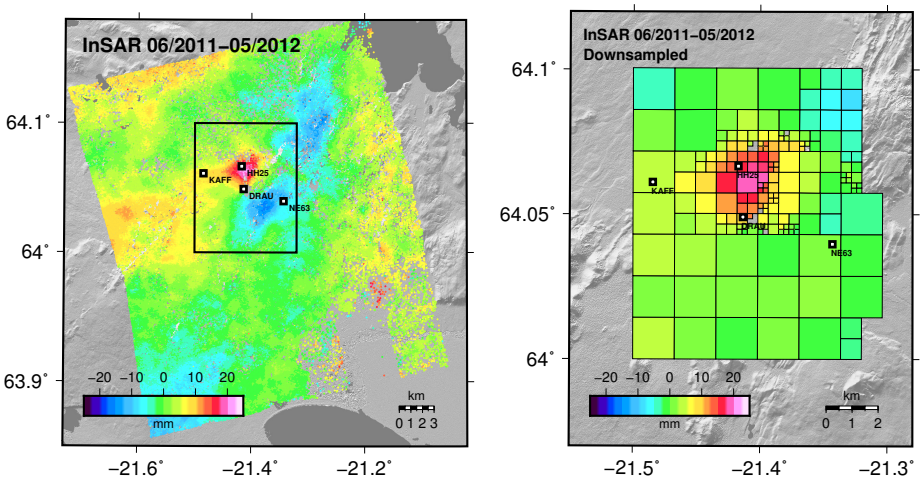

Figure 5: Left: TerraSAR-X interferogram showing Line of Sight (LOS) motion in mm observed from the satellite between 30.06.2011-03.05.2012. Negative values represent motion of the ground away from the satellite, positive values represent motion towards the satellite. Reference value is the mean value of the whole area. The black rectangle contains the data that are subsampled for the right-hand plot. Right: Cropped and downsampled data after being corrected for plate motion, subsidence related to magmatic activity and extraction of geothermal fluids (Árnadóttir et al., 2009; Juncu et al., 2017). The corrected interferogram before downsampling is shown in Supplement 3.

4 Modeling

4.1 Inverse deformation modeling

We test different elastic half-space models to relate subsurface processes to surface deformation: an opening or slipping rectangular dislocation (Okada, 1985), a spherical pressure source (McTigue, 1987) or a pressurized circular crack (Fialko et al., 2001). In all of our models we fix the rheological parameters to a shear modulus of $\mu = 10\,\text{GPa}$ and Poisson's ratio of $\nu = 0.25$, following other studies of deformation in geothermal areas (see Fialko and Simons, 2000; Keiding et al., 2010; Juncu et al., 2017).

We use a nonlinear Bayesian optimization method, CATMIP (Minson et al., 2013), to obtain the model parameters that optimize the fit to the surface deformation. The algorithm uses the annealing method (see Kirkpatrick et al., 1983) and runs multiple Markov chains (e.g. Gelman et al., 2014) to explore the parameter space. This way, it samples the posterior probability density function of the parameter space which is proportional to the product of the likelihood of a tested solution and the prior probability density function of its parameters. The likelihood function $p(\mathbf{D}|\theta)$ allows us to calculate the probability of the observed data $\mathbf{D}$ given a model θ,

$$p(\mathbf{D}|\theta) = \frac{1}{(2\pi)^{N_{dp}/2}|\mathbf{C}|^{\frac{1}{2}}} e^{-\frac{1}{2}\chi^2}, \tag{1}$$

where $\chi^2 = \mathbf{r}^T \mathbf{C}^{-1} \mathbf{r}$. Here, $\mathbf{r}$ is the residual between observed and model data points ($r = d_{obs} - d_{calc}$), $\mathbf{C}$ the data covariance matrix, N_{dp} the number of data points and T is the matrix transpose.

We perform a joint optimization for both GPS and InSAR data. In case of the InSAR data, $\mathbf{C}$ is the full variance-covariance matrix based on spatial correlation between data points (Section 3.2). For the GPS data only the main diagonal of $\mathbf{C}$ is non-zero, containing the variance values of the GPS data and assuming no spatial correlation between data points. The standard deviation of the InSAR data is 5.4 mm (see Section 3.2) and between 2.5 and 3.5 mm for the GPS data (see Supplement 1). We do not apply relative weights between the two datasets.

4.2 Results

Our main interest in this study is to identify the process that causes the observed surface deformation and whether we can connect it to the intense seismic activity. To this end, we run a joint optimization (see above) using the local total displacements that occurred during the transient.

The non-uniqueness of the optimization problem, as well as the many different physical processes that may have caused the observed deformation, make it difficult to select a single optimal solution. We test a variety of elastic half-space models and find several models that fit the data well (see below and Supplement 2). We use additional qualitative constraints to discern whether these models are feasible and how they compare against each other. We present two models (A and B) that we suggest to be the most realistic. Both of them are in agreement with the observations but they have different physical meaning.

4.2.1 Model A: Single source

Model A is a rectangular dislocation for which we only allow opening motion and solve for its location, size, dip and strike (8 free parameters in total). The optimal solution is a roughly 2 by 1 km opening dislocation, dipping 80° towards northwest, opening by 40 cm with a depth to the top of the structure of 1.7 km (see Figure 6, as well as Table 2 for parameter values and confidence intervals). The chi-squared value of the fit is $\chi^2 = 205$, implying 28% variance reduction (null-model: $\chi^2_{nm} = 285$).

The most notable misfit is the northward motion of DRAU. Also, Model A predicts negative LOS motion around the injection-wellheads which is not seen in the data. We show predicted LOS displacements for Model A for the full InSAR dataset in Supplement 3.

4.2.2 Model B: Two sources

Model B combines a spherical pressure source and a right-lateral strike-slip fault. We fix the fault orientation to have a strike of 5° and a dip towards east, in agreement with the majority of the focal mechanisms. The results are shown in Figure 7 and Table S2.5. This model has 13 free parameters and gives a variance reduction of 45%. The spherical pressure source is located at 2.7 km depth (90% confidence interval, CI,

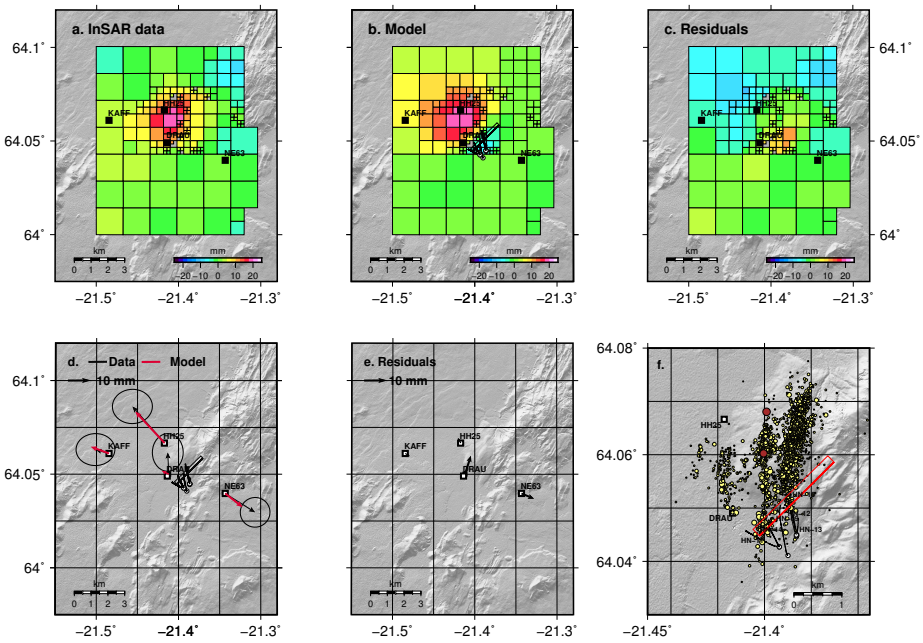

Figure 6: Model A: InSAR data (a), model (b) and residuals (c) in the top row. All in LOS of the satellite. GPS data and model (d), residuals (e), as well as the location of the rectangular dislocation relative to the seismicity and the locations of the injection boreholes (f) in the bottom row. The rectangle marks the dislocation, the bold line representing the upper edge.

Model A		
Free model parameters	8	
No. of data	179	
χ^2	205	
Dislocation		**90% CI**
Longitude [°W]	21.386	(21.371; 21.394)
Latitude [°N]	64.052	(64.045; 64.057)
Length [km]	2.2	(1.2; 4.4)
Width [km]	1.1	(0.2; 2.7)
Depth to top [km]	1.7	(1.0; 2.4)
Dip [°]	80	(63; 90)
Strike [°]	45	(30; 60)
Opening [m]	0.39	(0.11; 0.78)

Table 2: Parameters and 90% confidence intervals for model A after joint inversion of GPS and InSAR data. The shear modulus we use is $\mu = 10\,\text{GPa}$ and Poisson's ratio is $\nu = 0.25$.

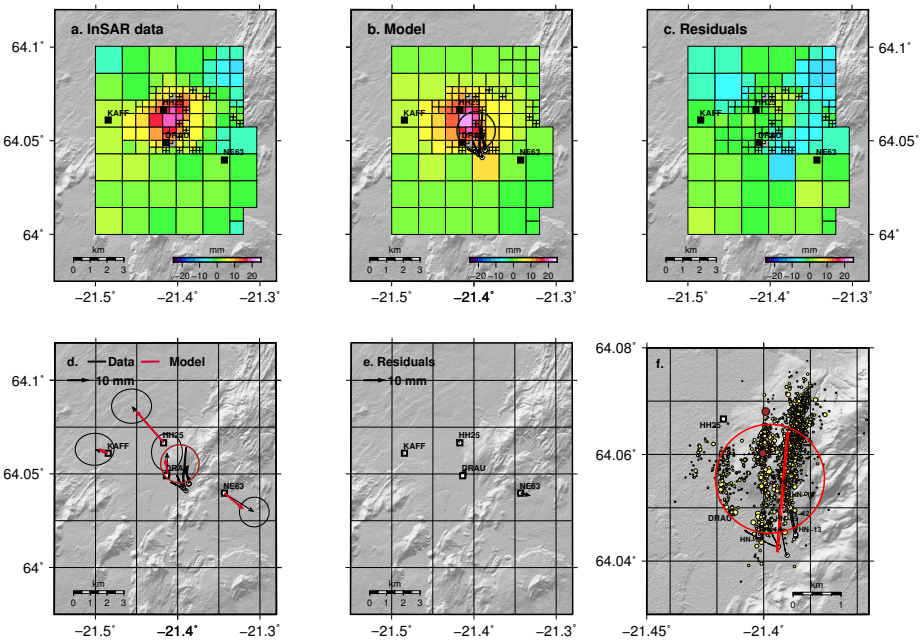

Figure 7: Model B: Spherical pressure source and rectangular dislocation. InSAR data (a), model (b) and residuals (c) in the top row. All in LOS of the satellite. GPS data and model (d), residuals (e), as well as the location of the sources relative to the seismicity and the locations of the injection boreholes (f) in the bottom row. The rectangle marks the dislocation (bold line is the upper edge), the circle the spherical pressure source.

ranging from 2.3–3.0 km), with a radius of 1.1 km (90% CI: 0.8–1.4 km). The center of the sphere is located around 500 m north of the injection sites. The fault has mainly a right-lateral strike-slip component of 45 cm, and minor dip-slip (normal) of 4 cm. It dips 84° to the east and the slip is concentrated between 0.7 km and 1.1 km depth.

Unlike Model A, Model B reproduces the northward motion of DRAU (Figure 7). The positive LOS motion around and south of the injection site, however, can not be seen in the data. This can also be seen when we plot the results for Model B for the full InSAR dataset, as shown in Supplement 3.

Model B		
Free model parameters	13	
No. of data	179	
χ^2	157	
Pressurized sphere		**90% CI**
Longitude [°W]	21.397	(21.380; 21.410)
Latitude [°N]	64.055	(64.048; 64.063)
Depth to center [km]	2.7	(2.2; 3.0)
ΔP [MPa]	1.0	(0.5; 2.0)
Radius [km]	1.1	(0.8; 1.4)
Dislocation		**90% CI**
Longitude [°W]	21.392	(21.388; 21.395)
Latitude [°N]	64.053	(64.051; 64.055)
Length [km]	2.5	(2.1; 3.0)
Width [km]	0.4	(0.2; 0.6)
Depth to top [km]	0.7	(0.5; 1.2)
Dip angle [°]	84	(76; 89)
RL-Strike-slip [m]	0.45	(0.24; 0.80)
Normal slip [m]	0.04	(0.01; 0.11)

Table 3: Parameters and 90% confidence intervals for model B after joint inversion of GPS and InSAR data. The shear modulus we use is $\mu = 10\,\text{GPa}$ and Poisson's ratio is $\nu = 0.25$.

5 Discussion

5.1 Causes of deformation

We observe a transient deformation signal in the area around the Húsmúli injection site (Figures 4 & 5) and investigate how deformation and injection may be linked. The transient starts with the injection in September 2011 and has a peak in total deformation around February/March 2012, before reversing partly and stopping mid-2012 (Figure 4). The spatial deformation pattern during this time interval indicates that part of the deformation stems from an expansive source, because surface displacements are pointing away from the injection site (Figures 6 & 7). We test several subsurface processes that could be responsible for the observed surface displacements:

- expansion of a fracture or layer, caused by local increase in fluid pressure in the vicinity of the injection site (Model A)
- pressure increase in a wider area surrounding the injection site (Model B)
- fault slip (Model B)

In the previous section we presented the models A and B that simulate one or more of these processes and are able to explain the surface deformation at Húsmúli occurring between the beginning of the injection in September 2011 and mid-2012. The combination of spatially dense InSAR data, which are most sensitive to vertical motion, and horizontal GPS data gives us good constraints on the location and the strength of the deformation source(s). However, the deformation signal is small, making it difficult to distinguish between different source types. These models represent different physical processes, both as the cause of deformation and how they may relate to micro-seismicity. We therefore consider qualitatively how the deformation sources could have contributed to the observed induced micro-seismicity and use this to select a preferred model. If a model indicates pore pressure increase around the earthquake foci (model B), the increase of pore pressure can be seen as a direct cause of the seismicity by reducing the effective normal stress on the seismogenic faults. If there is no pressure increase around the foci (model A, if we ignore pore pressure increase due to rock compression), the two most likely possibilities are, (a) the pressure increase does not cause detectable surface deformation but is still a possible cause for the seismicity or, (b) the seismicity is caused by an increase in Coulomb failure stress.

5.2 Fluid flow paths

In order to properly interpret the models we need to consider the possible flow paths of the injected water. The injection was aimed at NE striking fractures that were supposed to lead the fluids towards the northwesternmost production boreholes at Hellisheidi, northeast of the injection site (north of HE-08, see Figure 1). Tracer tests conducted 2013–2015 have confirmed that the injected water was partly recovered in the boreholes to the northeast, but not in holes southeast of the injection site (Kristjánsson et al., 2016). However, the total amount of recovered fluids range between 1% and 57% for the different injection holes (Kristjánsson et al., 2016). The recovery was

estimated by sampling boreholes at the Hellisheidi power plant (Figure 1), none of which are located directly north and northwest of the injection holes. This means that the amount of fluid flow to the north and northwest could not be determined. Khodayar et al. (2015) investigated possible structural flow paths in the Húsmúli area and found—in addition to the ENE striking fractures—northerly, WNW and NW striking, permeable fracture sets. These possible flow directions (North, NW and WNW) are required by Model B (see Section 4.2.2), while model A implies pressure build-up in direct vicinity of the injection site.

The end of the deformation transient in early 2012 indicates a change in the flow regime that caused the end of the pressure build-up. Most likely, this can be explained by two processes. The pressure increase N/NW/WNW of the injection site causes the pressure gradient to diminish, which results in reduced flow towards N/NW/WNW (only applies to model B). And, an increase in permeability towards other directions, caused by the induced seismicity could explain the observations.

5.3 Model A

We interpret Model A as a steeply dipping opening fracture that is fed by the injection and is opening due to pressure increase (see Section 4.2.1). The location of the source is close to the injection site and the northeastern strike agrees with the main fracture orientation in the Hengill area. Hence, Model A offers a possible link between fluid injection and deformation (Figure 6). The opening of a NE-SW trending crack is not outlined by the seismicity (Figure 6), but could have occurred aseismically. An analogy to this might be aseismic magmatic dyke opening (see Ágústsdóttir et al., 2016). This model does not include deformation due to pore pressure increase in the seismically active area, hence the induced seismicity is either caused by a small increase in pore pressure that does not produce detectable surface deformation, or due to an increase in Coulomb failure stress.

We present a slightly altered version of this model in Supplement 2.1 (model S1), where we allow fault slip in addition to opening. Model A is more plausible because model S1 includes significant fault slip while not being aligned with the trend of seismic events. Hence, model A requires only aseismic opening whereas model S1 requires aseismic opening, strike-slip and dip-slip.

5.3.1 Stress changes

Changes in the stress field can bring faults closer to rupture and are a possible cause for induced seismicity (Harris, 1998; Segall and Lu, 2015). Whether or not a fault will fail due to stress changes depends on the change in Coulomb failure stress (ΔCFS, Beeler et al., 2000),

$$\Delta\mathrm{CFS} = \Delta\tau_s + f\left(\Delta\sigma_n + \Delta p\right) \tag{2}$$

where $\Delta\tau_s$ is the change of shear stress in the slip direction, f is the coefficient of friction (which we set to 0.6 following Árnadóttir et al. (2003)), $\Delta\sigma_n$ is the change in normal stress (tensile stress is positive) and Δp is the change in pore pressure.

We calculate static stress changes for Model A and estimate the change in Coulomb failure stress. We assume a receiver fault location in the easternmost zone at Húsmúli

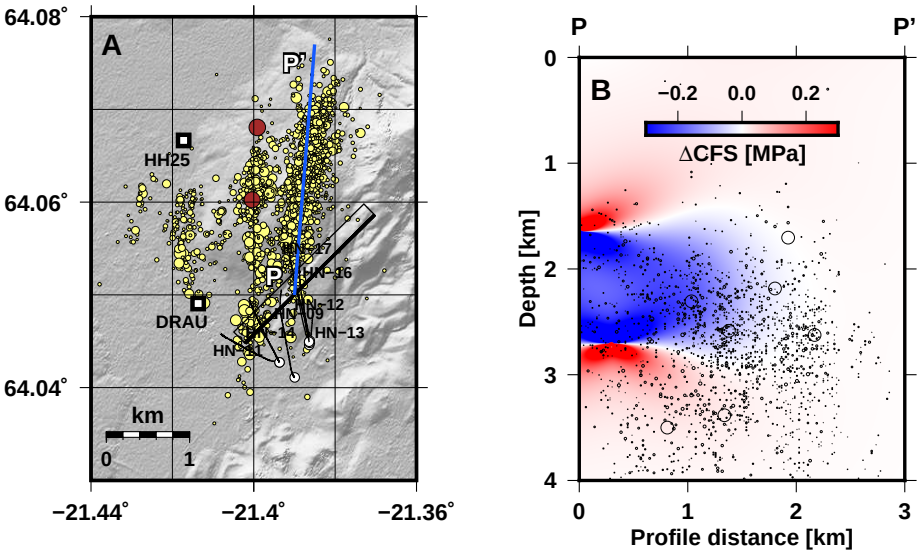

Figure 8: Coulomb failure stress change calculated for model A. Plot A shows the location of the deformation source (black rectangle) and the profile (P-P', blue line) on which ΔCFS is calculated. Yellow circles indicate earthquake locations (relocated from the SIL network), red circles indicate the M4 mainshocks of 15 October 2011. Plot B shows the ΔCFS profile, where warm (red) colors indicate an increase in Coulomb failure stress, cold (blue) colors a decrease. Black circles depict earthquake locations within 200 m of the P-P' profile.

(which is the zone of initial seismic activity), with orientation according to the majority of focal mechanisms in this zone (strike of 5°, dip towards east of 75° and rake of −150°; i.e. right-lateral strike-slip with normal slip component).

As can be seen Figure 8, we find that the majority of earthquakes (occurring at depths between 1.5 an 2.5 km)—and in particular the larger events—experience no change or a reduction in Coulomb failure stress (i.e. moving the receiver faults away from failure). We see no correlation between earthquake locations and changes in Coulomb failure stress and conclude that Model A is an unlikely explanation for the seismicity.

5.4 Model B

We interpret the spherical pressure source in Model B as an area of increased pore pressure (see Section 4.2.2). The center of the pressure source is located around 1 km north of the injection site which could indicate flow towards the north and northwest while flow from the injection site to the southeast is inhibited. From studies of flow paths (Kristjánsson et al., 2016) and structural geology (Khodayar et al., 2015) at Húsmúli (see Section 5.2) this seems quite possible. The pressure source covers much of the volume around the induced micro-seismicity, with the depth range of the source (depth to the center 2 to 3 km) agreeing very well with the depth of the earthquakes. This model therefore offers a plausible explanation for the seismicity, which would

mean that seismogenic faults were pushed towards failure by increase of pore pressure. The pressure increase of 1.0 MPa estimated in this model is poorly constrained by the inversion (90% CI: 0.5–2.0 MPa) and can only be interpreted as an average bulk pressure increase in the area. In reality it is more likely that the pressure increase is most prominent close to the permeable N/WNW/NW fractures and in layers that are fed by those fractures.

The location of the dislocation model was not constrained for the inversion but agrees with the easternmost zone of micro-seismicity in Húsmúli. The fault model, however, does not coincide with the location of the two largest events—which presumably caused most of the co-seismic slip—further west. We tested a model of the surface displacements that would be caused by the two M4 events (Supplement 2.3) and found insignificant deformation. We also tested a model that combines pressure increase and two slipping faults with locations constrained to the zones of most seismicity (Supplement 2.4, Model S4). This model does not fit the data as well as either Model A or Model B.

It should be noted however, that the depth of the slipping part of the fault in Model B, extending from 0.7 to 1.1 km, is shallow compared to the seismicity which mostly occurred between 1.5 and 4.5 km. The seismicity depth, however, is sensitive to the velocity model that was used.

We can estimate the geodetic moment of the fault slip as $M_0 = \mu A u$ (where μ is the shear modulus, A is the fault surface area and u is the amount of slip), and find a value of 4.5×10^{15} N m (which corresponds to a seismic event of magnitude $M = 4.4$, related to M_0 through $M = 2/3 \log M_0 - 6.03$). This is one order of magnitude higher than the cumulative seismic moment released by the earthquakes in the easternmost zone of 0.4×10^{15} N m, based on relocated earthquakes detected by the SIL network. That would indicate that the slip that causes surface deformation is—at least in part—shallow, aseismic slip above the easternmost seismic zone in Húsmúli. This value of the geodetic moment, however, is strongly dependent on the shear modulus. While the value of 10 GPa that we use in our models is not an uncommon assumption (see Fialko and Simons, 2000; Keiding et al., 2010; Juncu et al., 2017), some studies indicate that values of shear modulus may be lower by up one to three orders of magnitude, especially in volcanic areas (e.g. Davis, 1986; Elsworth et al., 2008; Hutnak et al., 2009; Bromley et al., 2013). We test the effect of varying the shear modulus on the inversion results and present the results for $\mu = 1$ GPa in Supplement 2.5. Using this value results in a geodetic moment of 0.3×10^{15} N m, in good agreement with the seismic moment released by the earthquakes. This would indicate that the fault slip inferred from geodetic observations could be linked to the observed seismicity.

Instead of using a spherical pressure source, the pressure increase can be modeled using the pressurized horizontal circular crack model (Fialko et al., 2001), simulating a horizontal aquifer. The result is shown in Supplement 2.6 and very similar to that of Model B. Both models fall short of accurately simulating the complex three-dimensional reservoir geometry. We think, however, that the spherical source is a better representation because it implies that pressure change has a vertical extent which could represent multiple layers of fluid-storing rock formations, rather than a single layer.

5.4.1 Thermal expansion as a possible cause of deformation

Temperature, like pressure, can play a role in deformation in geothermal areas. If the injected fluid is warmer than the rock, thermal expansion can cause deformation (case a), or if (case b), in contrast, water is injected into rock that has a higher temperature, the water can boil and subsequent pressure increase can cause deformation (Hutnak et al., 2009). For case a, the rock must be colder than the water which has a temperature of 80 °C. For case b, water temperature needs to be above its boiling point which is approximately between 280 and 350 °C for depths between 1 and 3 km. While there are no temperature measurements available for the area affected by uplift at Húsmúli, we can look at the temperature distribution in and around the Hellisheidi reservoir (see Supplement 4 and Gunnarsson et al., 2011). The temperature in nearby boreholes is between 200 and 250 °C at 1000 m depth, at a distance of around 1–2 km away from the deforming area. Since we are interested in the area that is slightly outside of the central region of the reservoir we assume that it is unlikely for the temperature in the deforming area to be warmer than 250 °C, i.e. it is unlikely that is hot enough to satisfy case b—greater than 280 °C. At the same time, there are no observations of temperatures below 100 °C in the area (including observations in the peripheral region) which means that it is unlikely that temperatures at Húsmúli are cold enough to satisfy case a, i.e. less than 80 °C. We conclude that it is improbable that thermal effects contribute to the expansive deformation at Húsmúli. That said, the injected fluid is likely to be cooler than the rock formation and may cause contraction of the rock, opposing the pore-pressure driven expansion. Any thermal effect is therefore more likely to reduce the deformation signal, rather than enhance it.

5.4.2 Volumetric expansion compared to volume of injected water

We can compare the volume of injected water to the volumetric expansion of the rock formation to test whether or not the injection can plausibly be linked to the deformation. The expansion of the spherical pressure source in model B is around 4.2×10^5 m^3, given by the relation

$$\Delta V_r = \pi \Delta P a^3 / \mu \tag{3}$$

(Segall, 2010) and the parameters given in Table S2.5. The total volume of injected water between September 2011 and May 2012 is around $\Delta V_f \approx 13 \times 10^6$ m^3 (see Section 2). This implies a volume ratio of $\Delta V_f / \Delta V_r \approx 30$.

The volume change of the rock V_r is related to the volume of injected fluid V_f, and the relation depends on several material parameters (porosity ϕ, Poisson's ratio ν, Biot's coefficient α, bulk modulus of the rock formation K and bulk modulus of the fluid K_f), as described in Juncu et al. (2018):

$$\frac{\Delta V_f}{\Delta V_r} = \frac{1}{f_e}\left[\alpha + \frac{3\phi}{\alpha}\frac{1-\nu}{1+\nu}\left(\alpha - 1 + \frac{K}{K_f}\right)\right]. \tag{4}$$

The factor f_e (with $0 \leq f_e \leq 1$) describes the effective fraction of the injected water that contributes to the deformation. It is 1 if all the injected water contributes to the deformation; it is less than 1 if some fraction is diverted to another area where it does not

cause observable deformation, e.g. because it flows into the reservoir where fluid is being extracted, or because locally higher rock strength (i.e. higher shear/bulk modulus) results in negligible surface deformation.

Equation 4 indicates that fluid compressibility is an important factor when interpreting the volume change of fluid bearing rock formations (see Juncu et al., 2018). This has also been observed in a volcanic setting when comparing calculated subsurface volume change to lava flow volumes (Johnson, 1987), as well as for models of volume changes during magma transfer between magma chambers and dykes (Rivalta and Segall, 2008).

Equation 4 allows us to predict the volume ratio $\Delta V_f/\Delta V_r$ based on material parameters. The bulk modulus of water at 80 °C at pressures between 1 and 10 MPa is $K_f = 2$ GPa (Wagner and Kretzschmar, 2007). The assumed rock's shear modulus of $\mu = 10$ GPa and Poisson's ratio of $\nu = 0.25$ imply a bulk modulus of $K = 17$ GPa (related to μ and ν through $K = 2\mu(1+\nu)/(3(1-2\nu))$). The average recovery from the injection wells in the Hellisheidi reservoir is likely below 50% (see section 5.2). If we assume that all injected water that is not flowing back into the reservoir is contributing to the deformation, this would mean that $f_e > 0.5$ in the Húsmúli area. As a limiting case we will test $f_e = 0.5$. Using likely values for porosity, $0.05 \leq \phi \leq 0.2$, and Biot's coefficient, $0.5 \leq \alpha \leq 1$, (see e.g. Juncu et al., 2018), we find that the maximum possible value we can reach with this parameter combination is $\Delta V_f/\Delta V_r \approx 10$, about one third of the observed volume ratio (see above).

In order to bridge the gap between the observed and the calculated volume ratios we have to revisit the assumptions that we made and consider unmodeled processes that might affect the deformation. We suggest that the following factors may influence the difference between observation and calculations:

- the value of the bulk modulus K. $\Delta V_f/\Delta V_r = 30$ can be reached with $K \approx 45$ GPa, when all other parameters remain unchanged.
- a porosity of $\phi > 0.2$, although changing the porosity alone would not suffice.
- a lower value for f_e (i.e. a smaller fraction of the injected water contributes to the deformation), of around $f_e = 0.15$ with all other parameters unchanged. This requires that a significant amount of the injected water ($> 30\%$) flows neither into the reservoir nor contributes to the deformation.
- if the injected water (80 °C) is colder than the surrounding rock (which is likely, see Section 5.4.1), contraction of the rock may occur, counteracting the expansion due to pore pressure increase.

As discussed in the beginning of Section 5.4, we think that the values for rock strength that we use in this study are already at the upper end of the possible spectrum, i.e. we assume that it is unlikely that $K > 17$ GPa. The porosity of geothermal reservoirs in Iceland is commonly assumed to be around 10% (see e.g. Axelsson et al., 2015). Hence, we think that $\phi > 0.2$ is unlikely. A low value of f_e is possible, but if we consider that only a limited amount of fluid flows back into the reservoir we are left with the question what happens to the portion of the injected liquid that is neither returned to the reservoir nor causes observable deformation. It is possible, however,

that water flows to greater depths where rock strengths are higher, or that it diffuses over greater volume so that the pore pressure increase becomes small. The contraction effect of cooling is a realistic possibility, because cooling related to fluid injection in geothermal reservoirs is a common effect (e.g. at the Geysers geothermal field, USA, see Rutqvist and Oldenburg, 2008). Additional modeling, however, is required to test this hypothesis.

6 Conclusion

Using GPS and InSAR data we find approximately 2 cm of surface displacement occurring during the initial phase of reinjection of waste water at the Hellisheidi power plant. We explore a range of various models to explain the surface deformation and present two in this paper, of which model B is our preferred model. Model B is composed of two deformation sources, a spherical source of expansion and a rectangular dislocation with uniform slip. We argue that it is unlikely that the expansion is caused by thermal effects (Section 5.4.1). We suggest that a local in increase pore-pressure is the cause of the expansion. It is possible, however, that thermal contraction counteracts the expansion due to pore-pressure increase, thus reducing its effect (see Section 5.4.2). We interpret our preferred model (Model B) as the combination of two different processes: an increase in pore pressure, and fault slip in the easternmost zone of induced seismicity. The model implies northward and north-westward flow from the injection site along permeable fractures resulting in pore pressure increase in adjacent formations. The induced pressure change causes surface deformation and increases the effective tensile normal stress on the active faults at Húsmúli. Hence, we assume that the induced seismicity and the fault slip that causes part of the surface deformation are a result of the increased pore pressure. We can not conclusively say whether or not the fault slip is directly linked to some of the micro-seismicity or if it is aseismic. The deformation transient ends when the flow regime changes, either due to permeability increase caused by the seismicity or due to a change in the pressure field caused by the pore pressure increase. Both the continuation of seismic swarms and the lack of subsidence after the deformation transient ended indicate that the pore pressure level remains elevated.

Acknowledgments

The authors would like to thank: Einar Gunnlaugsson from Reykjavik Energy (RE) for providing injection data from Hellisheidi; Bjarni Reyr Kristjánsson (RE) for discussions and advice regarding the geothermal power plant operations and tracer tests; Sarah Minson (U.S. Geological Service) for help with CATMIP and letting us use her code; Elías Rafn Heimisson (Stanford University, USA) for advice regarding Coulomb failure stress calculations; David Bekaert (University of Leeds, UK) for helpful advice on the InSAR processing; Sigurjón Jónsson (King Abdullah University of Science and Technology, SA) for commenting on the manuscript and for providing his Quadtree code; Ólafur Flóvenz (ÍSOR) for comments on the manuscript; the crustal deformation group at IES for help with the GPS measurements in Hengill and discussions on

the work in progress. Earthquake data were provided by the Icelandic Meteorological Office (data submission no. 08-03-2017). For computing the elastic half-space models we use *DMODELS* (Battaglia et al., 2013). We would like to thank Philippe Jousset as well as two anonymous reviewers for their thorough review which helped us improve the manuscript. Many of the figures were prepared using the GMT software (Wessel and Smith, 1991; Wessel et al., 2013). The intermediate TanDEM-X digital elevation model used in the InSAR processing was provided by DLR under project IDEM_GEOL0123. COMET is the NERC Centre for the Observation and Modelling of Earthquakes, Volcanoes and Tectonics. This work was supported in part by grants from the Iceland Research Fund (grant numbers 130371-051/052/053 and 174377-051) and the University of Iceland Research Fund (grant number HI-6489).

References

Ágústsdóttir, T., Woods, J., Greenfield, T., Green, R. G., White, R. S., Winder, T., Brandsdóttir, B., Steinthórsson, S., and Soosalu, H. (2016). Strike-slip faulting during the 2014 Bárðarbunga-Holuhraun dike intrusion, central Iceland. *Geophysical Research Letters*, 43(4):1495–1503.

Ágústsson, K., Kristjánsdóttir, S., Flóvenz, Ó. G., and Gudmundsson, O. (2015). Induced Seismic Activity during Drilling of Injection Wells at the Hellisheiði Power Plant, SW Iceland. In *Proceedings World Geothermal Congress 2015, Melbourne, Australia, 19–25 April 2015*.

Altamimi, Z., Metivier, I., and Collileux, X. (2012). ITRF2008 plate motion model. *J. Geophys. Res.*, 117.

Árnadóttir, T., Hreinsdóttir, S., Gudmundsson, G., Einarsson, P., Heinert, M., and Völksen, C. (2001). Crustal deformation measured by GPS in the South Iceland Seismic Zone due to two large earthquakes in June 2000. *Geophys. Res. Lett*, 28(21):4031–4033.

Árnadóttir, T., Jónsson, S., Pedersen, R., and Gudmundsson, G. B. (2003). Coulomb stress changes in the South Iceland Seismic Zone due to two large earthquakes in June 2000. *Geophysical Research Letters*, 30(5).

Árnadóttir, T., Lund, B., Jiang, W., Geirsson, H., Björnsson, H., Einarsson, P., and Sigurdsson, T. (2009). Glacial rebound and plate spreading: results from the first countrywide GPS observations in Iceland. *Geophys. J. Int.*, 177:691–716.

Axelsson, G., Arnaldsson, A., Berthet, J.-C. C., Bromley, C. J., Gudnason, E. Á., Hreinsdóttir, S., Karlsdóttir, R., Magnússon, I. T., Michalczewska, K. L., Sigmundsson, F., et al. (2015). Renewability Assessment of the Reykjanes Geothermal System, SW-Iceland. In *Proc. of the World Geothermal Congress 2015*.

Battaglia, M., Cervelli, C., and Murray, J. (2013). Modeling crustal deformation near active faults and volcanic centers– A catalog of deformation models. In *U.S. Geological Survey Techniques and Methods, book 13, chap. B1, 96 p.* USGS.

Beeler, N., Simpson, R., Hickman, S., and Lockner, D. (2000). Pore fluid pressure, apparent friction, and Coulomb failure. *Journal of Geophysical Research: Solid Earth*, 105(B11):25533–25542.

Bekaert, D. P. S., Hooper, A., and Wright, T. J. (2015a). Reassessing the 2006 Guerrero slow-slip event, Mexico: Implications for large earthquakes in the Guerrero Gap. *Journal of Geophysical Research: Solid Earth*, 120:1357–1375.

Bekaert, D. P. S., Walters, R. J., Wright, T. J., Hooper, A. J., and Parker, D. J. (2015b). Statistical comparison of InSAR tropospheric correction techniques. *Remote Sensing of Environment*, 170:40–47.

Bessason, B., Ólafsson, E., Gunnarsson, G., Flovenz, O., Jakobsdóttir, S., Björnsson, S., and Árnadóttir, T. (2012). Verklag vegna örvaðrar skjálftavirkni í jarðhitakerfum. Technical report, Orkuveita Reykjavíkur, Reykjavik, Iceland. [In Icelandic].

Björnsson, G. (2004). Reservoir conditions at 3-6 km depth in the Hellisheidi geothermal field, SW-Iceland, estimated by deep drilling, cold water injection and seismic monitoring. In *Proceedings: Workshop on Geothermal Reservoir Engineering. Vol. 29. Stanford University, Stanford Geothermal Program, Stanford, California*, pages 26–28.

Böðvarsson, R., Rögnvaldsson, S. T., , Slunga, R., and Kjartansson, E. (1999). The SIL data aquisition system: At present and beyond year 2000. *Phys. Earth. Plan. Int.*, 113:89–101.

Böðvarsson, R., Rögnvaldsson, S. T., Jakobsdóttir, S. S., Slunga, R., and Stefánsson, R. (1996). The SIL data acquisition and monitoring system. *Seismol. Res. Lett.*, 67:35–46.

Bromley, C., Brockbank, K., Glynn-Morris, T., Rosenberg, M., Pender, M., O'Sullivan, M., and Currie, S. (2013). Geothermal subsidence study at Wairakei–Tauhara, New Zealand. *Proceedings of the Institution of Civil Engineers - Geotechnical Engineering*, 166(2):211–223.

Chopra, A. K. and Chakrabarti, P. (1973). The Koyna earthquake and the damage to Koyna Dam. *Bulletin of the Seismological Society of America*, 63(2):381–397.

Clifton, A. E., Sigmundsson, F., Feigl, K. L., Guðmundsson, G., and Árnadóttir, T. (2002). Surface effects of faulting and deformation resulting from magma accumulation at the Hengill triple junction, SW Iceland, 1994–1998. *J. Volc. Geotherm. Res.*, 115:233–255.

Davis, P. M. (1986). Surface deformation due to inflation of an arbitrarily oriented triaxial ellipsoidal cavity in an elastic half-space, with reference to Kilauea Volcano, Hawaii. *Journal of Geophysical Research: Solid Earth*, 91(B7):7429–7438.

Davis, S. D. and Pennington, W. D. (1989). Induced seismic deformation in the Cogdell oil field of west Texas. *Bulletin of the Seismological Society of America*, 79(5):1477–1495.

Decriem, J., Árnadóttir, T., Hooper, A., Geirsson, H., Sigmundsson, F., Keiding, M., Ófeigsson, B. G., Hreinsdóttir, S., Einarsson, P., LaFemina, P., and Bennett, R. A. (2010). The 2008 May 29 earthquake doublet in SW Iceland. *Geophys. J. Int.*, 181:1128–1146.

Deichmann, N. and Giardini, D. (2009). Earthquakes induced by the stimulation of an enhanced geothermal system below Basel (Switzerland). *Seismological Research Letters*, 80(5):784–798.

Dorbath, L., Cuenot, N., Genter, A., and Frogneux, M. (2009). Seismic response of the fractured and faulted granite of Soultz-sous-Forêts (France) to 5 km deep massive water injections. *Geophysical Journal International*, 177(2):653–675.

Dzurisin, D. (2007). *Volcano Deformation*. Springer.

Einarsson, P. (1991). Earthquakes and present-day tectonism in Iceland. *Tectonophysics*, 189(1):261–279.

Einarsson, P. (2008). Plate boundaries, rifts and transforms in Iceland. *Jökull*, 58(12):35–58.

Ellsworth, W. L. (2013). Injection-induced earthquakes. *Science*, 341(6142):1225942.

Elsworth, D., Mattioli, G., Taron, J., Voight, B., and Herd, R. (2008). Implications of magma transfer between multiple reservoirs on eruption cycling. *Science*, 322(5899):246–248.

Evans, K. F., Zappone, A., Kraft, T., Deichmann, N., and Moia, F. (2012). A survey of the induced seismic responses to fluid injection in geothermal and CO_2 reservoirs in Europe. *Geothermics*, 41:30–54.

Feigl, K. L., Gasperi, J., Sigmundsson, F., and Rigo, A. (2000). Crustal deformation near Hengill volcano, Iceland 1993–1998: Coupling between magmatic activity and faulting inferred from elastic modeling of satellite radar interferograms. *J. Geophys. Res.*, 105(25):655–25.

Fialko, Y., Khazan, Y., and Simons, M. (2001). Deformation due to a pressurized horizontal circular crack in an elastic half-space, with applications to volcano geodesy. *Geophysical Journal International*, 146(1):181–190.

Fialko, Y. and Simons, M. (2000). Deformation and seismicity in the Coso geothermal area, Inyo County, California: Observations and modeling using satellite radar interferometry. *J. Geophys. Res.*, 105:21,781–21,793.

Flóvenz, O. G., Ágústsson, K., Guðnason, E. Á., and Kristjánsdóttir, S. (2015). Reinjection and Induced Seismicity in Geothermal Fields in Iceland. In *Proceedings World Geothermal Congress, Melbourne, Australia, 19–25 April 2015*.

Gelman, A., Carlin, J. B., Stern, H. S., Dunson, D. B., Vehtari, A., and Rubin, D. B. (2014). *Bayesian Data Analysis*. CRC Press Boca Raton, FL, Third edition.

Gunnarsson, G. (2012). Niðurdæling í húsmúla – staða og horfur. Technical report, Orkuveita Reykjavíkur (Reykjavik Energy). [In Icelandic].

Gunnarsson, G. (2013a). Staða niðurdælingarmála. Technical report, Orkuveita Reykjavíkur (Reykjavik Energy), Reykjavik, Iceland. [In Icelandic].

Gunnarsson, G. (2013b). Temperature Dependent Injectivity and Induced Seismicity–Managing Reinjection in the Hellisheiði Field, SW-Iceland. In *GRC Transactions*.

Gunnarsson, G., Arnaldsson, A., and Oddsdóttir, A. L. (2011). Model simulations of the Hengill Area, southwestern Iceland. *Transp Porous Med*, 90:3–22.

Gunnarsson, G., Kristjánsson, B. R., Gunnarsson, I., and Júlíusson, B. M. (2015). Reinjection into a Fractured Reservoir–Induced Seismicity and Other Challenges in Operating Reinjection Wells in the Hellisheidi Field, SW-Iceland. In *Proceedings World Geothermal Congress*.

Gunnlaugsson, E. (2016). Hellisheiði – vinnsluskýrsla 2015. Technical report, Orkuveita Reykjavíkur (Reykjavik Energy), Reykjavik, Iceland. [In Icelandic].

Haraldsdóttir, S. H. (2014). Mælingareftirlit á vinnslusvæðum Hellisheiðarvirkjunar árið 2014. Technical Report 2014/052, ÍSOR, Reykjavik, Iceland. [In Icelandic].

Harris, R. A. (1998). Introduction to special section: Stress triggers, stress shadows, and implications for seismic hazard. *Journal of Geophysical Research: Solid Earth*, 103(B10):24347–24358.

Healy, J. H., Rubey, W. W., Griggs, D. T., and Raleigh, C. B. (1968). The Denver Earthquakes. *Science*, 161(3848):1301–1310.

Herring, T. A., King, R. W., Floyd, M. A., and McClusky, S. C. (2015). Introduction to GAMIT/GLOBK, release 10.6. Technical report, Mass. Inst. Technol., Cambridge, MA, USA.

Hooper, A. (2008). A multi-temporal insar method incorporating both persistent scatterer and small baseline approaches. *Geophys. Res. Lett.*, 35.

Hooper, A., Bekaert, D., Spaans, K., and Arıkan, M. (2012). Recent advances in SAR interferometry time series analysis for measuring crustal deformation. *Tectonophysics*, 514:1–13.

Hreinsdóttir, S., Árnadóttir, T., Decriem, J., Geirsson, H., Tryggvason, A., Bennett, R. A., and LaFemina, P. (2009). A complex earthquake sequence captured by the continuous GPS network in SW Iceland. *Geophysical Research Letters*, 36.

Hutnak, M., Hurwitz, S., Ingebritsen, S. E., and Hsieh, P. A. (2009). Numerical models of caldera deformation: Effects of multiphase and multicomponent hydrothermal fluid flow. *Journal of Geophysical Research: Solid Earth*, 114(B4).

Jahr, T., Jentzsch, G., Gebauer, A., and Lau, T. (2008). Deformation, seismicity, and fluids: Results of the 2004/2005 water injection experiment at the KTB/Germany. *Journal of Geophysical Research: Solid Earth*, 113(B11).

Jakobsdóttir, S. S. (2008). Seismicity in Iceland: 1994–2007. *Jökull*, 58:75–100.

Johnson, D. J. (1987). Elastic and inelastic magma storage at Kilauea volcano. *Volcanism in Hawaii: US Geological Survey Professional Paper 1350*, pages 1297–1306.

Jónsson, S., Zebker, H., Segall, P., and Amelung, F. (2002). Fault slip distribution of the 1999 M_w 7.1 Hector Mine, California, earthquake, estimated from satellite radar and GPS measurements. *Bulletin of the Seismological Society of America*, 92(4):1377–1389.

Juncu, D., Árnadóttir, T., Hooper, A., and Gunnarsson, G. (2017). Anthropogenic and natural ground deformation in the Hengill geothermal area, Iceland. *Journal of Geophysical Research: Solid Earth*, 122(1):692–709.

Juncu, D., Árnadóttir, T., Geirsson, H., and Gunnarsson, G. (2018). The effect of fluid compressibility and elastic rock properties on deformation of geothermal reservoirs. Manuscript submitted for publication.

Kampes, B. M., Hanssen, R. F., and Perski, Z. (2003). Radar interferometry with public domain tools. In *Third International Workshop on ERS SAR Interferometry, 'FRINGE03'*, Frascati, Italy.

Keiding, M., Árnadóttir, T., Jónsson, S., Decriem, J., and Hooper, A. (2010). Plate boundary deformation and man-made subsidence around geothermal fields on the Reykjanes Peninsula, Iceland. *J. Volc. Geotherm. Res.*, 194:139–149.

Khodayar, M., Axelsson, G., and Steingrímsson, B. (2015). Potential Structural Flow Paths for Tracers and Source Faults of Earthquakes at Húsmúli, Hengill, South Iceland. Technical Report 2015/035, ÍSOR.

Kirkpatrick, S., Gelatt, C. D., and Vecchi, M. P. (1983). Optimization by simulated annealing. *Science*, 220(4598):671–680.

Kristjánsson, B. R., Axelsson, G., Gunnarsson, G., Gunnarsson, I., and Óskarsson, F. (2016). Comprehensive tracer testing in the Hellisheidi Geothermal Field in SW-Iceland. In *Proceedings, 41st Workshop on Geothermal Reservoir Engineering*.

Majer, E. L. and Peterson, J. E. (2007). The impact of injection on seismicity at The Geysers, California Geothermal Field. *International Journal of Rock Mechanics and Mining Sciences*, 44(8):1079–1090.

McTigue, D. F. (1987). Elastic stress and deformation near a finite spherical magma body: Resolution of the point source paradox. *J. Geophys. Res.*, 92:12,931–12,940.

Minson, S. E., Simons, M., and Beck, J. L. (2013). Bayesian inversion for finite fault earthquake source models I–theory and algorithm. *Geophys. J. Int.*, 194:1701–1726.

Okada, Y. (1985). Surface deformation due to shear and tensile faults in a half-space. *Bulletin of the Seismological Society of America*, 75(4):1135–1154.

Ottemöller, L., Nielsen, H., Atakan, K., Braunmiller, J., and Havskov, J. (2005). The 7 may 2001 induced seismic event in the Ekofisk oil field, North Sea. *Journal of Geophysical Research: Solid Earth*, 110(B10).

Pedersen, R., Jónsson, S., Árnadóttir, T., Sigmundsson, F., and Feigl, K. L. (2003). Fault slip distribution of two June 2000 M_w 6.5 earthquakes in South Iceland estimated from joint inversion of InSAR and GPS measurements. *Earth and Planetary Science Letters*, 213(3):487–502.

Rivalta, E. and Segall, P. (2008). Magma compressibility and the missing source for some dike intrusions. *Geophysical Research Letters*, 35(4).

Rögnvaldsson, S. T. and Slunga, R. (1993). Routine fault plane solutions for local and regional networks: a test with synthetic data. *Bull. Seismol. Soc. Am.*, 83(4):1232–1247.

Rögnvaldsson, S. T. and Slunga, R. (1994). Single and joint fault plane solutions for miqroearthquakes in South Iceland. *Tectonophysics*, 237:73–80.

Rutqvist, J. and Oldenburg, C. M. (2008). Analysis of injection-induced microearthquakes in a geothermal steam reservoir, the Geysers Geothermal Feld, California. *Lawrence Berkeley National Laboratory*.

Segall, P. (1989). Earthquakes triggered by fluid extraction. *Geology*, 17(10):942–946.

Segall, P. (2010). *Earthquake and Volcano Deformation*. Princeton University Press.

Segall, P. and Lu, S. (2015). Injection-induced seismicity: Poroelastic and earthquake nucleation effects. *Journal of Geophysical Research: Solid Earth*, 120.

Shirzaei, M., Ellsworth, W. L., Tiampo, K. F., González, P. J., and Manga, M. (2016). Surface uplift and time-dependent seismic hazard due to fluid injection in eastern Texas. *Science*, 353(6306):1416–1419.

Sigmundsson, F., Einarsson, P., Røgnvaldsson, S. T., Foulger, G. R., Hodgkinson, K. M., and Thorbergsson, G. (1997). The 1994 – 1995 seismicity and deformation at the Hengill triple junction, Iceland: Triggering of earthquakes by minor magma injection in a zone of horizontal shear stress. *J. Geophys. Res.*, 102:15,151–15,161.

Slunga, R. (1981). Earthquake source mechanism determination by use of body-wave amplitudes - an application to Swedish earthquakes. *Bull. Seismol. Soc. Am.*, 71(1):25–35.

Slunga, R., Rögnvaldsson, S. T., and Böðvarsson, R. (1995). Absolute and relative locations of similar events with application to microearthquakes in southern Iceland. *Geophysical Journal International*, 123(2):409–419.

Stefánsson, R., Böðvarsson, R., Slunga, R., Einarsson, P., Jakobsdóttir, S., Bungum, H., Gregersen, S., Havskov, J., Hjelme, J., and Korhonen, H. (1993). Earthquake prediction research in the South Iceland Seismic Zone and the SIL project. *Bulletin of the Seismological Society of America*, 83(3):696–716.

Stefánsson, R. and Halldórsson, P. (1988). Strain release and strain build-up in the South Iceland seismic zone. *Tectonophysics*, 152(3-4):267–276.

Vogfjörd, K., Nolet, G., Morgan, W., Allen, R., Slunga, R., Bergsson, B., Erlendsson, P., Foulger, G., Jakobsdóttir, S., Julian, B., et al. (2002). Crustal profiling in Iceland using earthquake source-arrays. In *AGU Fall Meeting Abstracts*.

Vogfjörd, K. and Slunga, R. (2003). Rupture in the South Iceland Seismic Zone forced by magmatic intrusion in the Hengill area. In *EGS-AGU-EUG Joint Assembly*, volume 1, page 9685.

Wagner, W. and Kretzschmar, H.-J. (2007). *International Steam Tables: Properties of Water and Steam based on the Industrial Formulation IAPWS-IF97*. Springer Science & Business Media.

Wessel, P. and Smith, W. H. F. (1991). Free software helps map and display data. *EOS, Transactions, AGU*, 72(41):445–446.

Wessel, P., Smith, W. H. F., Scharroo, R., Luis, J., and Wobbe, F. (2013). Generic mapping tools: Improved version released. *EOS, Transactions, AGU*, 94(45):409–410.

Zang, A., Oye, V., Jousset, P., Deichmann, N., Gritto, R., McGarr, A., Majer, E., and Bruhn, D. (2014). Analysis of induced seismicity in geothermal reservoirs – An overview. *Geothermics*, 52:6–21.

Supplement 1: GPS displacements

Here we describe how we obtain the GPS displacements that occurred between the beginning of the injection and May 2012, the date of the second SAR image. In the GPS time series we see constant velocities before injection begins in September 2011 (Figure S1.1). The strong northward component is due to the ITRF08 reference frame. The constant westward background motion is due to plate motion and anthropogenic processes due to extraction of geothermal fluids (Juncu et al., 2017). In order to obtain the local deformation for the same time interval as covered by the InSAR data, we remove these background velocities and obtain the movement that has taken place between the beginning of the injection and May 2012.

We use weighted least-squares to estimate the background velocity (see Figure S1.1) and then calculate the position if no transient had occurred (p_b). Because data for station HH25 are scarce between 2008 and September 2011 (Figure S1.2), we use the velocity of the station during 2012–2015 as the background velocity (–7.0 mm east; 21.4 mm north). We subtract these positions from the observed positions at 3 May 2012 (p_o, as a 10 day average) and obtain the displacements at the station that are caused solely by the transient motion (d_{tr}), free of constant rate signals (i.e., plate motion and geothermal power production) and the effect of the reference frame, thus:

$$d_{tr} = p_o - p_b. \tag{5}$$

We do not estimate the vertical displacements because we have good constraints on the vertical displacements from the InSAR data.

We estimate the uncertainty of the displacements (σ_d) by propagating the errors of the actual positions (σ_{po}, measurement errors) and the estimated transient-free positions (σ_{pb}, errors estimated through least-squares solution) as

$$\sigma_d = \sqrt{\sigma_{po}^2 + \sigma_{pb}^2}. \tag{6}$$

Displacement and standard deviations are shown in Table S1.1.

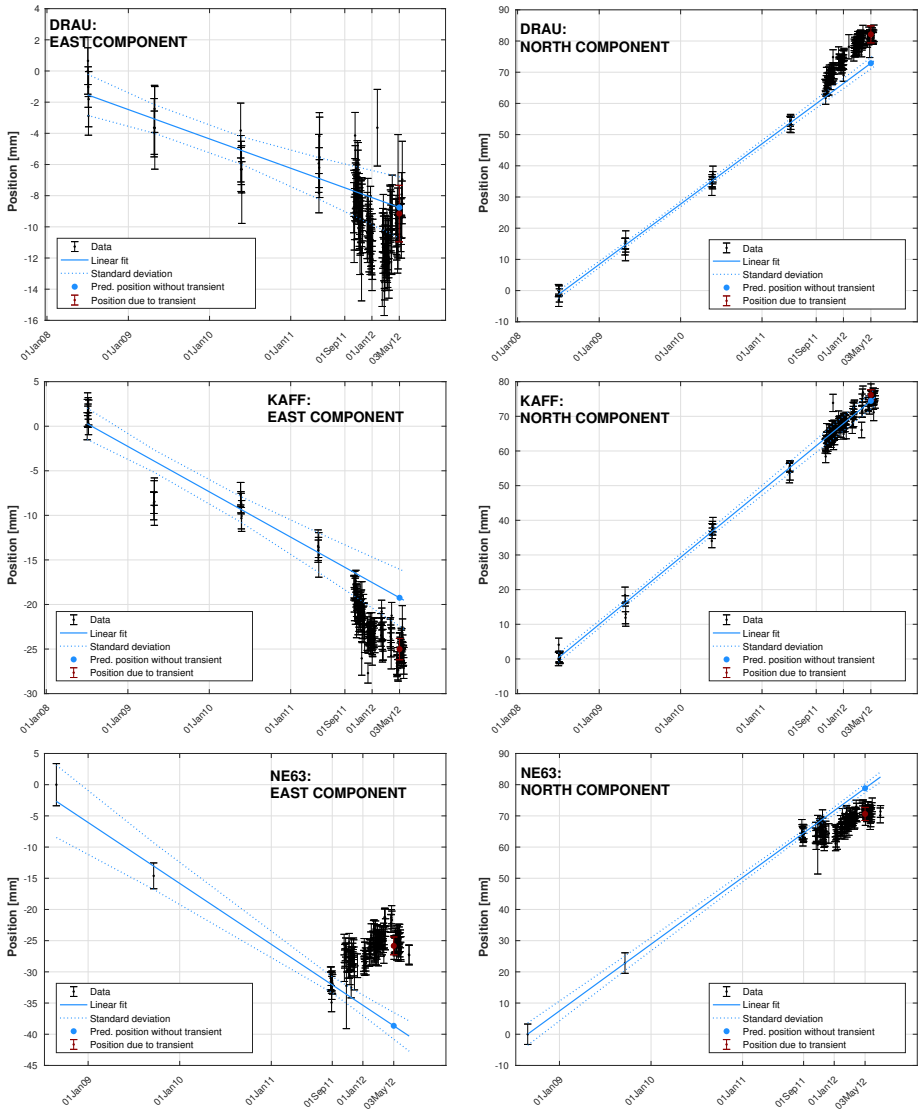

Figure S1.1: North and east components of DRAU, KAFF and NE63 in ITRF08 reference frame. The blue line shows the linear trend of background motion estimated using weighted least squares. The displacement due to a transient signal during 2011–2012 is calculated as the difference between the observed position (red dot) and the estimated position (blue dot), had no transient occurred, assuming a constant velocity.

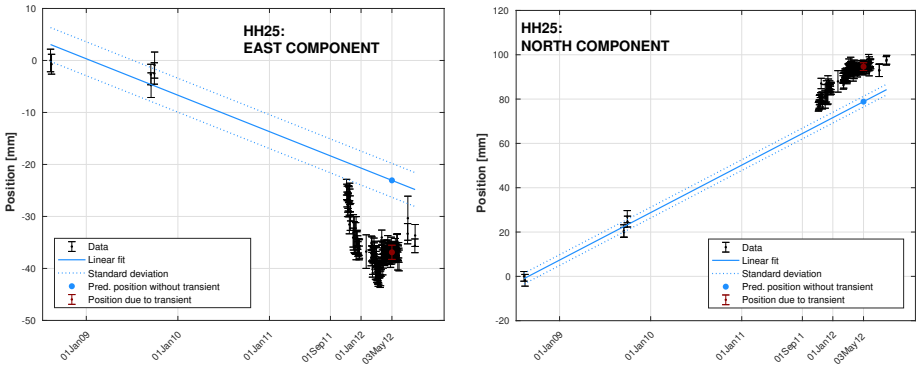

Figure S1.2: North and east components of HH25 in ITRF08 reference frame. The blue line shows the linear trend of background motion using the station velocity during 2012–2015. The displacement due to a transient signal during 2011–2012 is calculated as the difference between the observed position (red dot) and the estimated position (blue dot), had no transient occurred, assuming a constant velocity.

Station	Latitude	Longitude	East [mm]	North [mm]	σ_{east} [mm]	σ_{north} [mm]
DRAU	64.050099	-21.411964	−0.4	9.3	2.7	3.3
NE63	64.039761	-21.343078	12.8	−8.2	2.6	2.6
KAFF	64.061119	-21.484738	−5.8	1.7	3.4	2.8
HH25	64.066686	-21.416985	13.8	15.8	3.5	3.0

Table S1.1: Displacements and standard deviations at the four GPS stations due to the transient (starting September 2011) until 03 May 2012.

Supplement 2: Additional models

Here we show additional models that we explored in this study. All these models assume an elastic halfspace, with a Poisson's ratio ν of 0.25. Model S1 is a variation of model A, where we allow for strike- and dip-slip in addition to opening. In model S3 we test co-seismic fault slip. Models S2 and S4–S6 are variations of model B, where we test: allowing opening in addition to strike- and dip-slip (model S2); adding an additional fault (model S4); reducing the shear modulus from 10 GPa to 1 GPa (model S5); replacing the pressurized sphere by a pressurized horizontal crack (model S6).

S2.1 Model S1: rectangular dislocation, opening, strike-slip and dip-slip

We tested the effect allowing slip on the opening dislocation of model A. It has a better fit than model A ($\chi^2 = 193$ compared to $\chi^2 = 205$ for model A) and has two additional parameters (strike-slip and dip-slip). We think that model S1 is less likely because it implies a considerable amount of strike-slip (64 cm right-lateral slip; although uncertainties are large, see Table S2.1) while the fault does not align with the seismicity trends.

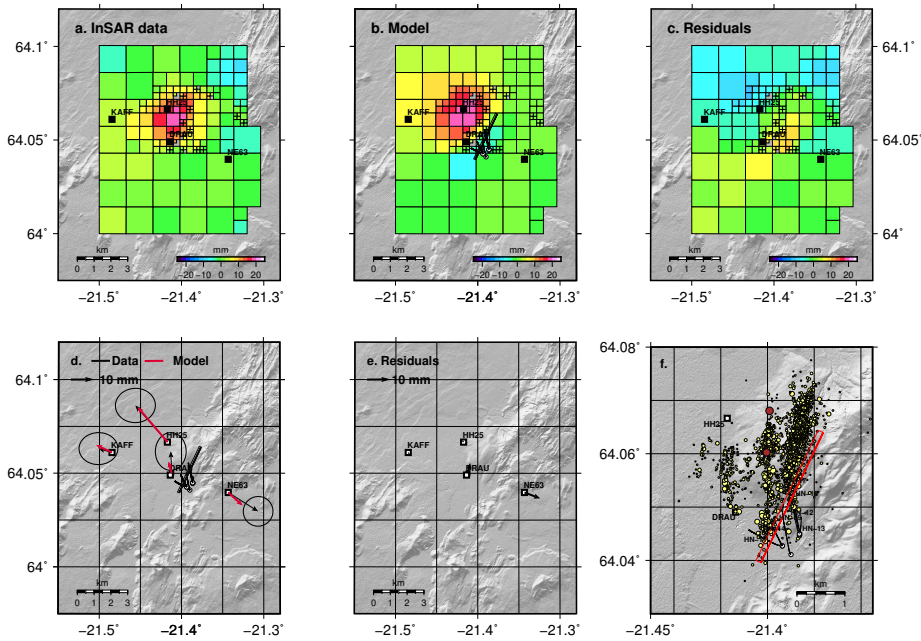

Figure S2.1: Results of model S1. The top row shows InSAR data, model and residuals, the bottom row shows GPS data, model and residuals, as well as the location of the source relative to the seismicity and the injection boreholes. The horizontal pressurized crack is shown as a circle, the dislocation is as a rectangle, with the bold line being the upper edge.

Model S1		
Free model parameters	10	
No. of data	179	
χ^2	193	
Dislocation		**90% CI**
Longitude [°W]	21.386	(21.365; 21.400)
Latitude [°N]	64.052	(64.046; 64.056)
Length [km]	3.0	(1.5; 4.1)
Width [km]	0.4	(0.1; 1.0)
Depth to top [km]	1.8	(1.2; 2.9)
Dip [°]	72	(30; 90)
Strike [°]	26	(13; 84)
Strike-slip [m]	0.64	(-0.73; 0.91)
Dip-slip [m]	0.10	(-0.14; 0.33)
Opening [m]	0.63	(0.20; 0.85)

Table S2.1: Parameters and 90% confidence intervals of model S1 after joint inversion of GPS and InSAR data. Positive strike-slip is right-lateral, negative strike-slip is left-lateral; positive dip-slip is normal slip, negative dip-slip is reverse slip. The shear modulus we use is $\mu = 10\,\text{GPa}$ and Poisson's ratio is $\nu = 0.25$.

S2.2 Model S2: Spherical pressure source and rectangular dislocation allowing strike-slip, dip-slip and opening

Model S2 is a slightly varied version of model B, where we test the effect of allowing opening of the rectangular dislocation in addition to oblique slip. The fit to the data is almost equal between model S2 and model B ($\chi^2 = 155$ compared to $\chi^2 = 157$ in model B). Model S2 has one parameter more than model B.

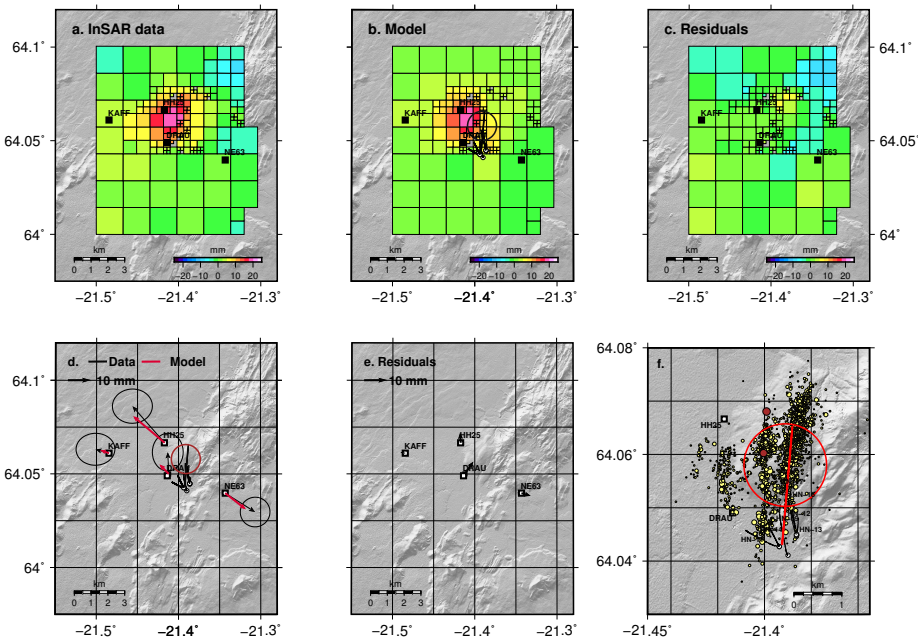

Figure S2.2: Results of model S2. The top row shows InSAR data, model and residuals, the bottom row shows GPS data, model and residuals, as well as the location of the source relative to the seismicity and the injection boreholes. The horizontal pressurized crack is shown as a circle, the dislocation is as a rectangle, with the bold line being the upper edge.

Model S2		
Free model parameters	14	
No. of data	179	
χ^2	155	
Pressurized crack		**90% CI**
Longitude [°W]	21.391	(21.377; 21.406)
Latitude [°N]	64.058	(64.051; 64.067)
Depth to center [km]	2.3	(1.6; 2.9)
Δ P [MPa]	1.1	(0.4; 2.5)
Radius [km]	0.9	(0.7; 1.1)
Dislocation		**90% CI**
Longitude [°W]	21.390	(21.387; 21.393)
Latitude [°N]	64.054	(64.051; 64.057)
Length [km]	2.5	(1.9; 3.1)
Width [km]	0.2	(0.1; 0.4)
Depth to top [km]	0.9	(0.7; 1.4)
Dip angle [°]	86	(78; 90)
RL-Strike-slip [m]	0.78	(0.49; 0.97)
Normal slip [m]	0.09	(0.01; 0.20)
Opening [m]	0.20	(0.07; 0.45)

Table S2.2: Parameters and 90% confidence intervals of model S2 after joint inversion of GPS and InSAR data. The shear modulus we use is $\mu = 10\,\text{GPa}$ and Poisson's ratio is $\nu = 0.25$.

S2.3 Model S3: Co-seismic deformation

Model S3 is a forward model where we fixed all the parameters. Strike, dip and rake were fixed to the known value given by the focal mechanism determined by the SIL network; fault area and amount of slip were estimated from the seismic moment.

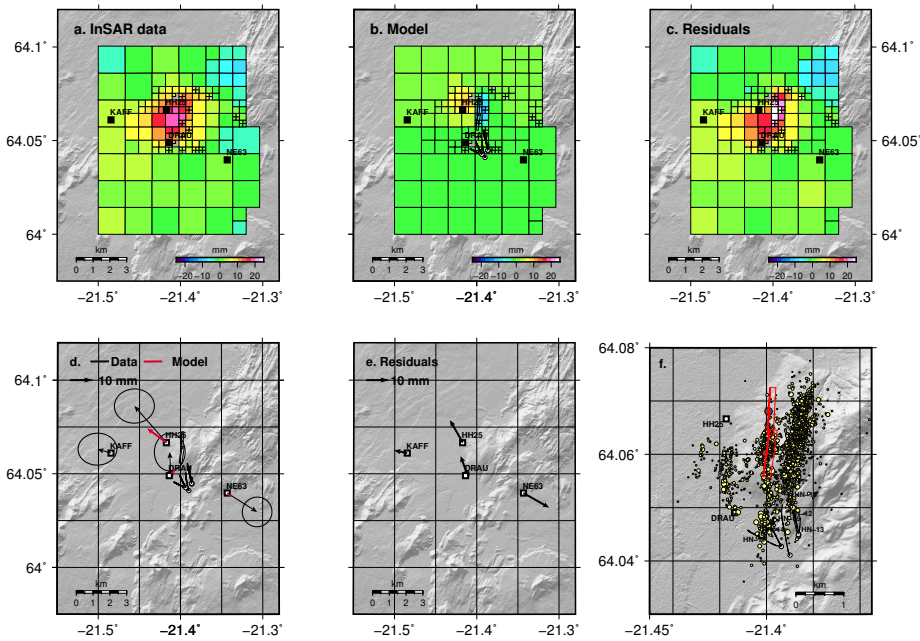

Figure S2.3: Co-seismic deformation due to the two October, 15 2011 earthquakes. The top row shows InSAR data, model and residuals, the bottom row shows GPS data, model and residuals, as well as the location of the source relative to the seismicity and the injection boreholes. The dislocations are shown as rectangles, with the bold line being the upper edge. Yellow circles show earthquakes.

Model S3	
χ^2	292
09:03 Earthquake	
Longitude [°W]	21.399
Latitude [°N]	64.060
Length [km]	1.0
Width [km]	0.5
Depth to top [km]	1.6
Dip [°]	72
Strike [°]	8
Strike-slip [m]	0.2
Dip-slip [m]	0.1
09:46 Earthquake	
Longitude [°W]	21.398
Latitude [°N]	64.068
Length [km]	1.0
Width [km]	0.5
Depth to top [km]	1.6
Dip [°]	76
Strike [°]	3
Strike-slip [m]	0.2
Dip-slip [m]	0.1

Table S2.3: Model parameters for forward modelling co-seismic deformation of the October 15 mainshocks. The shear modulus we use is $\mu = 10\,\text{GPa}$ and Poisson's ratio is $\nu = 0.25$.

S2.4 Model S4: Spherical pressure source and two rectangular dislocations

Model S4 is a variation of model B. We added an additional dislocation, and fixed the locations of both dislocations at the zones of most seismicity. The additional dislocation changes the displacement field resulting in the pressure source being located 3 km NW of the injection site. The residuals are considerably higher than in model B, despite the fact that model S2.4 has four more free parameters.

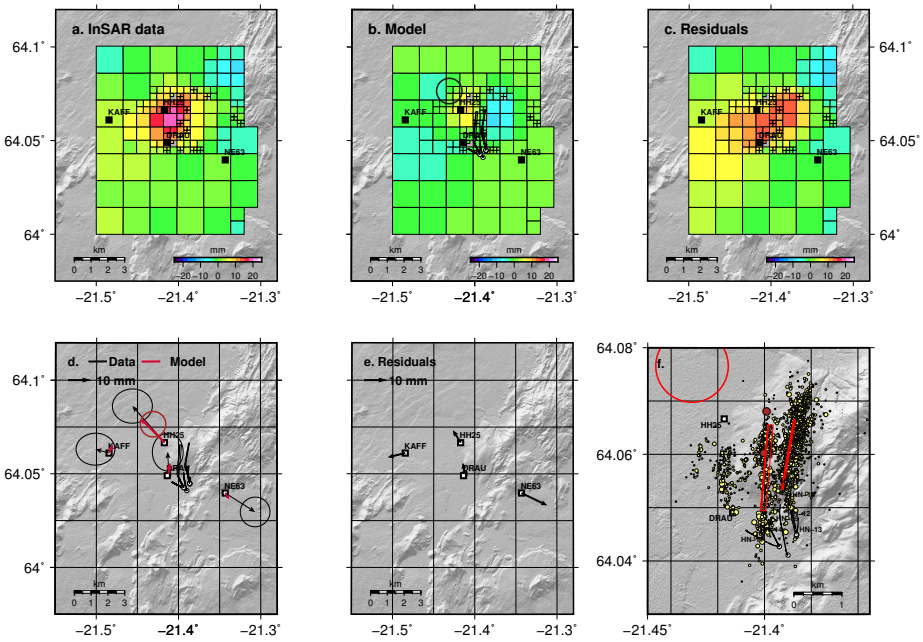

Figure S2.4: Results of model S4. The top row shows InSAR data, model and residuals, the bottom row shows GPS data, model and residuals, as well as the location of the source relative to the seismicity and the injection boreholes. The pressurized sphere is shown as a circle, the dislocations as rectangles, with the bold line being the upper edge.

Model S4		
Free model parameters	17	
No. of data	179	
χ^2	229	
Pressurized sphere		**90% CI**
Longitude [°W]	21.431	(21.414; 21.447)
Latitude [°N]	64.077	(64.071; 64.080)
Depth to center [km]	2.1	(1.5; 2.8)
ΔP [MPa]	1.9	(0.2; 2.9)
Radius [km]	0.8	(0.6; 1.1)
Dislocations		**90% CI**
Longitude [°W]	21.400	-
Latitude [°N]	64.058	-
Length [km]	1.8	(0.6; 5.3)
Width [km]	0.5	(0.1; 1.6)
Depth to top [km]	3.9	(1.6; 4.9)
Dip angle [°]	79	(46; 89)
RL-Strike-slip [m]	0.68	(0.17; 0.96)
Normal slip [m]	0.10	(0.00; 0.45)
Longitude [°W]	21.390	-
Latitude [°N]	64.060	-
Length [km]	1.5	(0.6; 4.3)
Width [km]	0.8	(0.2; 2.4)
Depth to top [km]	1.8	(1.1; 3.5)
Dip angle [°]	88	(81; 90)
RL-Strike-slip [m]	0.65	(0.11; 0.93)
Normal slip [m]	0.29	(0.11; 0.67)

Table S2.4: Parameters and 90% confidence intervals of model S4 after joint inversion of GPS and InSAR data. The shear modulus we use is $\mu = 10\,\text{GPa}$ and Poisson's ratio is $\nu = 0.25$.

S2.5 Model S5: spherical pressure source and rectangular dislocation, $\mu = 1\,\mathrm{GPa}$

In order to test the effect of a varying shear modulus we reduced the value to 1 GPa, compared to 10 GPa in model B. Model S5 results in a slightly better fit than model B ($\chi^2 = 153$ compared to $\chi^2 = 157$ in model B) while both models have the same amount of free parameters.

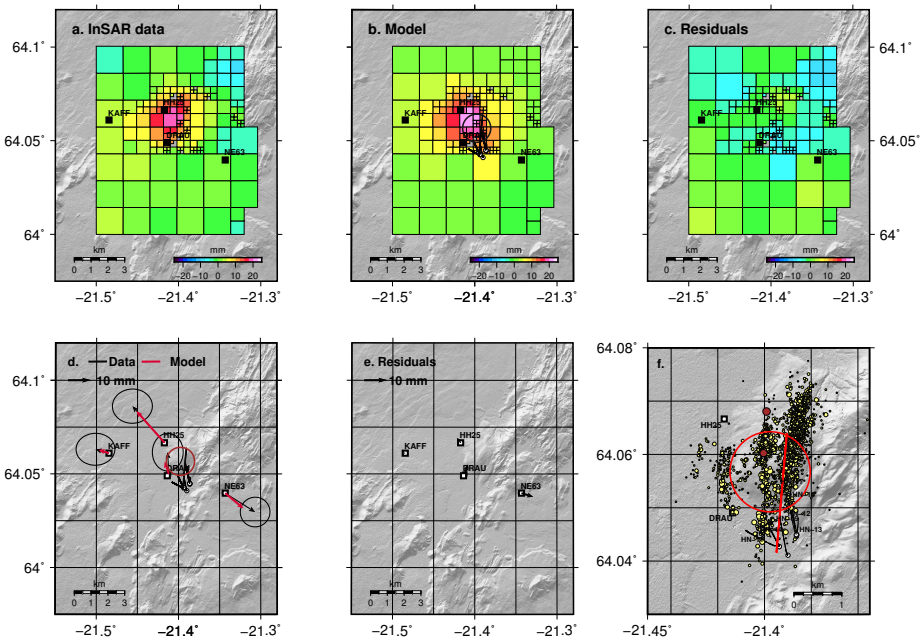

Figure S2.5: Results of model S5. The top row shows InSAR data, model and residuals, the bottom row shows GPS data, model and residuals, as well as the location of the source relative to the seismicity and the injection boreholes. The pressurized sphere is shown as a circle, the dislocation is as a rectangle, with the bold line being the upper edge.

Model S5		
Free model parameters	13	
No. of data	179	
χ^2	153	
Pressurized sphere		**90% CI**
Longitude [°W]	21.398	(21.383; 21.407)
Latitude [°N]	64.057	(64.052; 64.064)
Depth to center [km]	2.5	(2.0; 2.9)
ΔP [MPa]	0.26	(0.09; 0.72)
Radius [km]	0.8	(0.6; 1.2)
Dislocation		**90% CI**
Longitude [°W]	21.393	(21.389; 21.396)
Latitude [°N]	64.053	(64.051; 64.055)
Length [km]	2.5	(2.1; 3.0)
Width [km]	0.2	(0.1; 0.4)
Depth to top [km]	0.7	(0.5; 1.0)
Dip angle [°]	86	(78; 90)
RL-Strike-slip [m]	0.62	(0.32; 0.93)
Normal slip [m]	0.05	(0.01; 0.13)

Table S2.5: Parameters and 90% confidence intervals of model S5 after joint inversion of GPS and InSAR data. The shear modulus we use is $\mu = 1\,\text{GPa}$ and Poisson's ratio is $\nu = 0.25$.

S2.6 Model S6: Pressurized horizontal circular crack and rectangular dislocation

We replaced the spherical pressure source of model B by a circular horizontal pressurized crack (Fialko et al., 2001). In order to make model S6 more comparable to model B we fix longitude and latitude of the pressurized crack to be equal to that of model B. Both models have a similar fit to the data, with model B resulting in slightly smaller weighted residuals ($\chi^2 = 163$ in model S6 compared with $\chi^2 = 157$ in model B) while model S2.6 has two fewer model parameters (due to fixing the crack's position).

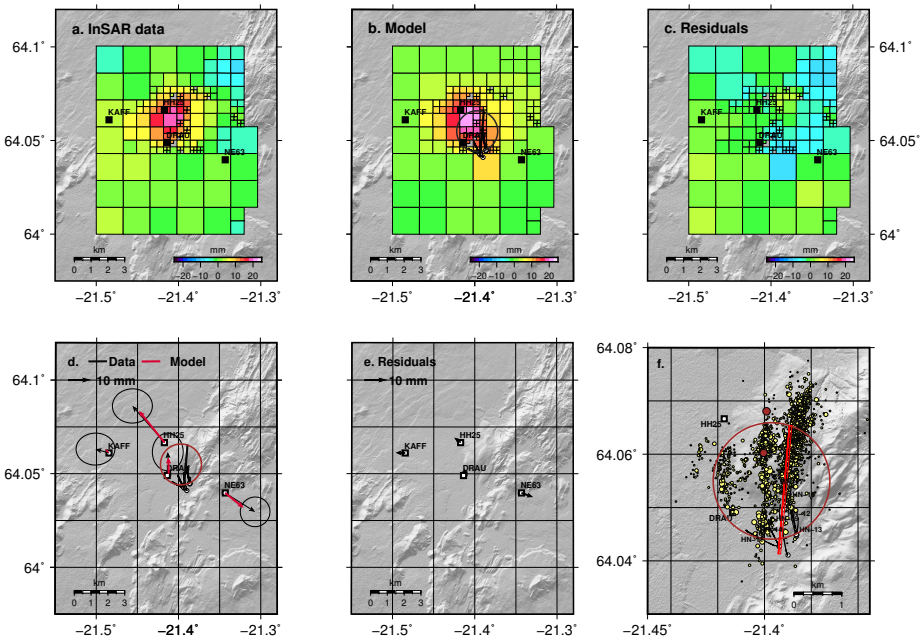

Figure S2.6: Results of model S6. The top row shows InSAR data, model and residuals, the bottom row shows GPS data, model and residuals, as well as the location of the source relative to the seismicity and the injection boreholes. The horizontal pressurized crack is shown as a circle, the dislocation is shown as a rectangle, with the bold line being the upper edge.

Model S6		
Free model parameters	11	
No. of data	179	
χ^2	163	
Pressurized crack		**90% CI**
Longitude [°W]	21.397	-
Latitude [°N]	64.055	-
Depth to center [km]	2.9	(2.4; 3.0)
Δ P [MPa]	1.0	(0.4; 1.5)
Radius [km]	1.2	(0.9; 1.6)
Dislocation		**90% CI**
Longitude [°W]	21.392	(21.388; 21.395)
Latitude [°N]	64.053	(64.051; 64.056)
Length [km]	2.7	(2.1; 3.2)
Width [km]	0.8	(0.3; 1.1)
Depth to top [km]	0.7	(0.5; 1.2)
Dip angle [°]	87	(80; 90)
RL-Strike-slip [m]	0.23	(0.14; 0.49)
Normal slip [m]	0.02	(0.00; 0.06)

Table S2.6: Parameters and 90% confidence intervals of model S6 after joint inversion of GPS and InSAR data. The shear modulus we use is $\mu = 10\,\text{GPa}$ and Poisson's ratio is $\nu = 0.25$.

Supplement 3: Predicted LOS displacements without downsampling

To analyze small scale residuals we plot the joint-inversion results for the full InSAR data without downsampling, both for Model A and for Model B. Both models have significant residuals in the northeastern and eastern parts of the study area. The residuals in the northeastern part can either be residual topographic signal or atmospheric noise or an unmodelled signal in the northern part of Hengill. The residuals in the east, north and west of the GPS station NE63, could be caused by an inaccurate correction for the Hellisheidi production signal.

S3.1 Model A

Model A overpredicts the spatial extent of the positive line-of-sight displacements as can be seen in the residuals in the west and north-west. The model contains negative line-of-sight displacements in the northwestern part of the Hellisheidi production field which can not be seen in the data. A possible explanation is that the actual physical processes do not match the employed model or that they are insufficiently described by the homogeneous character (e.g. the uniform opening) of the model.

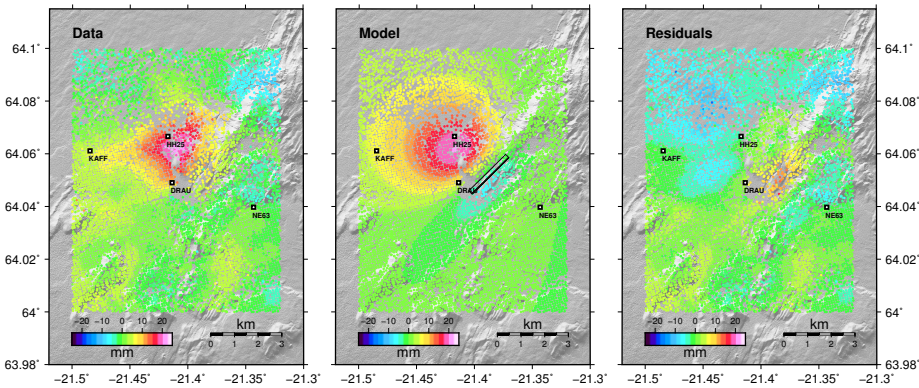

Figure S3.1: Results of Model A for the joint inversion projected calculated for the full InSAR dataset. From left to right, the plots show InSAR LOS changes after correcting for plate motion and production from the geothermal fields (data), LOS changes predicted by Model A and the residuals (difference between data and model). The location of the deformation source is marked in the central plot, the dislocation is shown as a rectangle, with the lines marking the edges and the bold line being the upper edge. The small squares show the locations of the GPS benchmarks.

S3.2 Model B

Model B fits the shape and the magnitude of the main deformation signal very well. It predicts, however, positive line-of-sight motion around the injection site, at the northwestern edge of the Hellisheidi production field. This signal stems from the strike-slip

motion on the modeled fault and might indicate that the slip is overestimated. A possible explanation here is, that the uniform-slip model which we employed too simple and that the actual physical process needs a more complex model to be accurately described.

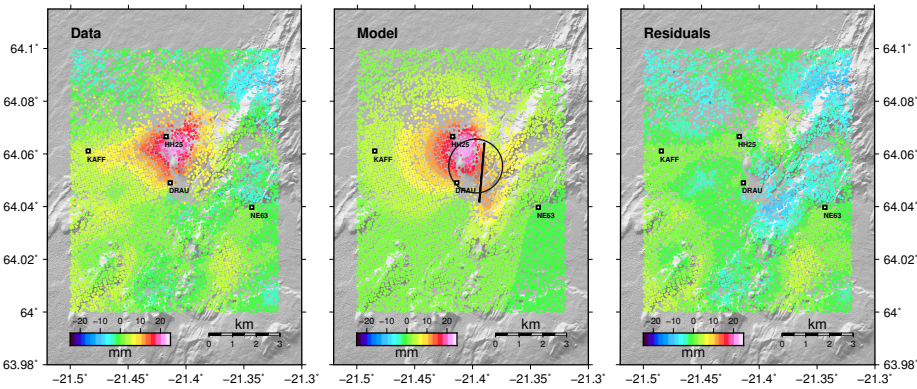

Figure S3.2: Results of Model B for the joint inversion projected calculated for the full InSAR dataset. From left to right, the plots show InSAR LOS changes after correcting for plate motion and production from the geothermal fields (data), LOS changes predicted by Model B and the residuals (difference between data and model). The location of the deformation sources are marked in the central plot, the horizontal pressurized crack is shown as a circle, and the near-vertical dislocation as a line. The small squares show the locations of the GPS benchmarks.

Supplement 4: Temperature distribution in Hengill

The distribution of formation temperature in the Hellisheidi area has been estimated using measurements from the many boreholes in the area at varying depths. Figure S4.1 shows the the interpolated temperature field at 1000 m below sea level.

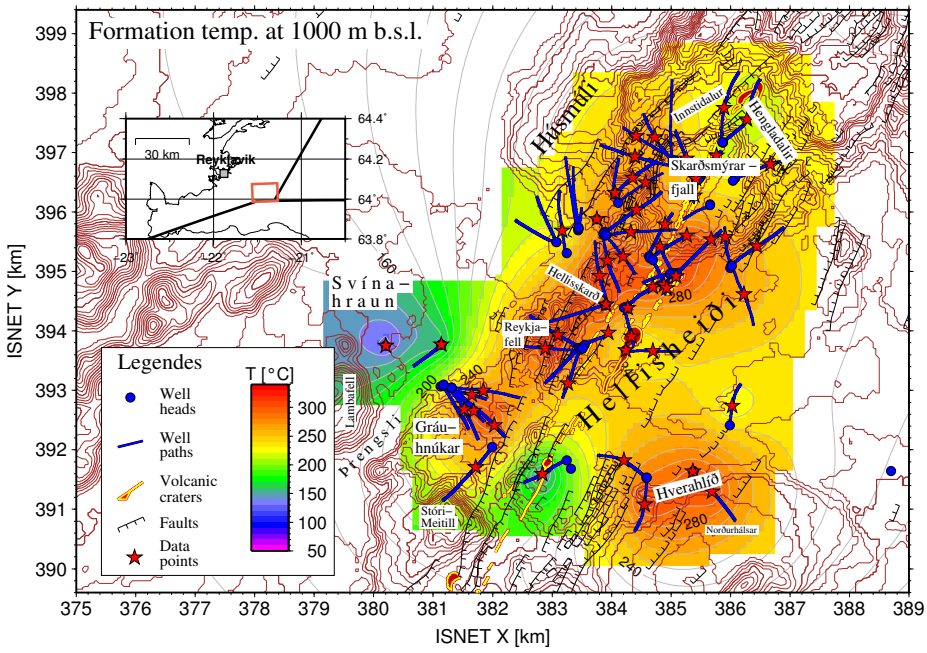

Figure S4.1: Temperature distribution, boreholes (blue dots and lines) and data points (red stars) in the Hellisheidi reservoir at 1000 m depth. The insert shows the location of the depicted area in SW-Iceland.

References

Fialko, Y., Khazan, Y., and Simons, M. (2001). Deformation due to a pressurized horizontal circular crack in an elastic half-space, with applications to volcano geodesy. *Geophysical Journal International*, 146(1):181–190.

Juncu, D., Árnadóttir, T., Hooper, A., and Gunnarsson, G. (2017). Anthropogenic and natural ground deformation in the Hengill geothermal area, Iceland. *Journal of Geophysical Research: Solid Earth*, 122(1):692–709.

Paper III

The effect of fluid compressibility and elastic rock properties on deformation of geothermal reservoirs

Daniel Juncu, Thóra Árnadóttir, Halldór Geirsson and Gunnar Gunnarsson

Submitted to *Geophysical Journal International*.

The effect of fluid compressibility and elastic rock properties on deformation of geothermal reservoirs

D. Juncu[1], Th. Árnadóttir[1], H. Geirsson[1], and G. Gunnarsson[2]

[1]Nordic Volcanological Center, Institute of Earth Sciences, University of Iceland, Reykjavik, Iceland
[2]OR–Reykjavik Energy, Reykjavik, Iceland

March 2, 2018

Abstract

A geothermal reservoir deforms when the extraction of pore fluid exceeds reservoir recharge, causing a decrease in pore pressure. The magnitude of this deformation is related to the amount of pore fluid that is extracted. Assuming compressible material properties in a homogeneous reservoir, we derive an expression for the ratio of reservoir volume change per extracted fluid mass. We show that this ratio depends on a number of parameters, notably the compressibilities of reservoir rock and pore fluid. We apply the obtained relationship to three different case studies to illustrate under which circumstances the relation between reservoir deformation and the amount of extracted fluid is able to help us learn more about reservoir conditions. We find that two-phase fluid compressibility, which can be significantly higher than the single-phase counterparts, can explain estimates of small volume changes in the reservoir per mass unit of extracted fluid. These results indicate that geodetic observations of surface deformation can be used to improve our understanding of rock and fluid properties in geothermal reservoirs.

1 Introduction

Extraction of geothermal fluids can cause significant surface deformation, sometimes with magnitudes reaching the metre-scale as observed at the Wairakei field in New Zealand (e.g. Hatton, 1970; Allis, 2000). With the rise of satellite based geodesy techniques it became possible to detect millimetre-scale surface deformation, resulting in new opportunities to study deformation of reservoir rocks. Many studies have been published in recent years highlighting deformation caused by geothermal fluid extraction and injection observed using InSAR and/or GNSS technology (e.g. Mossop and Segall, 1997, 1999; Fialko and Simons, 2000; Eysteinsson, 2000; Vasco et al., 2002; Foxall and Vasco, 2003; Keiding et al., 2010; Sarychikhina et al., 2011; Ali et al.,

2016; Barbour et al., 2016; Juncu et al., 2017; Drouin et al., 2017). These geodetic observations help us to quantify the deformation around fluid reservoirs, for example by using simple analytical deformation models. Using these models, we can estimate a reservoir's volume change due to contraction or dilatation. This volume change can be compared to observed pressure- or temperature changes or to the amount of fluid extraction/injection. In this study, we focus on the relationship between fluid extraction and the volume change of the reservoir for cases where deformation is driven by changes in pore pressure.

When comparing known volumes of fluid extraction and estimated changes in reservoir volumes, many studies find that the former volume exceeds the latter, sometimes by orders of magnitude (e.g. Eysteinsson, 2000; Keiding et al., 2010; Sarychikhina et al., 2011; Juncu et al., 2017). To examine what causes this difference, we investigate how fluid and reservoir volume changes are related and which parameters control this relation. We describe a simple methodology to help examine plausible parameter combinations and explain the magnitude of deformation for a given amount of extracted fluid. To this end, we derive an equation which shows that the ratio of fluid- to reservoir volume change depends on various reservoir properties, like the bulk compressibility of the reservoir rock and the compressibility of the pore fluid, as well as the fluid exchange with the surrounding formations (i.e., recharge in case of fluid extraction, leakage in case of fluid injection).

The reservoir parameters on which the magnitude of deformation depends are often only poorly constrained. The fluid compressibility in a geothermal reservoir, for instance, can have a wide range of values. If the pore fluid's phase is pure water or pure steam, the compressibility is straightforward to determine (given that temperature and pressure conditions are known) but varies over several order of magnitudes depending on the phase. If, however, the reservoir contains both phases, the fluid compressibility depends on the relative amounts of steam and water, which is often not well known. The bulk rock compressibility at field scale can be difficult to constrain, as well. While it is possible to obtain values of rock strength from laboratory experiments or seismic tomography, the values that are found this way are often higher than the static elastic moduli that prevail in large scale deformation problems (e.g. Heuze, 1980; van Heerden, 1987; Eissa and Kazi, 1988). Furthermore, studies show that bulk compressibility depends on effective stress (Zimmerman et al., 1986), implying a depth dependence of compressibility that needs to be considered, in particular for deformation at shallow depth. The range of values for compressibilities of shallow crustal rocks (less than 3 km depth) found or assumed in deformation studies in geothermal areas varies over orders of magnitude. Bromley et al. (2013) report values of the constrained modulus K_v (relation to the bulk modulus K given in Equation A.3) ranging from 0.01 to 1 GPa, while in other studies of geothermal deformation values of K are assumed to exceed 10 GPa (e.g. Fialko and Simons, 2000; Keiding et al., 2010; Juncu et al., 2017).

Using examples from different geothermal fields, we investigate the link between the magnitude of deformation of geothermal reservoirs and the reservoirs' properties in order to identify combinations of parameter ranges that are able to explain a given magnitude of deformation. We show that it is possible to narrow down parameter ranges using our methodology. Considering the afore mentioned problem in constraining the parameter values using other methods, e.g. laboratory measurements, we should view

man-made reservoir deformation as an opportunity, a large scale experiment, that we can use to learn more about the mechanical behaviour of porous and fractured rocks at field scale. The advantage of the reservoir setting stems from *a priori* knowledge about changes in pore fluid volume and pore pressure. This is information that is generally not available in cases of natural deformation, e.g. driven by magmatic or tectonic processes. Measurements of changes in pore pressure and the amount of extracted fluid can be used to better constrain reservoir conditions and estimate material properties, thus improving our understanding of reservoir processes.

2 Pore fluid and reservoir volume changes

Fluids in rock formations are stored in pores and fractures, where the fluid's pressure, or pore pressure, supports the rock matrix, counter-acting compressional normal stresses. A change in pore pressure can be achieved by a change in volume of pore fluid, which, according to the theory of poroelasticity (Biot, 1941), produces stress and deformation in the rock formation. The theory also implies that the change in stress in the rock in turn produces a change in pore pressure. This two-way coupling makes it difficult to obtain analytical solutions to the equations of poroelasticity. It is possible, however, to turn the two-way coupling into one-way coupling (changes in pore pressure produce changes in stress, but not vice versa) under the assumption of uniaxial strain and constant vertical stress in order to obtain analytical solutions. Geertsma (1966, 1973) used this assumption to derive an expression that relates changes in pore pressure within a fluid reservoir (modelled as a finite structure separated from its surroundings by an impermeable barrier) to surface deformation. The assumption holds for flat axisymmetric reservoirs, see Geertsma (1973), and involves homogeneous material properties (i.e. the properties of reservoir rock and surrounding formations are the same). Figure 1 depicts a sketch of the concept. For more detailed explanations on poroelastic theory we refer the reader to Wang (2000) whose notation we follow in this study.

2.1 Model equation

We use the analytical solution of Geertsma (1966, 1973) and retain the same set of assumptions to obtain a relation for fluid and reservoir volume change. According to Geertsma's work, reservoir volume change ΔV_r of a reservoir with volume V_r, under the condition of constrained strain (Eshelby, 1957), depends on a change in pore pressure Δp, such that:

$$\Delta V_r = c_m V_r \Delta p, \tag{1}$$

where $c_m = \alpha / K_v$ is the uniaxial poroelastic expansion coefficient, K_v is the uniaxial drained bulk modulus (also known as the constrained modulus) of the reservoir and α is Biot's poroelastic expansion coefficient (Geertsma, 1966, 1973; Wang, 2000).

Next we consider the relation between change of pore fluid volume ΔV_f and pore pressure change Δp. The amount of fluid that is moved from/into a control volume given a change in pore pressure depends on both solid and fluid compressibilities.

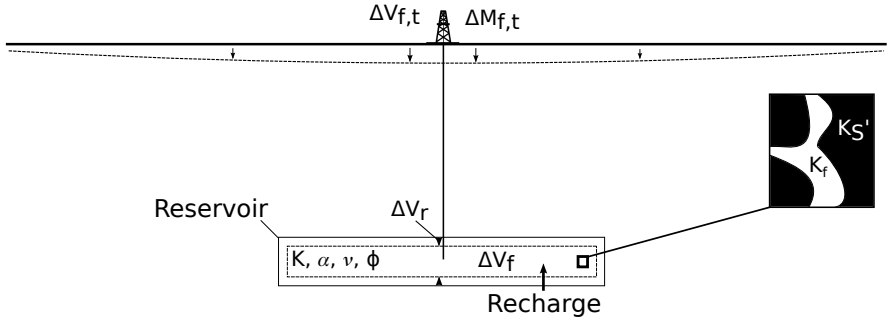

Figure 1: Schematic figure showing subsidence due to extraction of pore fluids. Deformation of the flat subsurface reservoir leads to measurable surface displacements. $\Delta V_{f,t}$ and $\Delta M_{f,t}$ are the total (gross) volume and total mass of extracted fluid. ΔV_r is the volume change of the reservoir due to deformation. ΔV_f is the net volume of extracted fluid, i.e. $\Delta V_{f,t}$ minus recharge. K is the reservoir bulk modulus, K_f is the bulk modulus of the pore fluid and K'_S is the bulk modulus of the solid matrix. α, ν and ϕ are Biot's coefficient, Poisson's ratio and porosity, respectively.

As noted by Geertsma (1957), the former consists of three different compressibilities, namely rock matrix compressibility $1/K'_S$, rock bulk compressibility $1/K$ and pore compressibility $1/K_\phi$. They are linked through a number of poroelastic coefficients, see e.g. Equation A.2. The combined effect of the different compressibilites can be expressed as the specific storage coefficient, S. Knowing this, we can write for a change in pore fluid volume:

$$\Delta V_f = S V_r \Delta p. \tag{2}$$

By taking the ratio $\Delta V_f / \Delta V_r$ we are able to eliminate the $V_r \Delta p$ terms in Equations 1 and 2 and obtain:

$$\frac{\Delta V_f}{\Delta V_r} = \frac{S}{c_m}. \tag{3}$$

Retaining the assumption of uniaxial strain we can write the (uniaxial) specific storage coefficient as (Wang, 2000, Section 3.3.3):

$$S = \frac{\alpha^2}{K_v} + \phi\left(\frac{1}{K_f} - \frac{1}{K_\phi}\right), \tag{4}$$

where $1/K_\phi$ is the unjacketed pore compressibility, $1/K_f$ the compressibility of the pore fluid, α is Biot's expansion coefficient and ϕ is the porosity. We can simplify this equation by assuming that the pore compressibility $1/K_\phi$ equals that of the rock matrix $1/K'_S$ (Equation A.2). This assumption holds for the case of a solid phase consisting

of a single constituent (Berge and Berryman, 1995; Wang, 2000), and is commonly applied to idealize numerical models (see e.g. Zienkiewicz and Shiomi, 1984). Using this assumption and inserting Equations 4 and A.3 into Equation 3, we arrive at:

$$\frac{\Delta V_f}{\Delta V_r} = \alpha + \frac{3\phi}{\alpha}\frac{(1-\nu)}{(1+\nu)}\Big(\alpha - 1 + \frac{K}{K_f}\Big), \tag{5}$$

where ν is Poisson's ratio. A problem with applying Equation 5, is that the net change in pore fluid volume (ΔV_f) is generally not known. The value of ΔV_f depends on the fluid balance in the reservoir, i.e. how much fluid is extracted and how much of the extracted fluid is replenished from surrounding formations or by injection. What we know instead, is the total volume of extracted fluid $\Delta V_{f,t}$, and that ΔV_f equals $\Delta V_{f,t}$ minus recharge into the reservoir. Hence, the value of ΔV_f represents only an *effective* fluid volume change, which we can relate to the known total extracted fluid volume $\Delta V_{f,t}$ by introducing a factor χ, so that

$$\Delta V_f = \chi \Delta V_{f,t}, \tag{6}$$

where $0 < \chi \leq 1$ denotes the fraction of $\Delta V_{f,t}$ that is causing the observed deformation. Within the assumptions of our model, homogeneous material parameters and small vertical extent of the reservoir, this χ essentially depends only on the recharge into the reservoir, which means that in this case, $1-\chi$ is the fraction of $\Delta V_{f,t}$ that is recharged.

Using Equation 6, Equation 5 can be rewritten as:

$$\frac{\Delta V_{f,t}}{\Delta V_r} = \frac{1}{\chi}\left[\alpha + \frac{3\phi}{\alpha}\frac{1-\nu}{1+\nu}\Big(\alpha - 1 + \frac{K}{K_f}\Big)\right]. \tag{7}$$

This shows that the volume ratio of fluid flow and reservoir deformation depends on 6 parameters. Under a set of simplifying assumptions we can illustrate a limiting behaviour of Equation 7. If pore fluid and solid matrix are both incompressible relative to the bulk compressibility of the reservoir ($K << K_f$, $K << K_S'$, $\alpha = 1$), the term in the square brackets in Equation 7 becomes unity so that the ratio of volume changes depends only on χ, i.e. $\Delta V_{f,t}/\Delta V_r = 1/\chi$. In most cases, however, this will not be very realistic, in particular because $K << K_f$ is not a common occurrence.

In high temperature geothermal reservoirs we have to consider an additional problem of two-phase conditions: Water and steam may both be present within the reservoir while their relative fractions of the total fluid volume are unknown. Therefore, it may not be possible to estimate the volume of extracted fluid $\Delta V_{f,t}$, which requires that we use mass instead of volume to quantify the fluid loss from the reservoir. The fluid volume in Equation 7 can be replaced by the total mass of extracted fluid $\Delta M_{f,t}$ by

$$\Delta V_{f,t} = \frac{\Delta M_{f,t}}{\rho_f}, \tag{8}$$

where ρ_f is the bulk fluid density within the reservoir, which depends on the relative fractions of water and steam. We can take Equation 8 and rearrange Equation 7 in terms of the reservoir volume change per total mass extraction $\Delta V_r/\Delta M_{f,t}$:

$$\frac{\Delta V_r}{\Delta M_{f,t}} = \frac{\chi}{\rho_f}\left[\alpha + \frac{3\phi}{\alpha}\frac{1-\nu}{1+\nu}\Big(\alpha - 1 + \frac{K}{K_f}\Big)\right]^{-1}. \tag{9}$$

To find an upper limit for this ratio we can consider the case of an incompressible fluid ($K_f = \infty$), incompressible solid grains ($K'_S >> K$, $\alpha = 1$, see Section 2.1.2), no recharge ($\chi = 1$) and a fluid density of $\rho_f = 1000\,\mathrm{kg\,m^{-3}}$, for which we obtain $\Delta V_r/\Delta M_{f,t} = 10^{-3}\,\mathrm{m^{-3}\,kg^{-1}}$. Any values lower than this are caused by the combined effect of the parameters on the right-hand-side of Equation 9.

2.1.1 Two-phase fluid compressibility

For a two-phase system, the fluid's bulk modulus K_f, or its inverse, the compressibility, depends on the volume fraction of liquid in the system, f_l. Grant and Sorey (1979) give an expression for the compressibility of a fluid in a two-phase system (see also Grant, 2011):

$$\frac{1}{K_f} = \frac{1}{\phi}\langle \rho C \rangle \left(\frac{\rho_w - \rho_s}{L\rho_w\rho_s}\right)^2 T, \tag{10}$$

where $\langle \rho C \rangle$ is the reservoir heat capacity, defined as (Moench and Atkinson, 1978):

$$\langle \rho C \rangle = \phi(1-f_l)\rho_s c_{p,s} + \phi f_l \rho_w c_{p,w} + (1-\phi)\rho_r c_{p,r}. \tag{11}$$

ρ denotes density, c_p specific heat, L the latent heat of vaporization and T the temperature (in Kelvin). Subscripts s, w and r denote steam phase, water phase and rock, respectively.

The density of the water-steam system is a function of the volume fraction of liquid as well, given as (Grant and Sorey, 1979):

$$\rho_f = f_l\rho_w + (1-f_l)\rho_s. \tag{12}$$

We can plug Equations 10, 11 and 12 into Equation 9 and obtain an expression for the reservoir volume change per total mass extraction $\Delta V_r/\Delta M_{f,t}$ in terms of the liquid fraction f_l:

$$\frac{\Delta V_r}{\Delta M_{f,t}} = \frac{\chi}{f_l\rho_w + (1-f_l)\rho_s}\left[\alpha + \frac{3\phi}{\alpha}\frac{1-\nu}{1+\nu}\right.$$
$$\left.\cdot\left(\alpha - 1 + K\left(\left(1-f_l\right)\rho_s c_{p,s} + f_l\rho_w c_{p,w} + \frac{(1-\phi)}{\phi}\rho_r c_{p,r}\right)\left(\frac{\rho_w-\rho_s}{L\rho_w\rho_s}\right)^2 T\right)\right]^{-1}. \tag{13}$$

2.1.2 Model parameters

Equations 7 and 9 contain a number of variables that depend on the physical properties of the reservoir. Here we give a short overview of these parameters as well as the range of values that they commonly assume. For properties of water and steam that depend on temperature and pressure (density, compressibility, heat capacity) we use the tables given in Wagner and Kretzschmar (2007).

Reservoir bulk modulus K. The reservoir bulk modulus (sometimes referred to as wet rock bulk modulus or drained bulk modulus) can vary from $\sim 10^{-2}$ to ~ 10 GPa (see Section 1). Its value depends on rock type, degree of fracturing and confining pressure, which means it may be strongly depth dependent. It can be constrained if pore pressure change and volumetric strain are known or estimated if other material parameters are known (Equation A.4).

Pore fluid's bulk modulus K_f. The fluid's bulk modulus is known in cases where the fluid composition is known. For the case of a two-phase geothermal field where both water and steam occur, K_f can be calculated in terms of the fraction of liquid it contains (see Section 2.1.1). At a pressure of 5 MPa, K_f of liquid water is around 1000 MPa between temperatures of 200 and 250 °C. For steam at 5 MPa, K_f is much lower, around 4 MPa at temperatures between 275 and 325 °C. For a two-phase system at 5 MPa and 264 °C (which is on the boiling point curve), it is the lowest, approximately 0.3 MPa, calculated using Equation 10 for $0 < f_l < 1$, $\phi = 0.1$, $\rho_r = 2500\,\mathrm{kg\,m^{-3}}$, $c_{p,r} = 1.0\,\mathrm{kJ\,kg^{-1}\,°C^{-1}}$, and the properties of water and steam according to the given temperature and pressure (Wagner and Kretzschmar, 2007).

Biot's coefficient α. Biot's expansion coefficient α controls how much of the pore pressure is being transferred onto the solid matrix. It can be expressed in terms of the reservoir bulk modulus K and the solid matrix bulk modulus K'_S, the relation is given in Equation A.2. Theoretically, it can take any value between 0 and 1, where the limiting cases are an incompressible (relative to the bulk reservoir strength) matrix ($K << K'_S \implies \alpha = 1$) and the reservoir bulk modulus being equal to the matrix bulk modulus ($K = K'_S \implies \alpha = 0$). It is commonly assumed, however, that the value of α falls between 0.5 and 1 (e.g. Zienkiewicz and Shiomi, 1984). We also know that the bulk moduli of the mineral components, which control the value of K'_S, are with few exceptions above 30 GPa (e.g. Mavko et al., 2009). This can be used to limit the range of possible values of α. A value of $K < 3$ GPa, for instance, in many cases requires that $\alpha > 0.9$.

Porosity ϕ. The porosity of rocks varies with rock type and confining pressure (i.e., depth) and typically ranges from 0.01 to 0.5 (see Manger, 1963). For hydrocarbon reservoir sandstones and carbonates at 1000 m depth these values are generally below 0.35 (Ehrenberg and Nadeau, 2005). We assume that geothermal reservoirs made up of e.g. volcanoclastic or fractured crystalline rocks do not have higher porosities. For geothermal reservoirs in Iceland, $\phi = 0.1$ is a common assumption for modelling reservoir processes (see e.g. Axelsson et al., 2015). These values can be better constrained by geological information from drill cores or other means.

Poisson's ratio ν. Poisson's ratio is the ratio of transverse strain to axial strain in an elastic medium. For rocks the values of ν fall most commonly between 0.1 and 0.4 (Gercek, 2007).

Fraction of effective fluid volume change χ. The parameter χ quantifies the ratio of the of the net fluid loss ΔV_f in the part of the reservoir exhibiting detectable deformation, to the total volume of extracted fluid $\Delta V_{f,t}$ (Equation 6). In this study we assume that we are able to detect deformation from the whole reservoir, which means that χ only relates to reservoir recharge, which is $1-\chi$. The value of χ ranges from 0 (complete recharge, i.e. no deformation) to 1 (no recharge). It is possible to constrain reservoir recharge using gravity measurements to infer mass changes in the reservoir (e.g. Guðnason et al., 2015).

Liquid volume fraction f_l. The liquid volume fraction is limited by $f_l = 0$ (pure steam) and $f_l = 1$ (pure water). In a geothermal two-phase reservoir it is often not well constrained, because of natural and induced variations in pressure and temperature in space and time. In our model this parameter is, as are all other parameters, averaged over the whole reservoir.

3 Examples: Deformation and fluid extraction at geothermal fields

We can apply the equations we derived in Section 2 to a set of examples where both fluid extraction rates and reservoir volume change are known. Due to parameter trade-off, Equation 9 requires additional constraints to allow any kind of quantitative interpretation. While for some parameters, constraints may be derived from prior information (e.g. examination of drill cores), for others, researchers or reservoir engineers have to rely on experience-based assumptions or adopt values from comparable cases.

We will use three examples to demonstrate how the ratio of deformation per fluid extraction can be used to constrain reservoir parameters and to learn more about reservoir conditions. To this end we employ a Monte Carlo accept-reject approach to sample each parameter in Equation 9 by accepting predicted values of $\Delta V_r/\Delta M_{f,t}$ depending on their difference to the observed value. We take samples from uniform probability distributions over parameter ranges discussed in Section 2.1.2, but use parameter values (or ranges) from the specific study if these are available. Temperature and pressure dependent water and steam properties are taken from Wagner and Kretzschmar (2007). Given the simplifying assumptions that imply homogeneous material parameters, it has to be noted that the resulting range of values depicts an average range in both space and time for the part of the reservoir that is deforming. Here, we study three examples where production of geothermal fluids caused observable surface deformation.

3.1 Hellisheidi, Iceland

The study of Juncu et al. (2017) reports surface deformation due to production at the Hellisheidi high-temperature geothermal field in south-west Iceland between 2012 and 2015. For this case we know the extraction rates from the reservoir in terms of mass rate, which was on average $\Delta M_{f,t} = 38 \cdot 10^9\,\mathrm{kg\,yr^{-1}}$ during the same time interval (Gunnlaugsson, 2016). Of the extracted mass, $\sim$60% was re-injected back into the

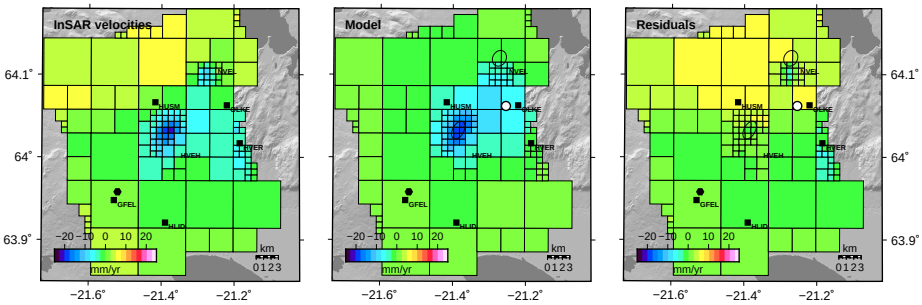

Figure 2: Downsampled InSAR data after correcting for plate motion (see Juncu et al., 2017) and best fitting model after joint optimization of GNSS and InSAR data. Data (left), model (center) and Residuals (right). Black squares denote continuous GNSS stations in the area, the black circle the reference point of the InSAR data.

crust, although it is not certain how much of this fraction flowed back into the reservoir (Juncu et al., 2017b).

In the study of Juncu et al. (2017) a shear modulus of 10 GPa and a Possion's ratio of 0.25 was assumed, which implies a bulk modulus of 17 GPa. However, pressure changes in the Hellisheidi reservoir have been inferred from borehole measurements (Haraldsdóttir, 2014; Juncu et al., 2017) and can be used as an upper bound for an average reservoir pressure decrease. Therefore, we are able to estimate the formation's bulk modulus using the geodetic data. We also invert the surface displacements reported by Juncu et al. (2017) to obtain an estimate for the reservoir volume change using a different reservoir model than in the original study and compare the difference in results.

3.1.1 Inversion of displacement data based on Geertsma's poroelastic model

Using GNSS and InSAR surface displacement data (2012–2015) from the Hellisheidi geothermal area and observed reservoir pore pressure changes (Juncu et al., 2017) we can perform a joint optimization of the two displacement datasets in order to constrain the bulk modulus of the formation. We use the nucleus of strain concept (see e.g. Geertsma, 1966), which can be integrated to obtain displacements for deforming reservoirs of flat cylindrical shape (Geertsma, 1966, 1973; Segall, 1992). Surface displacements for a nucleus of small, finite volume V_n, experiencing a pressure change Δp and located at x_i' are given by

$$u_i(x_1, x_2, 0) = \Delta p V_n c_m \frac{1-\nu}{\pi} \frac{x_i - x_i'}{|D|^3}, \tag{14}$$

where D is the distance between observation point x_i and source location x_i'. We approximate the integral of the nucleus of strain solution over the cylinder by superimposing the displacements caused by a number N of fixed size rectangular cuboids, representing the nuclei of strain. The cuboids are arranged so that they form a horizontal, flat elliptical cylinder of volume $V_r = V_{n,1} + \cdots + V_{n,N}$. We assume that Δp is

constant throughout the reservoir, i.e. the same in each cuboid, and use the observed pressure decrease range at Hellisheidi of 0.3 MPa yr^{-1} (Juncu et al., 2017) as an upper bound for the average reservoir pressure change. We use a Bayesian Markov chain Monte Carlo type inversion approach (the Catmip algorithm, Minson et al., 2013) to find the optimal reservoir source parameters as well as probability distributions of the parameter values (Figure 2 and Supplement Figures S1 and S2). As in Juncu et al. (2017) we correct the data for the plate spreading signal and invert for three local deformation sources, two for the geothermal fields at Hellisheidi and Nesjavellir and a deep source in eastern Hengill. Here, however, we focus only on the results of the Hellisheidi source. We obtain a 90% confidence range for the bulk modulus K of 0.1–6.7 GPa for a given Biot-coefficient range of $0.9 \leq \alpha \leq 1$. We find that the deformation originates from a depth of around 1.2 km (90% confidence interval, CI, ranging from 0.7 to 2.1 km) with a source thickness of 0.6 km (90% CI: 0.4 to 0.9 km). The reservoir volume change is $\Delta V_r \approx 3 \cdot 10^5\,\mathrm{m^3\,yr^{-1}}$ (90% CI: $1 \cdot 10^5$ to $6 \cdot 10^5\,\mathrm{m^3\,yr^{-1}}$), which results in a ratio of reservoir volume change per mass extraction of $\Delta V_r/\Delta M_{f,t} \approx 8 \cdot 10^{-6}\,\mathrm{m^3\,kg^{-1}}$, or, using the confidence interval, gives a 90% confidence range of $4 \cdot 10^{-6}$ to $16 \cdot 10^{-6}\,\mathrm{m^3\,kg^{-1}}$ (neglecting uncertainties in the mass extraction rate). The optimal model for Hellisheidi in the original study (Juncu et al., 2017) is a spheroid with a vertical thickness (at the source center) of 2.5 km (90% CI: 2.0 to 3.0 km) and a reservoir volume decrease of $4 \cdot 10^5\,\mathrm{m^3\,yr^{-1}}$, which is well within the 90% confidence limits of the reservoir volume change estimated here.

3.1.2 Relating $\Delta V_r/\Delta M_{f,t}$ to fluid properties

Having obtained constraints on the reservoir's bulk modulus we can explore the possible parameter combinations that yield $\Delta V_r/\Delta M_{f,t} \approx 8 \cdot 10^{-6}\,\mathrm{m^3\,kg^{-1}}$. The pressure in the central region of the Hellisheidi reservoir is approximately 7 MPa at depths between 1 and 1.5 km (see Haraldsdóttir, 2014) and the reservoir temperature is at the boiling point curve, which is 286 °C at this pressure. We expect the system to be two-phase, because a steam-cap has formed in the top region of the reservoir due to the pressure drop (Gunnarsson et al., 2011). To compare the different scenarios, however, we test the cases of pure steam and pure water, as well. We use Equation 9 and a Monte Carlo accept-reject approach to find the parameter combinations that yield values of $\Delta V_r/\Delta M_{f,t}$ that fall in the 90% confidence range of $4 \cdot 10^{-6}$ to $16 \cdot 10^{-6}\,\mathrm{m^3\,kg^{-1}}$, where parameter combinations that result in values close to the optimal value of $\Delta V_r/\Delta M_{f,t} \approx 8 \cdot 10^{-6}\,\mathrm{m^3\,kg^{-1}}$ are sampled more frequently.

We first test the single-phase case for pure liquid and pure steam just below and above the boiling point curve. For the pure liquid case we assume a density of $\rho_f = 750\,\mathrm{kg\,m^{-3}}$ and a fluid bulk modulus of $K_f = 500$ MPa; for pure steam we use $\rho_f = 35\,\mathrm{kg\,m^{-3}}$ and $K_f = 5$ MPa. For the remaining parameters in Equation 9 we make use of the results from the inversion of geodetic data (Section 3.1.1). In the inversion we obtained a 90% confidence interval of K of 0.1–6.7 GPa, and due to the low values of K we assume that $0.8 < \alpha < 1$ (see Section 2.1.2). We also use a range of $0.01 \leq \phi \leq 0.2$, $0 \leq \chi \leq 1$ and $0.1 \leq \nu \leq 0.4$. We find that these conditions require a very low value of χ, i.e. recharge fractions of greater than ∼80% (for steam) or ∼90% (for water), see Figure 3.

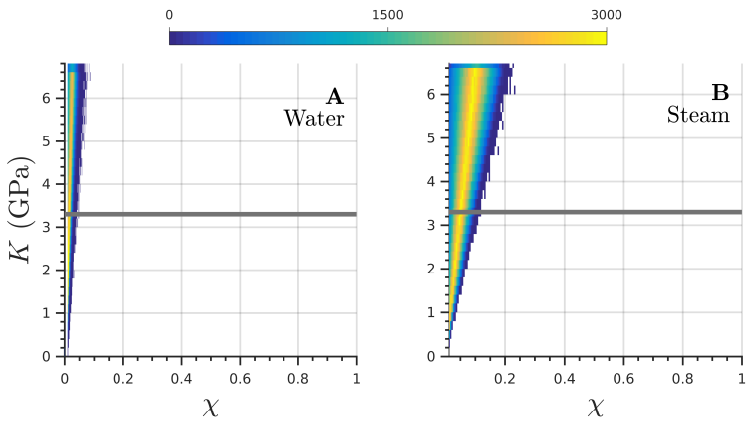

Figure 3: Bivariate histograms for K and χ for a single-phase pore fluid in the Hellisheidi reservoir (Juncu et al., 2017), for pure water (A) and pure steam (B). Frequency of sampled parameter combinations according to color scale. The parameter space was sampled using uniform prior distributions. The horizontal gray line depicts $K = 3.3\,\text{GPa}$.

Next, we test the assumption of a two-phase pore fluid. For this case, the parameter values for these conditions are shown in Table 1. Parameter value ranges of α, K, ϕ, χ and ν are the same as above. Using Equation 10 we can calculate a possible range of K_f of approximately 0.1–3 MPa (depending on the volume fraction of liquid f_l). We show in Figure 4 how the reservoir bulk modulus K and f_l correlate, and find that f_l is very sensitive to K and practically unconstrained for $K < 1\,\text{GPa}$. For the preferred value of $K = 3.3\,\text{GPa}$, determined through the inversion of geodetic data (Section 3.1.1), however, we find that $f_l < 0.3$, which translates to a liquid mass fraction of 90%.

Given the very high required recharge fraction and that we know that both water and steam occur in the reservoir, it seems more likely that the reservoir behaves like a two-phase system. It also shows that with a more accurate estimate of K it may be

Table 1: Parameters of water, steam and rock at temperature on the vapour-liquid saturation curve at 7 MPa and 286 °C; for the Hellisheidi field.

Parameter	Value
T	$559\,\text{K}$
$c_{p,r}$	$1.0\,\text{kJ}\,\text{kg}^{-1}\,\text{K}^{-1}$
$c_{p,w}$	$5.4\,\text{kJ}\,\text{kg}^{-1}\,\text{K}^{-1}$
$c_{p,s}$	$5.4\,\text{kJ}\,\text{kg}^{-1}\,\text{K}^{-1}$
ρ_r	$2500\,\text{kg}\,\text{m}^{-3}$
ρ_w	$740\,\text{kg}\,\text{m}^{-3}$
ρ_s	$37\,\text{kg}\,\text{m}^{-3}$
L	$2.3 \cdot 10^6\,\text{J}\,\text{kg}^{-1}$

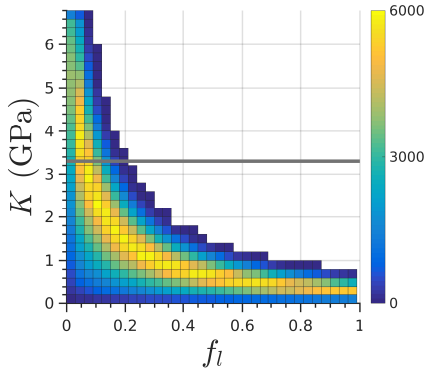

Figure 4: Parameter space depicting possible combinations of the liquid saturation f_l reservoir bulk modulus K for a two phase pore fluid. Calculated using Equation 7 for deformation at the Hellisheidi geothermal field (Juncu et al., 2017), for values of the estimated (through inversion of geodetic data) 90% confidence interval of K (0.1–6.7 GPa); the grey line depicts the inversion's best estimate of $K = 3.3$ GPa. Colour scale depicts the frequency of sampled parameter combinations. The parameter space was sampled using uniform prior distributions.

possible to constrain the ratio of water to steam in the deforming part of the reservoir.

3.2 Reykjanes, Iceland

Keiding et al. (2010) describe deformation between 2005 and 2008 at the Reykjanes geothermal field, located around 80 km south-west of the Hellisheidi field and commissioned in 2006. For this time interval they report a total mass extraction of around 58 Mton and find an estimated reservoir volume change of about $2.1 \cdot 10^6\,\mathrm{m}^3$. Hence, the extracted mass per reservoir volume change is $\Delta V_r/\Delta M_{f,t} \approx 4 \cdot 10^{-5}\,\mathrm{m}^3\,\mathrm{kg}^{-1}$.

For deformation modelling Keiding et al. (2010) assume a shear modulus of $G = 10$ GPa and Poisson's ratio of $\nu = 0.25$, which imply a bulk modulus of $K = 16.7$ GPa. These values were merely assumed and it was not tested whether they are appropriate in a deformation context. Looking at reservoir pressure change and volumetric strain at Reykjanes we can test if the values are realistic, by rearranging Equation 1 (and using Equation A.3):

$$K = \frac{1}{3}\frac{(1+\nu)}{(1-\nu)}\alpha\Delta p\frac{V_r}{\Delta V_r}. \tag{15}$$

Keiding et al. (2010) found $\Delta V_r \approx 0.002\,\mathrm{km}^3$ and $V_r \approx 19\,\mathrm{km}^3$. The values of V_r and ΔV_r imply a pressure decrease of $\Delta p \approx 1$ MPa using the constrained-strain relation for prolate spheroids given by Amoruso and Crescentini (2009): $\Delta V_r = V_r \Delta p/G$, where $G = 10$ GPa is the shear modulus used by Keiding et al. (2010). To approximate an upper bound for K, we assume the limiting case of incompressible solid grains, i.e. $\alpha = 1$, and a Poisson's ratio of $\nu = 0.4$, and find that $K \lesssim 10$ GPa.

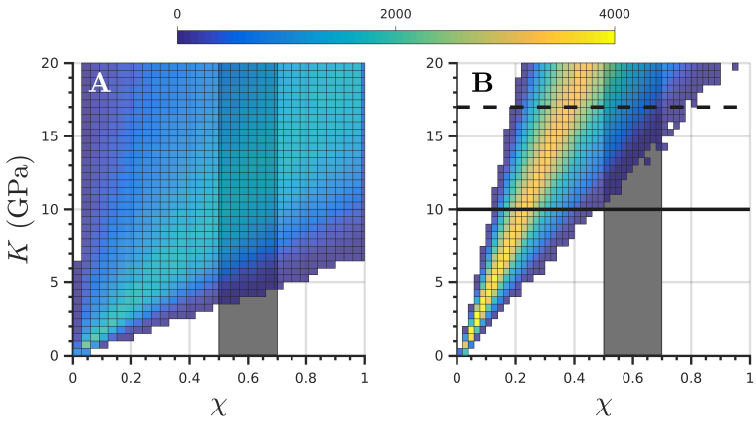

Figure 5: Bivariate histograms for K and χ for a pure liquid phase pore fluid in the Reykjanes reservoir (Keiding et al., 2010), for $0 \leq \phi \leq 0.35$ (A) and $\phi = 0.1$ (B). Frequency of sampled parameter combinations according to color scale. The parameter space was sampled using uniform prior distributions. The dashed black horizontal line depicts $K = 17\,\text{GPa}$, the black horizontal line depicts $K = 10\,\text{GPa}$ the vertical gray bar depicts $0.5 < \chi < 0.7$ (recharge between 30% and 50%, see Axelsson et al., 2015).

Due to production-induced pressure drop a steam cap developed in the reservoir (Axelsson et al., 2015). Since the deformation study of Keiding et al. (2010) covers only the beginning of the geothermal fluid production, it is not clear whether or not the amount of steam in the reservoir is significant at that time. We test both the effect of a purely liquid and a two-phase pore fluid. Given the low estimate of K, for both cases we assume that $\alpha > 0.5$, see Equation A.2. For simplicity, we assume the pore fluid's liquid phase is pure water, although in reality it is hydrothermally altered seawater (Axelsson et al., 2015).

3.2.1 Purely liquid pore fluid

First, we test the case of a purely liquid pore fluid, given material parameters as discussed above and a porosity of $0.01 \leq \phi \leq 0.35$. We find that $\Delta V_r / \Delta M_{f,t} = 4 \cdot 10^{-5}\,\text{m}^3\,\text{kg}^{-1}$ can be explained by a wide range of combinations of χ and K, as shown in Figure 5A. For geothermal reservoirs in Iceland a common assumption is $\phi = 0.1$, which we can apply to see if it helps to better constrain the parameters. Looking at the trade-off between K and χ after adding the constraints (Figure 5B), we can see that for $K = 17\,\text{GPa}$, the possible values of χ fall in the range 0.25–0.65 while for $K < 10\,\text{GPa}$ we get $\chi < 0.5$. For the period 2008–2010, Axelsson et al. (2015) estimate the recharge rate at Reykjanes to be about 30–50% (i.e. $0.5 < \chi < 0.7$), depicted by the vertical grey bar in Figure 5B. If the assumptions are correct (50–70% recharge rate and 10% porosity), this might imply these results are not compatible with our deformation-based estimate of the bulk modulus ($K < 10\,\text{GPa}$), meaning that a purely liquid pore fluid may not be plausible.

Table 2: Parameters of water, steam and rock at temperature on the vapour-liquid saturation curve at 10 MPa and 310 °C; for the Reykjanes field.

Parameter	Value
T	583 K
$c_{p,r}$	$1.0\,\mathrm{kJ\,kg^{-1}\,K^{-1}}$
$c_{p,w}$	$6.1\,\mathrm{kJ\,kg^{-1}\,K^{-1}}$
$c_{p,s}$	$7.1\,\mathrm{kJ\,kg^{-1}\,K^{-1}}$
ρ_r	$2500\,\mathrm{kg\,m^{-3}}$
ρ_w	$688\,\mathrm{kg\,m^{-3}}$
ρ_s	$55\,\mathrm{kg\,m^{-3}}$
L	$2.3 \cdot 10^6\,\mathrm{J\,kg^{-1}}$

3.2.2 Two-phase pore fluid

We test whether it is possible to achieve $\Delta V_r/\Delta M_{f,t}$ of $\sim 4 \cdot 10^{-5}\,\mathrm{m^3\,kg^{-1}}$ by two-phase reservoir conditions. We assume that average reservoir pressure is 10 MPa and that reservoir conditions are on the boiling point curve (temperature of 310 °C). The parameters for these conditions are shown in Table 2. The range of plausible combinations of liquid volume fraction f_l and reservoir bulk modulus K are any $0 < f_l < 1$ and $K < 10$ GPa, while the most probable are $0 < f_l < 0.8$ and $K < 5$ GPa (see Figure 6). Two-phase compressibility allows for a wider range of parameter values than the single-phase assumption. This suggests that a two-phase pore fluid may be more plausible in the Reykjanes case.

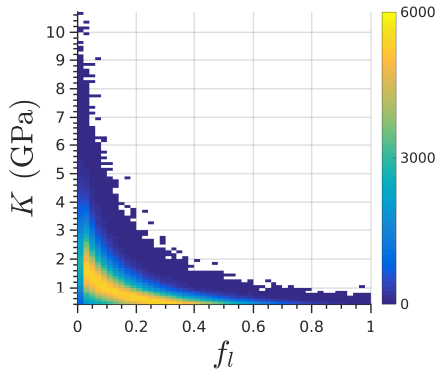

Figure 6: Bivariate histogram of liquid saturation f_l and reservoir bulk modulus K for a two phase pore fluid. Calculated using Equation 9 for deformation at the Reykjanes geothermal field (Keiding et al., 2010). Colour scale depicts the frequency of sampled parameter combinations. The parameter space was sampled using uniform prior distributions.

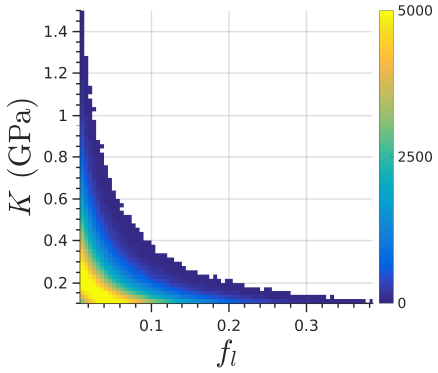

Figure 7: Bivariate histogram of liquid saturation f_l and reservoir bulk modulus K for a two phase pore fluid. Calculated using Equation 9 for deformation at The Geysers (Mossop and Segall, 1997, 1999). Colour scale depicts the frequency of sampled parameter combinations. The parameter space was sampled using uniform prior distributions.

3.3 The Geysers, California, USA

Large scale geothermal power production at The Geysers began in 1960, with production being strongly increased from 1972 to the late 1980's (Barker et al., 1992). Mossop and Segall (1997, 1999) published two studies presenting deformation obtained by GPS and leveling observations at The Geysers between 1977 and 1996. From their estimates of volumetric strain and observations of reservoir pressure changes, they estimate $K \leq 4.6\,\text{GPa}$ (Mossop and Segall, 1999). For the solid grain bulk modulus they assume $K_S' \approx 37\,\text{GPa}$. From the estimates for K and K_S' we can derive an estimate range for values of α using Equation A.2, giving $0.9 < \alpha < 1$, which we will apply here. Gunderson (1992) and Barker et al. (1992) report reservoir matrix- and fracture porosities of 1–6% and 1–2%, respectively. According to this, we assume the gross reservoir porosity to be $0.01 \leq \phi \leq 0.1$. We assume that the average reservoir pressure is approximately 2 MPa (see Barker et al., 1992). For Poisson's ratio of the reservoir we use a range of $0.1 \leq \nu \leq 0.4$.

The total extracted mass for the investigated time interval is $1.4 \cdot 10^{12}\,\text{kg}$ and the reservoir volume change is $\Delta V_r \approx 9 \cdot 10^7\,\text{m}^3$ (Mossop and Segall, 1997), giving a ratio for volume change per extracted mass of $\Delta V_r/\Delta M_{f,t}$ of $6 \cdot 10^{-5}\,\text{m}^3\,\text{kg}^{-1}$.

First we test the case of two-phase compressibility. As for the previous examples we can use Equation 10 to calculate K_f, which for a temperature of 212 °C and a pressure of 2 MPa (saturation conditions) yields values of $K_f < 0.1\,\text{MPa}$. Such low values of K_f produce low values of $\Delta V_r/\Delta M_{f,t}$, considerably lower than $6 \cdot 10^{-5}\,\text{m}^3\,\text{kg}^{-1}$. For $K > 1\,\text{GPa}$, $\Delta V_r/\Delta M_{f,t}$ is never higher than $2 \cdot 10^{-5}\,\text{m}^3\,\text{kg}^{-1}$. For $K < 1\,\text{GPa}$ and small values for liquid volume fraction f_l, on the other hand, it is possible to obtain $\Delta V_r/\Delta M_{f,t} \approx 6 \cdot 10^{-5}\,\text{m}^3\,\text{kg}^{-1}$ (Figure 7).

Next, we investigate single-phase conditions. For the pure water case we assume a temperature of 210 °C and pressure of 2 MPa. According to these conditions we

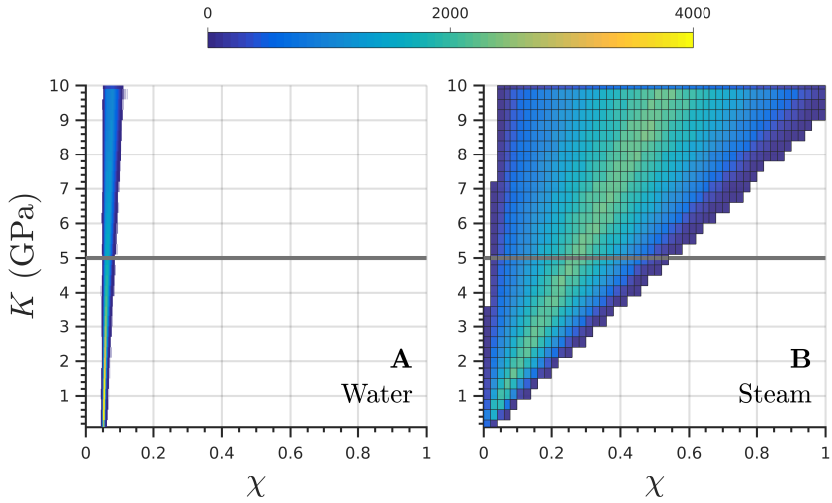

Figure 8: Bivariate histograms for K and χ for single-phase pore fluid at the Geysers reservoir (Mossop and Segall, 1997, 1999), both for pure liquid (A) and pure vapour phase pore fluid (B). The grey lines show $K = 3.6\,\text{GPa}$ the estimated maximum by (Mossop and Segall, 1997). Color scale depicts the frequency of sampled parameter combinations. The parameter space was sampled using uniform prior distributions.

assume a density of water of $850\,\text{kg}\,\text{m}^{-3}$ and a fluid bulk modulus of $K_f = 1000\,\text{MPa}$. We can apply Equation 9 to determine the most likely combinations of χ and K (see Figure 8A). The results imply that under the assumption that we observe deformation from the whole reservoir, the the case of pure water as pore fluid requires a minimum recharge $(1-\chi)$ of 90%. For the pure vapour case we assume a temperature of 240 °C and a pressure of 2 MPa. For these conditions we use a bulk modulus of vapour of $K_f = 2\,\text{MPa}$ and a density of $10\,\text{kg}\,\text{m}^{-3}$. The results allow a wider range of χ than the pure water case, with a minimum recharge of 50% for $K < 5\,\text{GPa}$ (see Figure 8B).

It seems to be generally assumed that for the studied time interval, The Geysers are a two-phase reservoir (Barker et al., 1992; Mossop and Segall, 1999). Our results indicate that this may explain the magnitude of deformation per mass of fluid extracted, albeit it implies a very small bulk modulus of $K < 1.5\,\text{GPa}$. Alternatively, pure steam conditions can also plausibly explain the observed deformation, allowing a wider range

of K.

4 Discussion

In a fluid reservoir, the relation between the volume or mass of extracted fluid to the volume change of the reservoir due to contraction depends on elastic and poroelastic parameters of fluid and solid (K, K_f, ν, α, ϕ) as well as the amount of recharge. The equations derived in this study show that the reservoir volume change and the fluid volume change can not be expected to have the same value, except for the idealized case of both pore fluid and solid matrix being incompressible. Expected values should be $\Delta V_r/\Delta V_{f,t} < 1$, or $\Delta V_r/\Delta M_{f,t} < 10^{-3}\,\mathrm{m^3\,kg^{-1}}$ in case of fluid mass, where the magnitude primarily depends on the ratio of the reservoir bulk modulus over fluid bulk modulus and the amount of recharge into the reservoir.

It should be noted that the assumptions made to simplify the reservoir model, for example that the vertical extent of the reservoir is relatively small, might not be true for a real reservoir. If a reservoir has a large vertical extent, material heterogeneities become more important and we may have to consider that deeper parts of a reservoir generally have a lower porosity (less fluid volume) and a higher rock bulk modulus (due to the dependence of K on confining pressures, see Section 2.1.2). This means that the deeper parts cause significantly less surface deformation than the shallower parts. Therefore, some of the reservoir deformation may not be detected by geodetic observations which would lead to an underestimate of the reservoir volume change ΔV_r. In future studies, an improved representation of physical complexities in the reservoir models could help to increase the accuracy of the method presented here.

4.1 Difference in $\Delta V_r/\Delta M_{f,t}$ between different geothermal reservoirs

Three examples of geothermal systems in Iceland and the USA, all of which exhibit fluid pressure decrease, show different magnitudes of deformation despite all of them being fractured rock two-phase systems. The Hellisheidi system exhibits considerably lower values of deformation per extraction ($\Delta V_r/\Delta M_{f,t}$ in the order of $10^{-6}\,\mathrm{m^3\,kg^{-1}}$) than the Reykjanes system and The Geysers ($\Delta V_r/\Delta M_{f,t}$ in the order of $10^{-5}\,\mathrm{m^3\,kg^{-1}}$). Investigating the different examples indicate that the difference of this value is strongly affected by the compressibility of the pore fluid, the value of which being controlled by whether the fluid is in a single-phase or of two-phase state. The two-phase compressibility of a water-steam system can be very high, higher than either of the single phase counterparts. This means that in a two-phase system the pressure change, as well as the deformation, will be significantly smaller even if extraction rate, reservoir volume and reservoir properties are the same. Even though the results of each example are not entirely conclusive, they carry useful implications. At Hellisheidi we find that the relatively low $\Delta V_r/\Delta M_{f,t}$ can very well be explained by two-phase conditions in the reservoir. In the case of Reykjanes, two-phase conditions seem to be more plausible than pure water and require a low bulk modulus, most likely lower than 5 GPa. At The Geysers, both pure steam and two-phase conditions are possible candidates to

explain the deformation. Research about reservoir conditions (e.g. Barker et al., 1992) indicate that, during the study interval 1977–1996, the reservoir was under two-phase conditions. If this is correct, this would imply a very low bulk modulus of less than 1.5 GPa.

While we expect the reservoirs in the presented examples to exhibit two-phase fluid compressibilities in all cases, given the knowledge we have about these reservoirs, we can not rule out that single-phase conditions can occur. High temperature geothermal reservoirs often evolve through different states during their lifetime, from liquid dominated to two-phase to vapour-dominated. Therefore, the ratio of deformation volume per mass of extracted fluid may change over a reservoir's lifetime. The Reykjanes power plant had just been commissioned at the time when Keiding et al. (2010) studied the deformation (2005–2008), which means that it is possible that the reservoir at this point was still liquid dominated. If this was the case, we would expect that the ratio of deformation volume to extracted fluid mass decreases with ongoing production. If the ratio does not change if is more likely that the deformation behaviour was dominated by a two-phase pore fluid from the beginning, as both the single phase and the two-phase explanation are possible (see Section 3.2). Investigating how the deformation per extracted fluid varies over longer time intervals would be an interesting study that might give further insight into this problem. At The Geysers, the production had been going on for several years before the deformation studies of Mossop and Segall (1997, 1999), investigating the time interval of 1977–1996. This could mean that the pore and fracture space was mostly filled with steam by the time the deformation was observed. Even though for both Reykjanes and The Geysers it can not be conclusively stated whether two-phase or single-phase conditions, either possibility has different implications for material parameter values. Two-phase conditions, due to the low fluid bulk modulus, require a low reservoir bulk modulus. Single-phase conditions, on the other hand, may imply a lower limit for the reservoir recharge (or, an upper limit for χ).

4.2 Constraining material parameters

The work presented here highlights the importance of constraining material parameters. The values of the reservoir bulk modulus K in the given examples, estimated from deformation data, fall in all cases below commonly obtained values for different rocks derived from seismic data or laboratory experiments. Possible explanations for this are discussed by e.g. Heuze (1980) and Mossop and Segall (1997, 1999). Seismic wavelengths are insensitive to small pore and fracture length scales. Laboratory experiments on the other hand fail to capture effects of scales larger than the lab sample. Apart from the difficulties in estimating K through different methods, the values of K can vary greatly between reservoirs at different locations because they depend on a number of factors: on rock type, degree of fracturing and confining pressures (e.g. Zimmerman et al., 1986). This means they can vary strongly depending on depth and location and should not be simply adopted from one location to another even if geological conditions are similar. Deformation studies in a partly controlled setting like we have in cases of geothermal reservoir deformation, offer, in cases where the mass of extracted fluid and changes in reservoir pressures are known, opportunities to deter-

mine the effective quasi-static bulk modulus which we should make use of. Additional constraints on K can lead to constraints of other material parameters, which allows for a more accurate interpretation of results of surface deformation studies. In combination with fluid extraction rates this can lead to a better understanding of reservoir deformation.

We show that it may be possible to use the presented methods to determine whether the pore fluid is water, steam or two-phase. The knowledge about which fluid state prevails in a reservoir is important for the successful implementation of forward models of reservoir deformation. Our results imply that if the wrong fluid compressibility is used in a deformation model driven by fluid extraction, predicted deformation can be under- or overestimated by one order of magnitude. Instead, in order to improve accuracy of forward model predictions, we should make use of volume change estimates from geodetic observations in combination with a) pressure changes to constrain the reservoir bulk modulus K and b) extraction rates to constrain the fluid bulk modulus K_f.

4.3 Deformation caused by reservoir temperature changes

While this study focusses on deformation caused by reservoir pressure changes, there are also examples of deforming geothermal reservoirs where temperature decrease has been identified as the driving cause of deformation, see e.g. Drouin et al. (2017) who studied deformation in the Krafla geothermal area in North Iceland. Interestingly, Drouin et al. (2017) find a value of $\Delta V_r/\Delta M_{f,t}$ very similar to the Hellisheidi example, which in their case is $\sim 8 \cdot 10^{-6}\,\mathrm{m^3\,kg^{-1}}$. For the thermoelastic case, the deformation behaviour could be studied analogously to the poroelastic analysis presented in this study.

5 Conclusions

We derive an equation that relates rock volume changes estimated from deformation studies to the mass of extracted fluid from a flat reservoir. The equation shows that the change in reservoir volume, given the mass of extracted fluid, depends on fluid compressibility and elastic rock properties, as well as the rate of fluid recharge. We use examples from three different geothermal fields, where the ratio of deformation volume per mass of extracted fluid varies by one order of magnitude, to investigate how the obtained relation between deformation, extraction and material properties can be applied. Using a stochastic approach we identify how varying parameter combinations affect the difference in the volume change per fluid mass extraction ratio, and found that the compressibilities of pore fluid and reservoir rock have a significant effect. Our results indicate that low reservoir bulk moduli, $K \lesssim 5\,\mathrm{GPa}$, agree well with reported deformation at the geothermal fields Hellsheidi, Reykjanes and The Geysers. This study shows that using the methods presented here for interpreting observations of surface deformation can help to better constrain reservoir conditions and improve our understanding of geothermal reservoirs.

Acknowledgments

We would like to thank Andrew Hooper (University of Leeds, GB), Björn Lund (Uppsala University, SE), Sigurjón Jónsson (King Abdullah University of Science and Technology, SA), Ólafur Flóvenz (Iceland GeoSurvey) and Freysteinn Sigmundsson (University of Iceland) for helpful comments on the manuscript. This work was supported in part by grants from the Iceland Research Fund (grant numbers 130371-051/052/053 and 174377-051) and the University of Iceland Research Fund (grant number HI-6489).

Appendix A Relations between poroelastic parameters and constants

Relations between poroelastic parameters and constants that are used in this study, taken or slightly recast from Wang (2000).

Bulk modulus K in terms of shear modulus G and Poisson's ratio ν

$$K = \frac{2G(1+\nu)}{3(1-2\nu)} \tag{A.1}$$

Bulk modulus of the solid skeleton K'_S

$$K'_S = \frac{K}{1-\alpha} \iff \alpha = 1 - \frac{K}{K'_S} \tag{A.2}$$

Uniaxial bulk modulus K_ν

$$K_\nu = 3K\frac{1-\nu}{1+\nu} \tag{A.3}$$

Drained pore bulk modulus K_p

$$K_p = \frac{\phi K}{\alpha} \tag{A.4}$$

References

Ali, S. T., Akerley, J., Baluyut, E. C., Cardiff, M., Davatzes, N. C., Feigl, K. L., Foxall, W., Fratta, D., Mellors, R. J., Spielman, P., Wang, H. F., and Zemach, E. (2016). Time-series analysis of surface deformation at Brady Hot Springs geothermal field (Nevada) using interferometric synthetic aperture radar. *Geothermics*, 61:114–120.

Allis, R. G. (2000). Review of subsidence at Wairakei field, New Zealand. *Geothermics*, 29:455–478.

Amoruso, A. and Crescentini, L. (2009). Shape and volume change of pressurized ellipsoidal cavities from deformation and seismic data. *J. Geophys. Res.*, 114.

Axelsson, G., Arnaldsson, A., Berthet, J.-C. C., Bromley, C. J., Gudnason, E. Á., Hreinsdóttir, S., Karlsdóttir, R., Magnússon, I. T., Michalczewska, K. L., Sigmundsson, F., et al. (2015). Renewability Assessment of the Reykjanes Geothermal System, SW-Iceland. In *Proc. of the World Geothermal Congress 2015*.

Barbour, A. J., Evans, E. L., Hickman, S. H., and Eneva, M. (2016). Subsidence rates at the southern Salton Sea consistent with reservoir depletion. *Journal of Geophysical Research: Solid Earth*, 121(7):5308–5327.

Barker, B. J., Gulati, M. S., Bryan, M. A., and Riedel, K. L. (1992). Geysers Reservoir Performance. In *Monograph on The Geysers Geothermal Field, Special Report No. 17*, pages 167–177. Geothermal Resources Council.

Berge, P. and Berryman, J. (1995). Realizability of negative pore compressibility in poroelastic composites. *Journal of Applied Mechanics*, 62:1053–1062.

Biot, M. A. (1941). General theory of three-dimensional consolidation. *Journal of Applied Physics*, 12(2):155–164.

Bromley, C., Brockbank, K., Glynn-Morris, T., Rosenberg, M., Pender, M., O'Sullivan, M., and Currie, S. (2013). Geothermal subsidence study at Wairakei–Tauhara, New Zealand. *Proceedings of the Institution of Civil Engineers - Geotechnical Engineering*, 166(2):211–223.

Drouin, V., Sigmundsson, F., Verhagen, S., Ófeigsson, B. G., Spaans, K., and Hreinsdóttir, S. (2017). Deformation at Krafla and Bjarnarflag geothermal areas, Northern Volcanic Zone of Iceland, 1993–2015. *Journal of Volcanology and Geothermal Research*, 344:92–105.

Ehrenberg, S. N. and Nadeau, P. H. (2005). Sandstone vs. carbonate petroleum reservoirs: A global perspective on porosity-depth and porosity-permeability relationships. *AAPG bulletin*, 89(4):435–445.

Eissa, E. A. and Kazi, A. (1988). Relation between static and dynamic Young's moduli of rocks. *International Journal of Rock Mechanics and Mining Sciences & Geomechanics Abstracts*, 25(6):479–482.

Eshelby, J. D. (1957). The determination of the elastic field of an ellipsoidal inclusion, and related problems. In *Proc. R. Soc. Lond. A*, volume 241, pages 376–396. The Royal Society.

Eysteinsson, H. (2000). Elevation and gravity changes at geothermal fields on the Reykjanes Peninsula, SW Iceland. In *Proceedings World Geothermal Congress*, pages 559–564.

Fialko, Y. and Simons, M. (2000). Deformation and seismicity in the Coso geothermal area, Inyo County, California: Observations and modeling using satellite radar interferometry. *J. Geophys. Res.*, 105:21,781–21,793.

Foxall, W. and Vasco, D. (2003). Inversion of synthetic aperture radar interferograms for sources of production-related subsidence at the Dixie Valley geothermal field. Technical report, Lawrence Livermore National Laboratory (LLNL), Livermore, CA.

Geertsma, J. (1957). The effect of fluid pressure decline on volumetric changes of porous rocks. *Petroleum Transactions, AIME*, 210:331–340.

Geertsma, J. (1966). Problems of rock mechanics in petroleum production engineering. In *Proceedings of the 1st ISRM Congress*. International Society for Rock Mechanics.

Geertsma, J. (1973). Land subsidence above compacting oil and gas reservoirs. *Journal of Petroleum Technology*, 25(06):734–744.

Gercek, H. (2007). Poisson's ratio values for rocks. *International Journal of Rock Mechanics and Mining Sciences*, 44(1):1–13.

Grant, M. A. (2011). *Geothermal Reservoir Engineering*. Wiley Online Library, second edition.

Grant, M. A. and Sorey, M. L. (1979). The compressibility and hydraulic diffusivity of a water-steam flow. *Water Resources Research*, 15(3):684–686.

Guðnason, E. Á., Arnaldsson, A., Axelsson, G., Berthet, J.-C. C., Halldórsdóttir, S., and Magnússon, I. Þ. (2015). Analysis and Modelling of Gravity Changes in the Reykjanes Geothermal System in Iceland, During 2004–2010. In *Proceedings World Geothermal Congress 2015*.

Gunderson, R. P. (1992). Porosity of reservoir graywacke at The Geysers. In *Monograph on The Geysers Geothermal Field, Special Report No. 17*, pages 89–93. Geothermal Resources Council.

Gunnarsson, G., Arnaldsson, A., and Oddsdóttir, A. L. (2011). Model simulations of the Hengill Area, southwestern Iceland. *Transp Porous Med*, 90:3–22.

Gunnlaugsson, E. (2016). Hellisheiði – vinnsluskýrsla 2015. Technical report, Orkuveita Reykjavíkur (Reykjavik Energy), Reykjavik, Iceland. [In Icelandic].

Haraldsdóttir, S. H. (2014). Mælingareftirlit á vinnslusvæðum Hellisheiðarvirkjunar árið 2014. Technical Report 2014/052, ÍSOR, Reykjavik, Iceland. [In Icelandic].

Hatton, J. (1970). Ground subsidence of a geothermal field during exploitation. *Geothermics*, 2:1294–1296.

Heuze, F. E. (1980). Scale effects in the determination of rock mass strength and deformability. *Rock Mechanics*, 12(3-4):167–192.

Juncu, D., Árnadóttir, T., Hooper, A., and Gunnarsson, G. (2017a). Anthropogenic and natural ground deformation in the Hengill geothermal area, Iceland. *Journal of Geophysical Research: Solid Earth*, 122(1):692–709.

Juncu, D., Árnadóttir, T., Geirsson, H., Guðmundsson, Lund, B., Gunnarsson, G., Hooper, A., Hreinsdóttir, S., and Michalczewska, K. (2017b). Injection-induced surface deformation and seismicity at the Hellisheidi geothermal field, Iceland. Manuscript submitted for publication.

Keiding, M., Árnadóttir, T., Jónsson, S., Decriem, J., and Hooper, A. (2010). Plate boundary deformation and man-made subsidence around geothermal fields on the Reykjanes Peninsula, Iceland. *J. Volc. Geotherm. Res.*, 194:139–149.

Manger, G. E. (1963). Porosity and bulk density of sedimentary rocks. *Geological Survey Bulletin 1144-E*.

Mavko, G., Mukerji, T., and Dvorkin, J. (2009). *Rock physics handbook*. Cambridge University Press.

Minson, S. E., Simons, M., and Beck, J. L. (2013). Bayesian inversion for finite fault earthquake source models I–theory and algorithm. *Geophys. J. Int.*, 194:1701–1726.

Moench, A. F. and Atkinson, P. G. (1978). Transient-pressure analysis in geothermal steam reservoirs with an immobile vaporizing liquid phase. *Geothermics*, 7(2-4):253–264.

Mossop, A. and Segall, P. (1997). Subsidence at The Geysers geothermal field, N. California from a comparison of GPS and leveling surveys. *Geophysical Research Letters*, 24(14):1839–1842.

Mossop, A. and Segall, P. (1999). Volume strain within the Geysers geothermal field. *Journal of Geophysical Research: Solid Earth*, 104(B12):29113–29131.

Sarychikhina, O., Glowacka, E., Mellors, R., and Vidal, F. S. (2011). Land subsidence in the Cerro Prieto Geothermal Field, Baja California, Mexico, from 1994 to 2005: An integrated analysis of DInSAR, leveling and geological data. *Journal of Volcanology and Geothermal Research*, 204(1):76–90.

Segall, P. (1992). Induced stresses due to fluid extraction from axisymmetric reservoirs. *Pure and Applied Geophysics*, 139(3):535–560.

van Heerden, W. L. (1987). General relations between static and dynamic moduli of rocks. *International Journal of Rock Mechanics and Mining Sciences & Geomechanics Abstracts*, 24(6):381–385.

Vasco, D. W., Wicks Jr, C., Karasaki, K., and Marques, O. (2002). Geodetic imaging: reservoir monitoring using satellite interferometry. *Geophysical Journal International*, 149(3):555–571.

Wagner, W. and Kretzschmar, H.-J. (2007). *International Steam Tables: Properties of Water and Steam based on the Industrial Formulation IAPWS-IF97*. Springer Science & Business Media.

Wang, H. F. (2000). *Theory of Linear Poroelasticity with Applications to Geomechanics and Hydrogeology*. Princeton University Press Princeton, NJ.

Zienkiewicz, O. and Shiomi, T. (1984). Dynamic behaviour of saturated porous media; the generalized Biot formulation and its numerical solution. *International Journal for Numerical and Analytical Methods in Geomechanics*, 8(1):71–96.

Zimmerman, R. W., Somerton, W. H., and King, M. S. (1986). Compressibility of porous rocks. *Journal of Geophysical Research: Solid Earth*, 91(B12):12765–12777.

Supplement material: Bivariate histograms of material parameters inferred from the inversion of geodetic data

By inversion of geodetic data from the Hellisheidi geothermal field (Juncu et al., 2017) using a Bayesian Markov chain Monte Carlo algorithm (Catmip, Minson et al., 2013), we obtained posterior probability distributions of the model parameters as depicted in Figures S1 and S2.

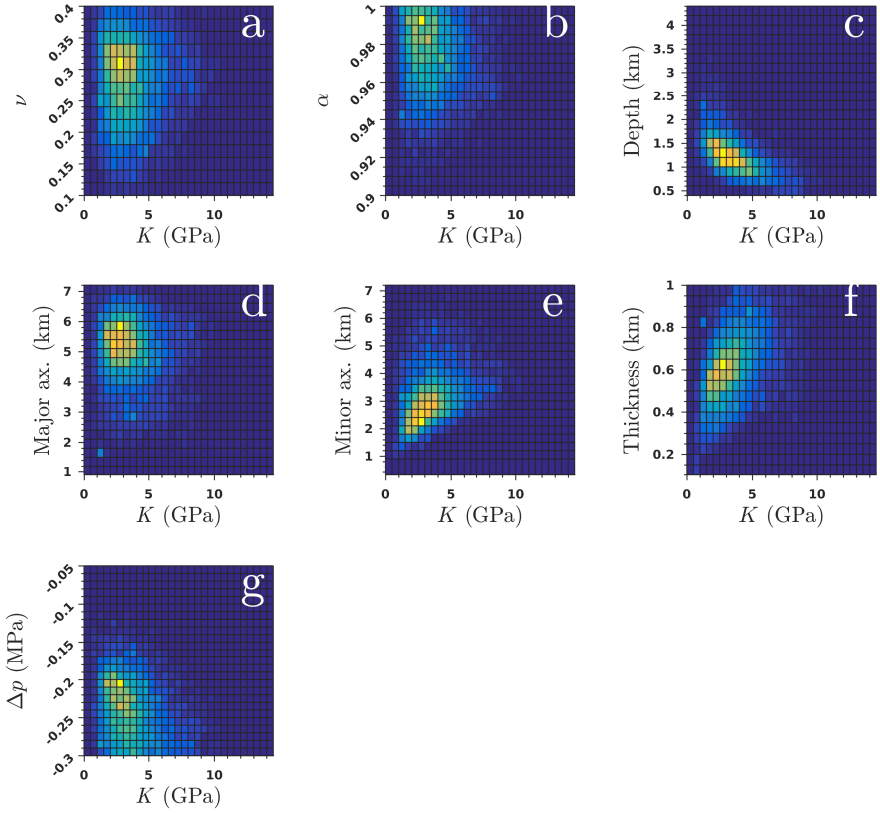

Figure S1: Bivariate histograms of the source parameters in the model optimization using geodetic data. Bulk modulus K with Poisson's ratio ν (a), Biot's coefficient α (b), depth (c), major axis (d), minor axis (e), thickness (f) and pressure decrease (g) of the reservoir. The color scale gives the frequency of results within a bin, from higher frequencies depicted by yellow to lower frequencies depicted by blue.

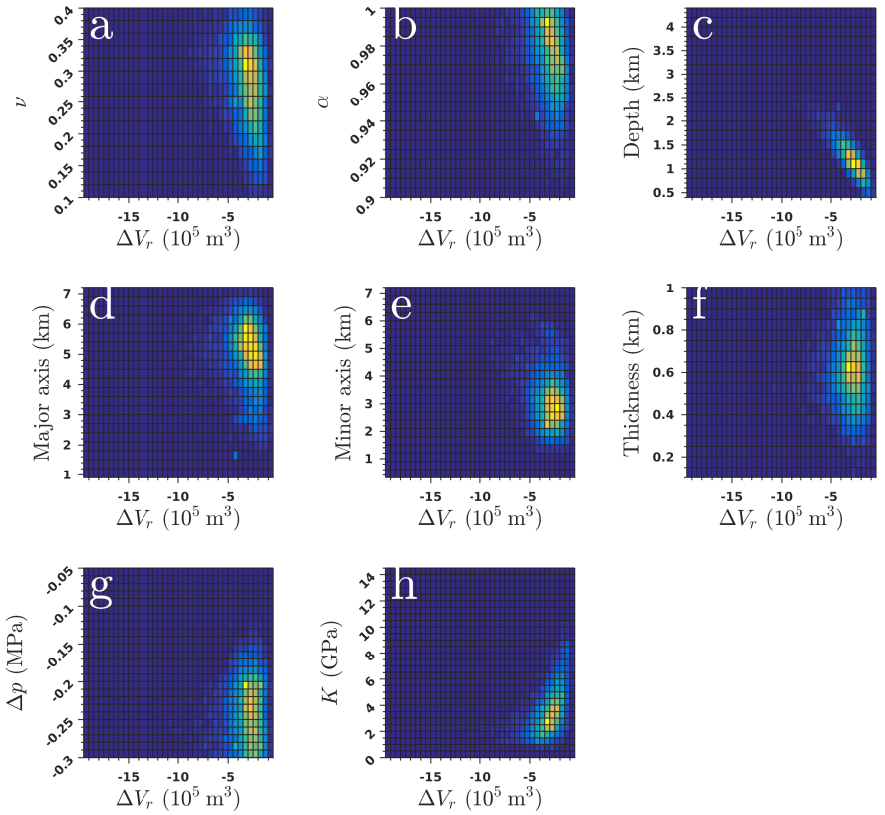

Figure S2: Bivariate histograms of the source parameters in the model optimization using geodetic data. Reservoir volume change ΔV_r with Poisson's ratio ν (a), Biot's coefficient α (b), depth (c), major axis (d), minor axis (e), thickness (f), pressure decrease (g) of the and bulk modulus K of the reservoir. The color scale gives the frequency of results within a bin, from higher frequencies depicted by yellow to lower frequencies depicted by blue.

References

Juncu, D., Árnadóttir, T., Hooper, A., and Gunnarsson, G. (2017). Anthropogenic and natural ground deformation in the Hengill geothermal area, Iceland. *Journal of Geophysical Research: Solid Earth*, 122(1):692–709.

Minson, S. E., Simons, M., and Beck, J. L. (2013). Bayesian inversion for finite fault earthquake source models I–theory and algorithm. *Geophys. J. Int.*, 194:1701–1726.